Affinity-tuning leukocyte integrin for development of safe therapeutics

A Dissertation

Presented to the Faculty of the Graduate School

Of Cornell University

In Partial Fulfillment of the Requirements for the Degree of

Doctor of Philosophy

by

Spencer Park

January 2017

Affinity-tuning leukocyte integrin for development of safe therapeutics

Spencer Park, Ph. D.

Cornell University 2017

Much attention has been given to the molecular and cellular pathways linking inflammation with cancer and the local tumor environment to identify new target molecules that could lead to improved diagnosis and treatment. Among the many molecular players involved in the complex response, central to the induction of inflammation is intercellular adhesion molecule (ICAM)-1, which is of particular interest for its highly sensitive and localized expression in response to inflammatory signals. ICAM-1, which has been implicated to play a critical role in tumor progression in various types of cancer, has also been linked to cancer metastases, where ICAM-1 facilitates the spread of metastatic cancer cells to secondary sites. This unique expression profile of ICAM-1 throughout solid tumor microenvironment makes ICAM-1 an intriguing molecular target, which holds great potential as an important diagnostic and therapeutic tool.

Herein, we have engineered the ligand binding domain, or the inserted (I) domain of a leukocyte integrin, to exhibit a wide range of monovalent affinities to the natural ligand, ICAM-1. Using the resulting I domain variants, we have created drug and gene delivery nanoparticles, as well as targeted immunotherapeutics that have the ability to bind and migrate to inflammatory sites prevalent in tumors and the associated microenvironment. Through the delivery of diagnostic agents, chemotherapeutics, and immunotherapeutics, the following

chapters demonstrate that the affinity enhancements achieved by directed evolution bring the affinity of I domains into the range optimal for numerous applications.

BIOGRAPHICAL SKETCH

Spencer Park was born on January 9th, 1986 in Chapel Hill, North Carolina as the only son to Jeehyun Kim and Chun-wook Park. At the time, Jeehyun Kim and Chun-wook Park were Ph.D. candidate students at University of North Carolina studying Nutritional Science and Civil Engineering, respectively. Soon after Spencer's birth, his father was diagnosed with lung cancer, which prompted the family to relocated to Seoul, Korea, before completing the graduate studies. Despite the valiant efforts and support from family and friends, Chun-wook passed away on March 23rd of 1990, which left Spencer to be raised by Jeehyun as a single-mother.

Because Spencer's mother was a young single mother that had to work to raise a child, Spencer spent most of his childhood days with his grandparents, who not only fed and took care of him, but also helped him with his homework and tended to his school needs. At first, Spencer attended Yang-jun elementary school in Gae-po-dong, Seoul and thrived in classes as well as in extracurricular activities. However, despite his grandparents' efforts, when Spencer entered 6th grade, his school performance began to slip and he was beginning to be associated with the troublesome groups of the school.

Concerned by these sudden series of events, Spencer's mother, who had been working hard to build her own career, decided she would have to forego her ambitions to raise Spencer in a new environment. With this decision came the move back to the United States, which became the turning point for Spencer. Despite the language barrier that hindered his performance in many of the humanities classes, he excelled in math and science courses. Being away from the academically competitive environment that is prevalent in Korea, Spencer could

immerse himself in various extracurricular activities, such as skiing, soccer, basketball, and violin. By the time Spencer was a Senior in high school, he had collected many awards and trophies from attending state-wide and nation-wide events.

Spencer pursued his undergraduate studies at Cornell University from 2004 to 2008, majoring in Biological and Environmental Engineering with a minor in Biomedical Engineering. Though at first he was drawn to designing and functionalizing devices that can be used in diagnostics or therapy, gradually his interests began to change. During the summers, he worked in Dr. Joseph Wu's lab at New York Medical College studying some of the biochemical signaling pathways important in tumor progression. For the work done at Dr. Wu's lab, Spencer was awarded a fellowship prize. Then, the trigger for a change came when Spencer took Molecular Principles of Biomedical Engineering taught by Dr. Moonsoo Jin. The introduction to the molecular components of diseases and application of various therapy methods seemed enticing and to learn more Spencer joined Dr. Jin's lab.

For the following 7 years, Spencer worked with Dr. Jin at first as a lab manager then as a graduate student on projects ranging from designing drug delivery systems to targeted immunotherapy via engineering T cells with chimeric antigen receptors. He was awarded a graduate research fellowship prize from National Science Foundation CLIMB, presented in multiple conferences, and published two first author papers. Additionally, he has another first author paper in preparation. Starting in September 2016, he will be working for Pfizer in South San Francisco.

ACKNOWLEDGMENTS

I realize now after having gone through the entirety of my graduate studies that obtaining a doctoral degree is not through one person's efforts. Without the help of numerous people giving me patient and relentless help, I would not have been able to be where I am today.

It is difficult to list all the things I am grateful for, but nonetheless I would like to express my gratitude and appreciation to my advisor, Dr. Moonsoo Jin. He has set an example of excellence as a researcher, mentor, instructor, and role model. I came to Dr. Jin as an undergraduate student inspired after one of his lectures in Molecular Principles of Biomedical Engineering asking to join his lab. That was 7 years ago and since then he couldn't get rid of me. His methodical yet zealous approach to solving many clinical problems has motivated me to pursue Ph.D. under his guidance. Looking through my old lab notebooks, it is evident how much I have grown as a scientist, especially in my ability to think critically, persevere through obstacles, and apply knowledge from many different engineering and basic sciences disciplines in answering questions. Even after 7 years, I am often awed by how he effortlessly provides suggestions to problems that seem daunting at first. Undoubtedly, everything I am today as a scientist I owe to Dr. Jin and I am forever grateful to him for preparing me to be who I am today.

I would also like to thank my committee members, Dr. Michael King and Dr. Rasa Zarnegar for the words of encouragement, guidance in my graduate work, and support in job searches. Your guidance through this process, your discussion, ideas, and feedback have been

absolutely invaluable. This accomplishment would also have been impossible without the help of Belinda, Cliona, and Sindy, who have been tremendous through their administrative support.

Present and past members of Jin Lab have been fantastic. It was the late night, early morning discussions and challenges that have allowed me to grow as a scientist, but more so as a person. Working with Enda, Yogi, Marjan, and Susan as a team, we have done some great work. Coming from different backgrounds, we were able to bounce ideas off of each other to further our thinking. For the work presented in this dissertation, in particular, I thank Enda for teaching me the many aspects of *in vitro* T cell and lentiviral work as well as great pointers on my defense presentation. I thank Yogi for the countless plasmids and histology sections that have aided me in completing my project. Dr. Irene Min has been enormous help with her guidance in *ex vivo* analyses of mouse organs as well as her support during my job search process. Marjan has truly been an indispensable addition to our lab, spearheading and optimizing many of the animal experiments that was at first very new to all of us. Finally, without Susan's help and selflessness I would still be many months behind completion of my thesis, to say the least. She has sacrificed many hours on weekends and nights, in addition to normal work hours, to assist me in all dimensions of the CAR T cell project. It also helped that she was very good with T cell cultures and ELISA. She was not only a great lab assistant for my project but also a source of moral support. I would have gone hungry many nights if it were not for the dinners and coffees she brought for me. I have no doubt she will do great in dental school and anything that comes after. I believe the remaining members will also continue to learn and grow with Dr. Jin's guidance and I expect to hear about their amazing accomplishments down the road.

Past Jin lab members have also been indispensable but to point one person out, I would like to thank Sung-kwon Kang, or as we called him, Goose. He was and has been the source of motivation through many years. We stayed in lab late many nights having intellectually stimulating and fruitful discussions about our projects, and sometimes about other topics like investment opportunities. Though he is already doing well, I wish him all the best in his future endeavors. I also have great memories working alongside Tricia, Milly, Kristen, Leslie, Brian, Dave, Taehyun, Xuebo, Nina, Turner, Fai, Zoe, and Richard. Thanks to them, working in Jin Lab was not only stimulating but also fun.

Dedicated to Mom and Dad for
the immeasurable love and sacrifice,
to Bob and the rest of my family for
the patient support and prayers

TABLE OF CONTENTS

LIST OF FIGURES

LIST OF TABLES

CHAPTER 1

INTRODUCTION

Inflammation

Inflammation is the body's necessary response to harmful insult, in which a careful interplay between the immune system and damaged tissues mediate the healing process. The restoration is characterized by heat, pain, redness, and swelling, instigated by increased blood flow, accumulation of fluid, and release of chemicals such as histamine and bradykinin[1, 2]. This intricate process requires tight control over the various components of the immune system for achieving desired immune responses to eliminate the stimulus and heal in a timely manner[3]. Acute inflammation is a self-limiting transient response that usually results in controlled wound healing. Chronic inflammation, on the other hand, is a prolonged response prompted by dysregulated immunomodulation[4]. Such persistent homeostatic imbalance is often associated with many chronic human conditions and diseases, including allergy, atherosclerosis, and neoplastic progression[5-9].

In response to tissue damage, a complex network of biochemical and molecular cues initiate a cellular response designed to heal the afflicted tissue, where activated leukocytes are directed from the venous system to sites of damage. Monocytes and neutrophils, in addition to tissue-resident macrophages, are the first recruited effectors to the site of tissue injury, guided by chemotactic factors[10]. Once activated, macrophages become the main providers of growth

factors and cytokines, which activate endothelial, epithelial and mesenchymal cells in the inflamed milieu[10-12].

Activated vascular endothelium neighboring the site of tissue injury upregulate their expression of adhesion molecules in order to further orchestrate recognition by the circulating inflammatory cells[3, 10]. Simultaneously, leukocyte integrins, serving as binding partners for various adhesion molecules, are also induced and activated on the surface of approaching immune cells to allow tight adhesion to target sites (Fig. 1.1). Coupled with integrin clustering on the plasma membrane of leukocytes for increased valency, integrin affinity modulation has been shown to play a critical role in chemokine-induced arrest under flow[13, 14]. Finally, leukocytes transmigrate through the endothelium, either through the paracellular or transcellular route, facilitated by various extracellular proteases, such as matrix metalloproteinases[15, 16].

Inflammation and cancer

The link between inflammation and cancer was first postulated by Virchow in the 19th century, when he discovered the presence of leukocytes in tumors. Since then, many studies have strengthened this hypothesis and recently, clear evidence showing the roles that inflammation plays in tumor progression has been demonstrated[17, 18]. Now it is generally accepted that an inflamed milieu is a critical component of tumor initiation and progression[18], dubbing cancer as “wounds that do not heal”.

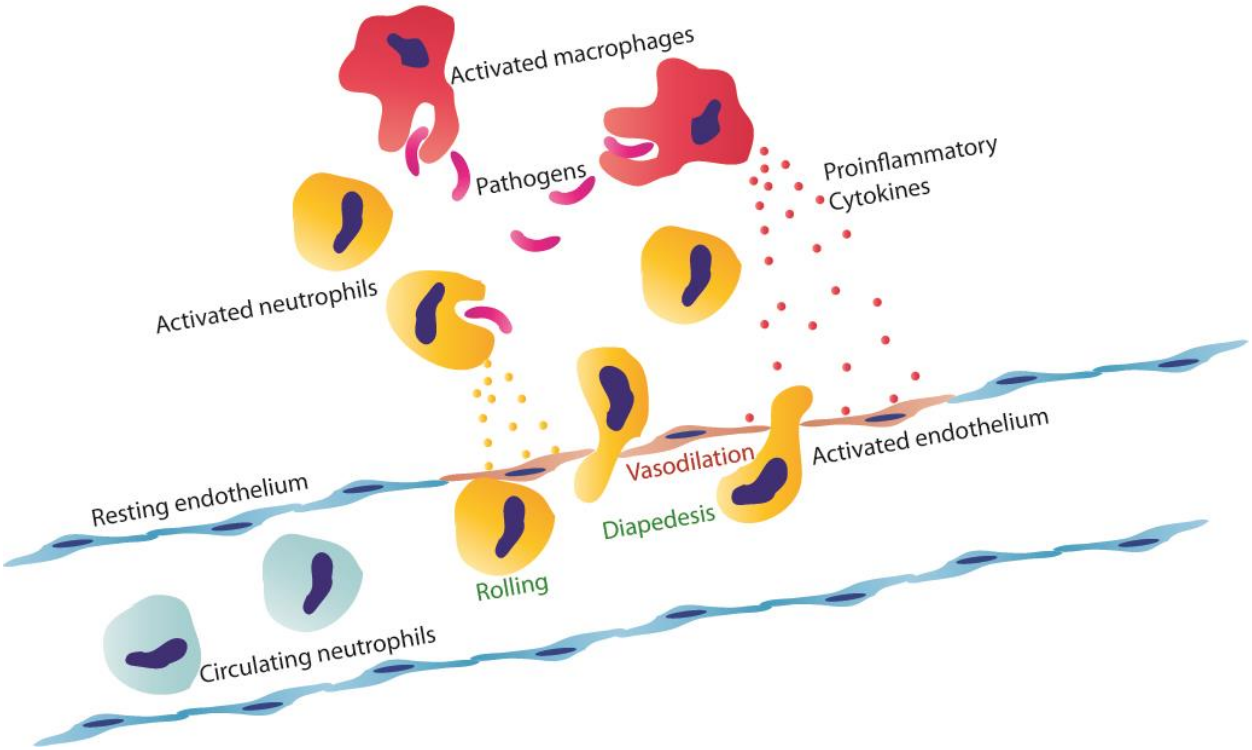

Figure 1.1: The inflammatory response of vascularized tissue.
Irritated inflammatory tissue recruits leukocytes, such as neutrophils and monocyte/macrophages through activated endothelial cells, involving the steps of rolling, strengthening of adhesion, crawling, and paracellular/transcellular migration (diapedesis). Subsequently, migrated leukocytes secrete pro-inflammatory cytokines and chemokines that further activates the surrounding tissue to recruit more immune cells. (Illustration designed and rendered by Spencer Park)

In many cases, some form of chronic inflammation precedes tumor development. Initially, the inflammatory responses as these are a part of normal host defense. However, tumorigenic pathogens can sabotage host's immune response and establish chronic inflammation, facilitating cancer development. Persistent *Helicobacter pylori* infection is associated with gastric cancer and mucosa-associated lymphoid tissue lymphoma[19], while infections with hepatitis B or C viruses increase the risk of hepatocellular carcinoma[17, 20].

Conversely, by mirroring wounds, tumors can initiate inflammation. Once established, solid malignancies trigger an intrinsic inflammatory response that launches a pro-tumor microenvironment[21]. Tumors begin remodeling the neighboring stroma through secretion of chemokines/cytokines, recruitment of leukocytes, and initiation of angiogenesis[22, 23]. As a result of the transformation, tumor microenvironment is composed of innate and adaptive immune cells co-existing with tumor cells as well as stromal cells, including mesenchymal cells, endothelial cells, and fibroblasts[24]. During this development, malignancies demand increasingly higher blood supply. When the tumor's metabolic needs are no longer met, the cells receiving insufficient levels of nutrients die, forming a necrotic core and releasing proinflammatory cytokines, such as IL-1[25]. The augmented inflammation promotes further angiogenesis and the resultant wave of immune cells provide the tumor with necessary cytokines and growth factors[17].

Intercellular adhesion molecule-1 in inflammation and cancer

Much attention has been given to the molecular and cellular pathways linking inflammation with cancer and the local tumor environment to identify new target molecules that could lead to improved diagnosis and treatment[9, 21]. Among the many molecular players involved in the complex response, central to the induction of inflammation is the transcription factor known as, nuclear factor kappa-light-chain-enhancer of activated B cells (NF-κB). Malignant epithelial cells manipulate NF-κB, which controls various genes involved in inflammation, to be constitutively active. For example, in tumor-associated macrophages, activated NF-κB causes polarization of the cells into a phenotype that suppresses cytotoxic T lymphocyte response, increases angiogenesis, and promotes tumor development (Fig. 1.2)[26].

One of the genes induced by the activation of NF-κB is intercellular adhesion molecule (ICAM)-1, which is of particular interest for its highly sensitive and localized expression in response to inflammatory signals. Intercellular adhesion molecule (ICAM)-1 is a transmembrane glycoprotein belonging to the immunoglobulin superfamily of adhesion molecules and is composed of five extracellular Immunoglobulin G-like domains. ICAM-1 is continuously expressed at low levels on various cell types including fibroblasts, endothelial cells, and some leukocytes but is profoundly inducible in inflammation[27, 28]. More specifically, inflammatory mediators, including lipopolysaccharide, IFN-γ, IL-1 and TNF have been shown to cause strong induction of ICAM-1 in a wide variety of tissues and greatly increase binding of leukocytes, facilitating the infiltration of damaged tissues[29].

In line with the increasing reports on the importance of inflammation in tumor progression, ICAM-1 has also been implicated to play a critical role in tumor progression in various types of cancer[30-36], where its over-expression has been correlated to poor

prognosis [35, 37-39]. In addition, the expression level of ICAM-1 has also been linked to cancer metastases, where ICAM-1 facilitates the spread of metastatic cancer cells to secondary sites [40-43]. Not only is ICAM-1 over-expressed on many carcinomas, it is also induced in the inflamed milieu in the vicinity of tumors[9, 44, 45]. This unique expression profile of ICAM-1 throughout solid tumor microenvironment makes ICAM-1 an intriguing molecular target, which holds great potential as an important diagnostic tool for assessing the progression and prognosis of tumors. In therapy, using drug-delivery or immunotherapy methods targeted against ICAM-1 would bypass the efforts often required in identifying proper tumor antigens for each type of cancer.

Lymphocyte function-associated antigen-1

Integrins are members of a versatile family of noncovalently associated α/β heterodimeric cell surface receptors that stabilize cell-cell and cell-extracellular matrix adhesion during immune responses[46]. A type of leukocyte Integrin, $\alpha_L\beta_2$ or lymphocyte function associated antigen (LFA)-1, is constitutively expressed on all leukocytes and is the natural ligand for ICAM-1. Although originally identified using antibodies that inhibit T cell-mediated killing, LFA-1 is also critically important for other leukocyte functions, including adherence to endothelial cells, fibroblasts, and epithelial cells[47, 48]. In resting lymphocytes, the integrin remains in a low affinity state but it is rapidly synchronized to undergo dynamic conformational changes during lymphocyte activation, which greatly increases its binding affinity to ICAM-1 (Fig. 1.3). In addition to the affinity modification, avidity alteration through clustering in the membrane plays an

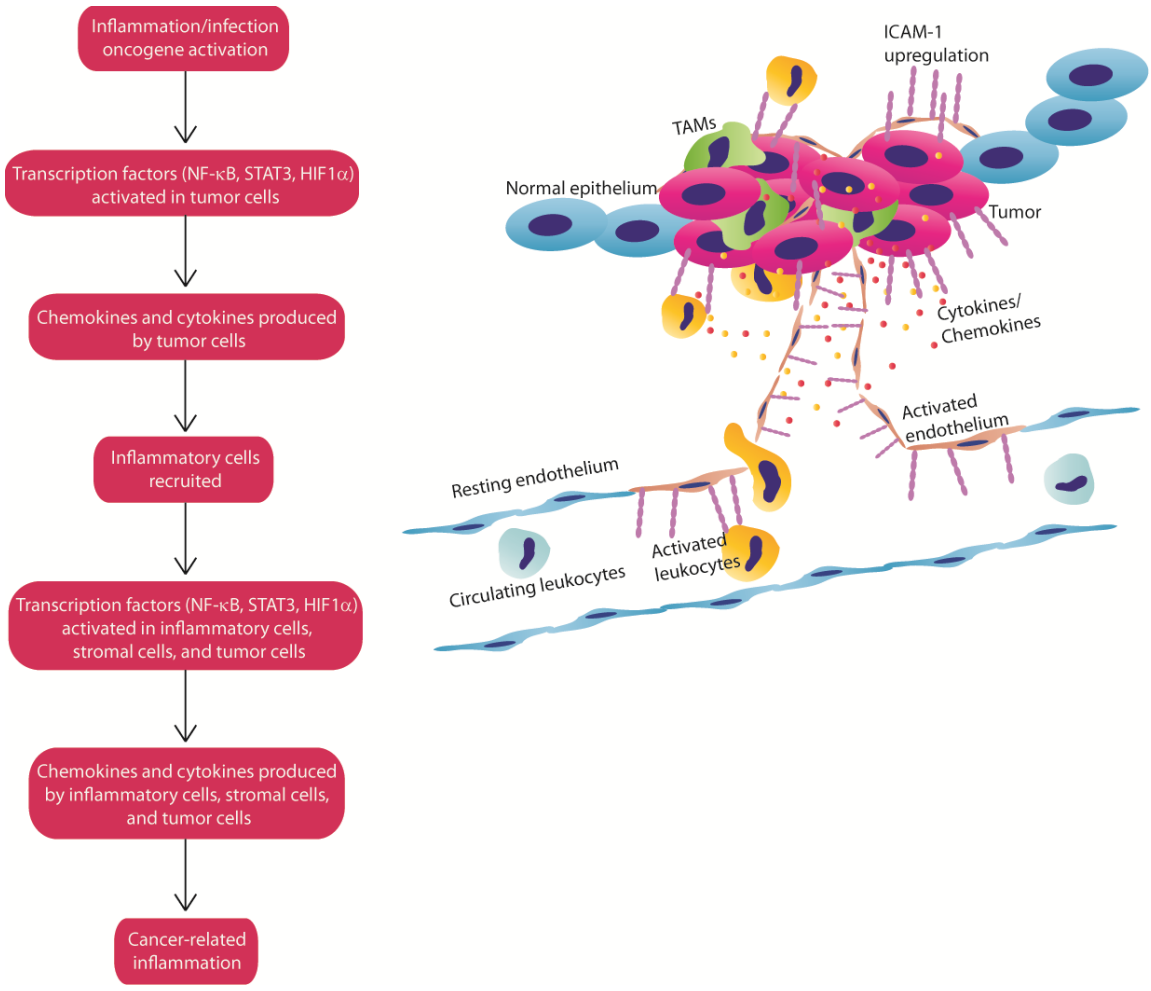

Figure 1.2: Pathways that connect inflammation and cancer.
Various types of oncogene by mutation or infectious conditions augment the risk of developing cancer. Activation of transcription factors, mainly nuclear factor-κB (NF-κB), in tumor cells coordinate the production of inflammatory cytokines and chemokines, as well as certain adhesion molecules like ICAM-1. These factors recruit and activate various leukocytes leading to accumulation of inflammatory mediators and ultimately an inflammatory microenvironment. (Illustration designed and rendered by Spencer Park)

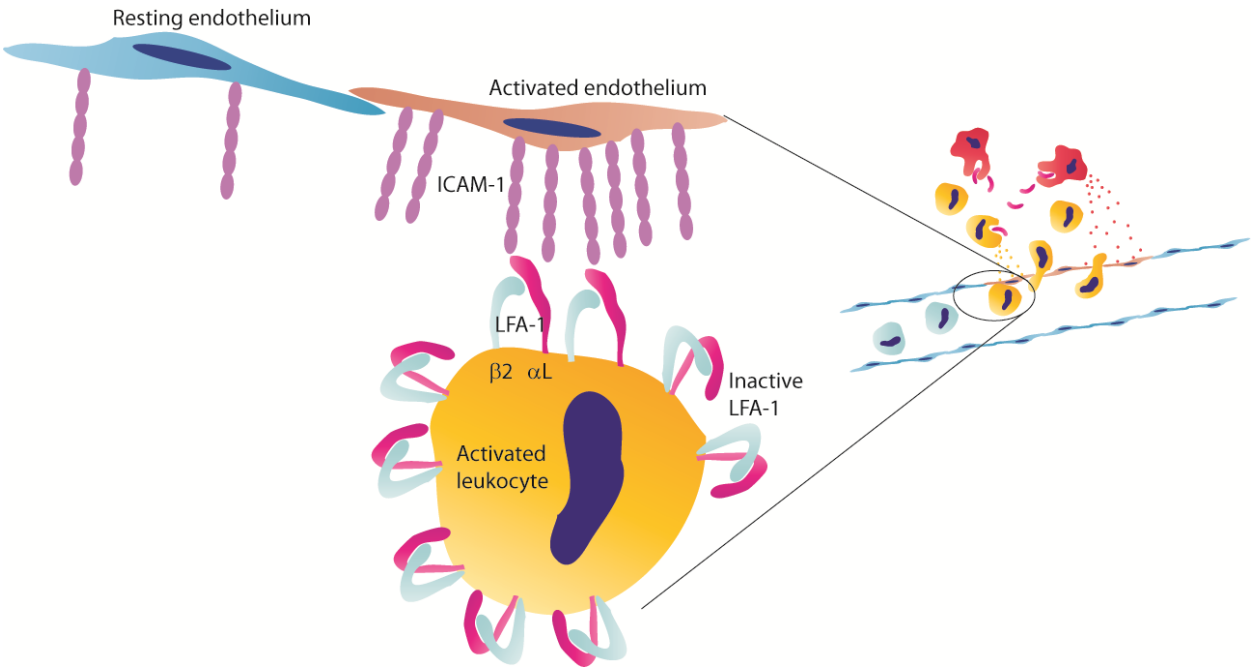

Figure 1.3: LFA-1 and the physiological ligand, ICAM-1.
Activated LFA-1 binds its physiological ligand, ICAM-1, through the top of the extended form. ICAM-1 is upregulated on inflamed endothelial cells. (Illustration designed and rendered by Spencer Park)

important role in regulating adhesiveness of LFA-1 to ICAM-1[49]. Regulation of LFA-1 activation is, therefore, pivotal for controlling leukocyte trafficking and immune responses in health and diseases.

LFA-1 structure and affinity-tuning

LFA-1 contains a von Willebrand factor-type A domain, the inserted (I) domain in the α_L subunit[50], which is responsible in mediating the interaction between LFA-1 integrin and ICAM-1. The I domain has a Mg^{2+} ion coordinated at the metal ion-dependent adhesion site (MIDAS) located within the ligand-binding face[50, 51], explaining the Mg^{2+} requirement in lymphocyte adhesion. The affinity of the α_L I domain for ICAM-1, during LFA-1 activation, is controlled by downward dislodgment of its C-terminal α7 helix by 10 Å, which causes allosteric restructuring of MIDAS into the 'open' conformation and increases the affinity for ICAM-1 by 10,000-fold (Fig. 1.4)[52, 53]. As part of an integrin molecule, the 'open' conformation of MIDAS is stabilized when the linker region after the α7-helix interacts with the adjacent I-like domain of the β subunit to retain the α7-helix in the downward position.

To stabilize the 'open' conformation in an isolated, standalone I domain unit, however, previous studies have introduced a pair of cysteines within αL I domain, essentially anchoring the α7 helix[50, 52]. Some other studies demonstrated that single point mutations, can lead to higher affinity of the I domains. When directed evolution, a method where random mutagenesis in protein of interest is coupled with functional screening, was first applied to α_L I domain, hot spots for activation were identified. In this study, yeast surface display system was used to screen for

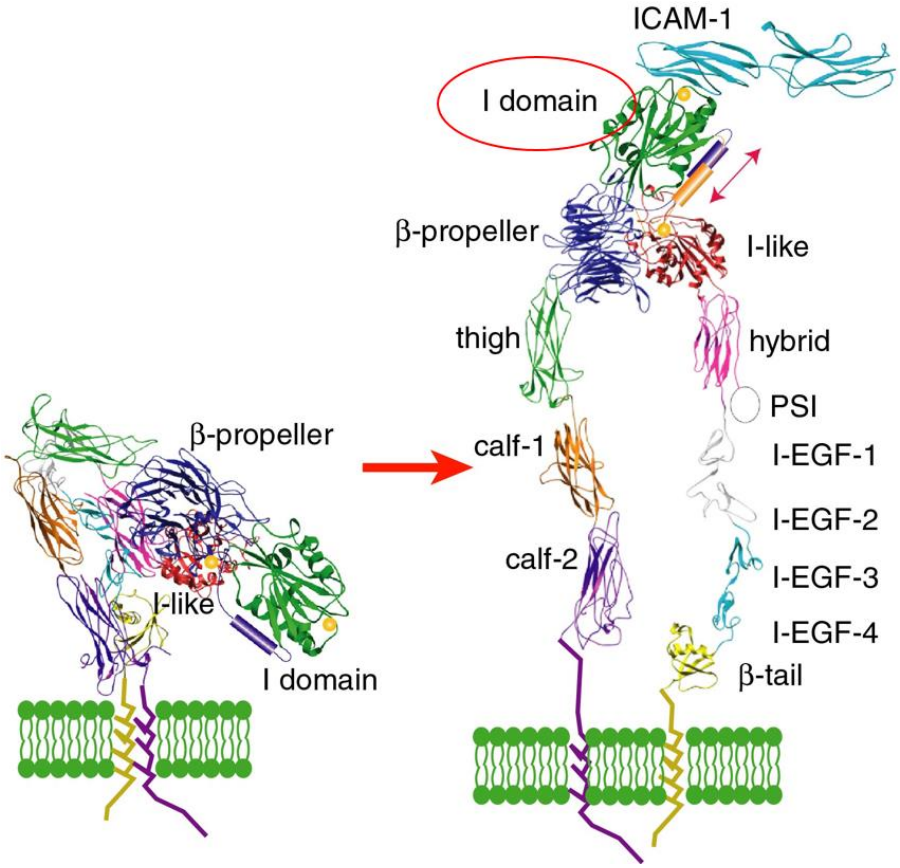

Figure 1.4: Global conformational rearrangements of integrin.
Inactive integrin exists in a bent conformation with the headpiece folded over the tailpiece. Active integrin exhibits the switchblade-like extension and the separation of the two subunits (α and β) at the cytoplasmic and transmembrane domains. Ribbon diagrams were made using PyMOL (DeLano, W.L.).

high affinity I domains using conformation specific antibodies and ICAM-1 for both structural and functional analysis. From a yeast library of I domains containing random mutations, select mutations exhibited affinities to ICAM-1 that was up to 200,000-fold higher than the wild-type[54]. Without a priori structural knowledge of I domain, which undergoes complex allosteric changes, this study isolated I domain mutants with varying affinities to ICAM-1. The discovered affinities ranged from 1500 μM to 6 nM, a wide range that allows screening of the mutants in different therapeutic methods of different disease settings to allow for optimal therapeutic index.

Inflammation-targeted chemotherapeutic delivery

The utmost ambition in chemotherapeutic delivery is to differentially deliver the drug to the site of tumor growth and achieve necessary local concentrations for effective therapeutic index. In this endeavor, utilizing nanoparticles is advantageous over the conventional methods of either delivering drugs directly or as molecular conjugates. Nanoparticles can protect the therapeutics in their active form from chemical and enzymatic degradation, enhance the pharmacokinetics, bioavailability, and biodistribution, and circumventing the need for chemical modification of therapeutic agents, which often leads to reduced potency and stability [55, 56].

Most of these delivery vehicles are composed of lipids, polymers, or proteins that have the ability to encapsulate or associate with various therapeutics, including small molecule drugs, siRNAs, and DNA. One of the first drug-carrier-based therapeutics to be approved by the Food and Drug Administration for clinical use was Doxil in treating ovarian cancer and multiple

myeloma[57]. However, traditional passive distribution methods that are utilized by Doxil face difficulties in achieving high local concentration in tumors [58]. Though initially they are able to accumulate in tumor vicinity due to the leaky vasculature that surrounds tumors through a mechanism called enhanced permeation and retention (EPR) effect, they are quickly forced back into circulation by the high interstitial fluid pressure and dysfunctional lymphatic vessels present in tumor microenvironment [59-63]. Since drug carriers are designed for slow release of payloads, they often are not able to release sufficient amount of drugs during the short span of time in tumor vicinity before they are forced back into circulation.

To overcome such physiological barriers, local applications of hyperthermia [64], photosensitization [65], and ultrasound [66] have been used to increase the permeability of tumor vessels. Alternatively, new types of nanoparticles to address such problems have also been engineered, including immunotargeting or site-directed carriers, many of which are specific to ligand/receptor interactions[56]. Active targeting methods, as such, allow the particles to be taken up by target cells after escaping circulation. This allows the accumulation of therapeutics at the site of disease to correlate with the presence of target antigens, thereby significantly minimizing the required effective dosage, and the associated cytotoxicity and unwanted side effects.

Active targeting requires identification and targeting of tumor antigens, however, which is difficult to achieve. Not only is there a limited number of known tumor antigens, tumors are genetically unstable, causing them to be heterogeneous in their antigen expression. Due to the highly inconsistent nature of these antigens, specific delivery to tumors via active targeting has proven to be limited in efficacy. We believe that by shifting from this mainstream practice and

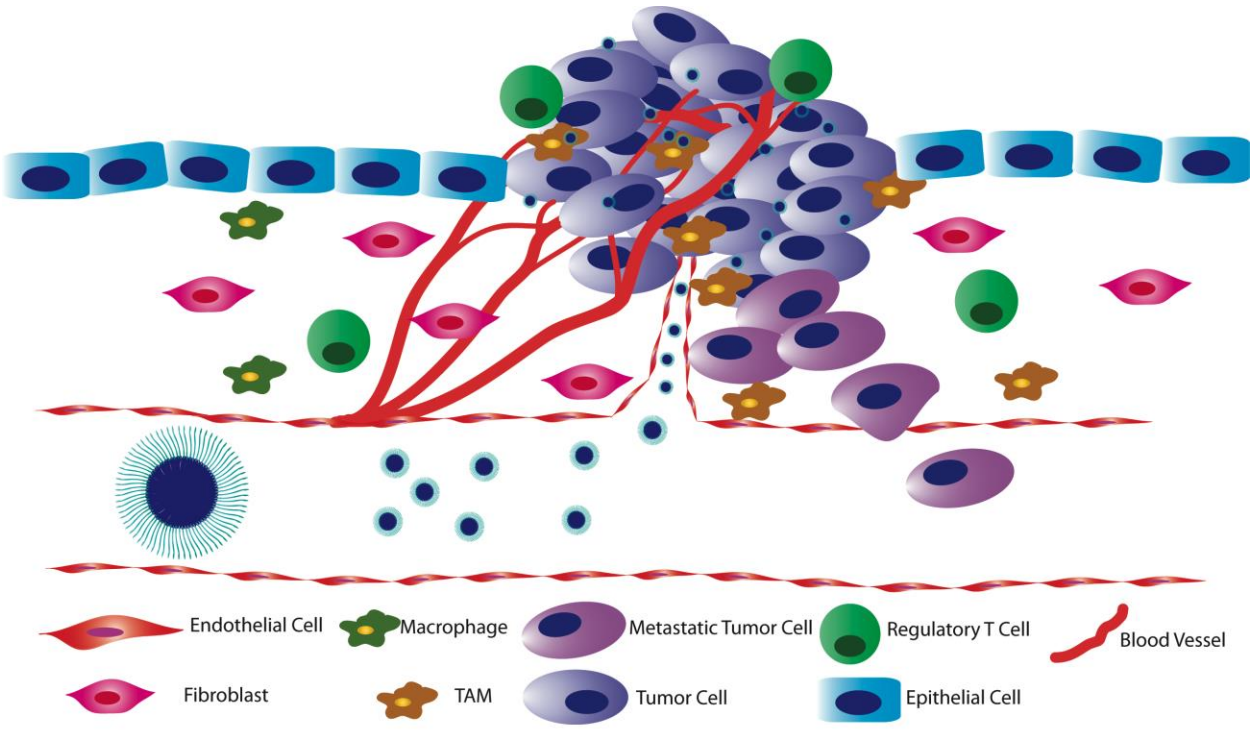

Figure 1.5: Targeted payload delivery to inflamed tumor microenvironment.
The primary tumor microenvironment consists of tumor cells surrounded by normal epithelial cells, endothelial cells, and various immune cells. Despite the presence of heterogeneous cells, the common expression of inflammation markers, such as ICAM-1, makes targeting inflammation for payload delivery efficient.

relying more on other features of tumor microenvironment, such as the presence of inflammation, will help to circumvent such hurdles (Fig. 1.5).

Drug carriers possessing the ability to target inflammation markers can be directed to the tumor stromal constituents, including the vasculature [67, 68] and/or tumor-associated macrophages[69]. Because the expression levels of cell adhesion molecules such as ICAM-1 and VCAM1 are highly upregulated at the sites of inflammation, they have been extensively targeted for payload delivery[70-72]. Moreover, multimeric clustering of these molecules promotes rapid endocytosis, allowing delivery systems to reach into the cytosol of target cells quickly, an important trait for delivery systems[73]. Therefore, it can be speculated that drug carriers designed to target the pivotal inflammatory signaling would be broadly effective in eradicating not only carcinoma cells expressing inflammatory markers but also those lacking by subverting the tumor stromal cells.

Development of safe immunotherapy against solid tumors

In the recent years, the use of engineered T cells directed against specific antigens has demonstrated great potential in HIV and cancer therapy. Along with immune checkpoint blockade[74], this approach has triggered a paradigm shift in cancer immunotherapy. The first reported use of adoptive cellular therapy for tumor allografts was more than 60 years ago[75] but the results of the early trials using allogeneic or autologous lymphocytes were not promising. In 1989 and 1990, the concept of introducing genetic materials encoding for an antibody into a T cell hybridoma was first described[76, 77]. This was quickly followed by

studies demonstrating that a single polypeptide chain is sufficient to mimic the signaling capacity of the T cell receptor (TCR)[78-80]. Together, above studies verified the possibility of redirecting T cells to an antigen of choice independent of MHC restrictions and gave birth to the concept of chimeric antigen receptors (CARs).

A chimeric antigen receptor is made up of an antigen recognition domain and the TCR signaling domain. The antigen recognition domain is usually a single chain variable fragment (scFv) adopted from an antibody against the antigen of interest. Most of the currently identified and targeted tumor antigens are self-antigens that are aberrantly expressed during malignancy. The affinity of TCRs for these antigens is considerably lower than affinity for viral antigens, revealing the weight of central tolerance on T cell repertoire to self-antigens[81]. In contrast, scFvs obtained through powerful screening methods, such as phage display, exhibit much higher affinities[82].

The signaling machinery of CARs has evolved significantly from the first generation configuration of having only the CD3ζ signaling domain[83]. The first-generation CAR trials in cancer patients proved disappointing. It is predicted that the first-generation CARs became anergic without the costimulation input[84, 85]. Since then, in an effort to boost T cell persistence/proliferation, several costimulatory endodomains were tested. Second-generation CARs included a costimulatory signaling domain such as CD28 or 4-1BB [86, 87], and third-generation CARs included a combination of costimulatory endodomains in addition to CD3ζ [88]. Many trials are currently ongoing to test second- and third-generation CARs.

The most successful CAR clinical trials have been against hematological cancers. Chemotherapy-refractory leukemia and lymphoma patients receiving CD19-specific CAR T cells

have shown especially promising results[89-92], where the patients exhibited remissions lasting more than two years[89]. In these studies, low doses of T cells demonstrated explosive in vivo expansion and efficient killing of $CD19^+$ B cells, including aplasia of normal B cells.

Unfortunately, the clinical results for CAR-T cells targeting solid cancers have been much less encouraging. The two most favorable trials targeted sarcoma using ErbB2 CAR, where 4 of 17 patients showed stable disease[93], and neuroblastoma using GD2 CAR, where 3 of 11 patients showed complete remissions[94]. The reason for CAR T cells under-performing in solid tumor models is thought to be multifactorial. First, CAR T cells must efficiently gather at the tumor site despite potential incompatibility between chemokine receptors present on T cell surface and chemokines secreted by tumors[95]. Second, CAR T cells must infiltrate physical barriers posed by tumor stroma and interact with tumor cells in spite of possible antigen loss or heterogeneity. Third, CAR T cells must overcome hypoxia, oxidative stress, lack of nutrients, acidosis, and immune-suppression[96, 97]. The exciting success of CAR therapy in hematologic malignancies is fueling the application of CARs in solid tumors. However, a more complete grasp over the major hurdles seen in solid tumors will be necessary to optimize CAR engineering.

As with most cancer therapies, there is an emerging set of toxicities associated with CAR-T cell therapies. In the case of CD19 CAR-T cells, these toxicities include B cell aplasia, tumor lysis syndrome (TLS), and cytokine release syndrome (CRS). Intravenous immunoglobulin can be used to replace quantitative antibody deficiency. TLS has been managed successfully by standard supportive therapy, including hydration, alkalinization, allopurinol, and rasburicase[98]. In patients with B cell malignancies, CRS occurs at the time of peak levels of

CAR T cells in blood and bone marrow. Corticosteroids and cytokine blockade are currently being evaluated for patients with CLL and ALL.

In treating solid tumors, on-target off-tumor toxicity is the major problem as most solid tumor antigens are not exclusively present on tumors. T cells expressing a CAR specific for carbonic anhydrase IX, an antigen present on the surface of clear cell renal cell carcinoma, caused an unexpected serious hepatic toxicity in several patients[99]. This is likely due to carbonic anhydrase IX expression in the biliary tract. This study indicates that CAR targets must be carefully chosen to avoid such adverse effects, or that on-target off-tumor toxicity must be mitigated through additional safety features, such as suicide switches under the control of an inducible promoter[100] or transient expression systems[101].

Dissertation outline

In this dissertation, I demonstrate the application of various LFA-1 I domain mutants exhibiting wide range of affinities toward its ligand, ICAM-1, for targeting tumor-associated inflammation. Through the delivery of diagnostic agents, chemotherapeutics, as well as immunotherapeutics, the following chapters demonstrate that the affinity enhancements achieved by directed evolution bring the affinity of I domains into the range optimal for numerous applications.

In the first chapters, I used amphiphilic polymeric nanoparticles to encapsulate water-insoluble chemotherapeutic and anti-inflammatory drugs in the hydrophobic core, while functionalizing the surface with LFA-1 I domain. The I domain mutants displaying different

degrees of affinity towards ICAM-1 were first screened in an *in vitro* setting to determine the most competent targeting agent.

In chemotherapy, the major obstacle lies in delivering sufficient amount of drugs to tumors to have desired effects, thereby reducing the drugs concentrations in healthy tissues. Thus, after observing the potent ICAM-1-specific drug delivery and killing by nanoparticles functionalized with the highest affinity I domain mutant, we carried out the subsequent *in vivo* mouse studies with the same formulation. I found that by being directed by the high affinity I domain, nanoparticles preferentially accumulated in inflamed mouse stromal cells that upregulated the expression of ICAM-1. Though the specific cytotoxic effect was enhanced in the tumor model expressing a high level of ICAM-1, ICAM-1$^-$ tumor growth was also arrested due to the toxicity on the tumor-supporting cells. The associated systemic toxicity with this drug delivery method was determined to be low and transient.

To demonstrate the versatile applicability of LFA-1 I domain in cancer therapy, we replaced the scFv region of chimeric antigen receptors with different I domain mutants to be applied in immunotherapy. Since target-mediated toxicity is a major concern in engineering CAR T cells for solid tumors, we utilized the various I domain mutants to discriminate tumors overexpressing ICAM-1 from normal tissues. High affinity CAR T cells recognized ICAM-1 expressed at any level, including normal cells, causing systemic toxicity in host and ultimately leading to death. Affinity-tuned CAR T cells exhibited robust anti-tumor lysis but excluded normal tissues. The use of affinity-tuned CAR T cells endows potent CAR T cells with a safe strategy to discriminate targets widely overexpressed on solid tumors

REFERENCES

1. Greaves, M. and S. Shuster, *Responses of skin blood vessels to bradykinin, histamine and 5-hydroxytryptamine.* J Physiol, 1967. **193**(2): p. 255-67.
2. Williams, T.J. and M.J. Peck, *Role of prostaglandin-mediated vasodilatation in inflammation.* Nature, 1977. **270**(5637): p. 530-2.
3. Medzhitov, R., *Origin and physiological roles of inflammation.* Nature, 2008. **454**(7203): p. 428-35.
4. Barton, G.M., *A calculated response: control of inflammation by the innate immune system.* J Clin Invest, 2008. **118**(2): p. 413-20.
5. Nathan, C. and A. Ding, *Nonresolving inflammation.* Cell, 2010. **140**(6): p. 871-82.
6. Libby, P., *Inflammation in atherosclerosis.* Nature, 2002. **420**(6917): p. 868-874.
7. Hotamisligil, G.S., *Inflammation and metabolic disorders.* Nature, 2006. **444**(7121): p. 860-7.
8. Glass, C.K., et al., *Mechanisms underlying inflammation in neurodegeneration.* Cell, 2010. **140**(6): p. 918-34.
9. Coussens, L.M. and Z. Werb, *Inflammation and cancer.* Nature, 2002. **420**(6917): p. 860-7.
10. Ley, K., et al., *Getting to the site of inflammation: the leukocyte adhesion cascade updated.* Nat Rev Immunol, 2007. **7**(9): p. 678-89.
11. Proost, P., A. Wuyts, and J. van Damme, *The role of chemokines in inflammation.* Int J Clin Lab Res, 1996. **26**(4): p. 211-23.
12. Pober, J.S. and W.C. Sessa, *Evolving functions of endothelial cells in inflammation.* Nat Rev Immunol, 2007. **7**(10): p. 803-15.
13. Giagulli, C., et al., *RhoA and zeta PKC control distinct modalities of LFA-1 activation by chemokines: critical role of LFA-1 affinity triggering in lymphocyte in vivo homing.* Immunity, 2004. **20**(1): p. 25-35.
14. Kinashi, T., *Intracellular signalling controlling integrin activation in lymphocytes.* Nat Rev Immunol, 2005. **5**(7): p. 546-59.
15. Springer, T.A., *Traffic signals for lymphocyte recirculation and leukocyte emigration: the multistep paradigm.* Cell, 1994. **76**(2): p. 301-14.
16. Springer, T.A., *Traffic signals on endothelium for lymphocyte recirculation and leukocyte emigration.* Annu Rev Physiol, 1995. **57**: p. 827-72.
17. Karin, M., *Nuclear factor-kappaB in cancer development and progression.* Nature, 2006. **441**(7092): p. 431-6.
18. Hanahan, D. and R.A. Weinberg, *Hallmarks of cancer: the next generation.* Cell, 2011. **144**(5): p. 646-74.
19. de Martel, C. and S. Franceschi, *Infections and cancer: established associations and new hypotheses.* Crit Rev Oncol Hematol, 2009. **70**(3): p. 183-94.
20. Wu, S., et al., *A human colonic commensal promotes colon tumorigenesis via activation of T helper type 17 T cell responses.* Nat Med, 2009. **15**(9): p. 1016-22.
21. Mantovani, A., et al., *Cancer-related inflammation.* Nature, 2008. **454**(7203): p. 436-44.
22. Germano, G., P. Allavena, and A. Mantovani, *Cytokines as a key component of cancer-related inflammation.* Cytokine, 2008. **43**(3): p. 374-9.

23. Sica, A., P. Allavena, and A. Mantovani, *Cancer related inflammation: the macrophage connection.* Cancer Lett, 2008. **267**(2): p. 204-15.
24. de Visser, K.E., A. Eichten, and L.M. Coussens, *Paradoxical roles of the immune system during cancer development.* Nat Rev Cancer, 2006. **6**(1): p. 24-37.
25. Vakkila, J. and M.T. Lotze, *Inflammation and necrosis promote tumour growth.* Nat Rev Immunol, 2004. **4**(8): p. 641-8.
26. Hagemann, T., et al., *"Re-educating" tumor-associated macrophages by targeting NF-kappaB.* J Exp Med, 2008. **205**(6): p. 1261-8.
27. Marlin, S.D. and T.A. Springer, *Purified intercellular adhesion molecule-1 (ICAM-1) is a ligand for lymphocyte function-associated antigen 1 (LFA-1).* Cell, 1987. **51**(5): p. 813-9.
28. Dustin, M.L., et al., *Induction by IL 1 and interferon-gamma: tissue distribution, biochemistry, and function of a natural adherence molecule (ICAM-1).* J Immunol, 1986. **137**(1): p. 245-54.
29. Rothlein, R., et al., *A human intercellular adhesion molecule (ICAM-1) distinct from LFA-1.* J Immunol, 1986. **137**(4): p. 1270-4.
30. Ogawa, Y., et al., *Expression of intercellular adhesion molecule-1 in invasive breast cancer reflects low growth potential, negative lymph node involvement, and good prognosis.* Clin Cancer Res, 1998. **4**(1): p. 31-6.
31. Kelly, C.P., et al., *Human colon cancer cells express ICAM-1 in vivo and support LFA-1-dependent lymphocyte adhesion in vitro.* Am J Physiol, 1992. **263**(6 Pt 1): p. G864-70.
32. Passlick, B., et al., *Expression of major histocompatibility class I and class II antigens and intercellular adhesion molecule-1 on operable non-small cell lung carcinomas: frequency and prognostic significance.* Eur J Cancer, 1994. **30A**(3): p. 376-81.
33. Tomita, Y., et al., *Expression of intercellular adhesion molecule-1 (ICAM-1) on renal-cell cancer: possible significance in host immune responses.* Int J Cancer, 1990. **46**(6): p. 1001-6.
34. Koyama, S., T. Ebihara, and K. Fukao, *Expression of intercellular adhesion molecule 1 (ICAM-1) during the development of invasion and/or metastasis of gastric carcinoma.* J Cancer Res Clin Oncol, 1992. **118**(8): p. 609-14.
35. Shimoyama, S., et al., *Overexpression of intercellular adhesion molecule-1 (ICAM-1) in pancreatic adenocarcinoma in comparison with normal pancreas.* Pancreas, 1997. **14**(2): p. 181-6.
36. Hoesel, B. and J.A. Schmid, *The complexity of NF-kappaB signaling in inflammation and cancer.* Mol Cancer, 2013. **12**: p. 86.
37. Buitrago, D., et al., *Intercellular adhesion molecule-1 (ICAM-1) is upregulated in aggressive papillary thyroid carcinoma.* Ann Surg Oncol, 2012. **19**(3): p. 973-80.
38. Schroder, C., et al., *Prognostic value of intercellular adhesion molecule (ICAM)-1 expression in breast cancer.* J Cancer Res Clin Oncol, 2011. **137**(8): p. 1193-201.
39. Roland, C.L., et al., *Tumor-derived intercellular adhesion molecule-1 mediates tumor-associated leukocyte infiltration in orthotopic pancreatic xenografts.* Exp Biol Med (Maywood), 2010. **235**(2): p. 263-70.
40. Buitrago, D., et al., *Intercellular Adhesion Molecule-1 (ICAM-1) is Upregulated in Aggressive Papillary Thyroid Carcinoma.* Annals of Surgical Oncology, 2012. **19**(3): p. 973-980.

41. Schroder, C., et al., *Prognostic value of intercellular adhesion molecule (ICAM)-1 expression in breast cancer.* Journal of Cancer Research and Clinical Oncology, 2011. **137**(8): p. 1193-1201.
42. Roland, C.L., et al., *Tumor-derived intercellular adhesion molecule-1 mediates tumor-associated leukocyte infiltration in orthotopic pancreatic xenografts.* Experimental Biology and Medicine, 2010. **235**(2): p. 263-269.
43. Roland, C.L., et al., *ICAM-1 expression determines malignant potential of cancer.* Surgery, 2007. **141**(6): p. 705-7.
44. Grivennikov, S.I., F.R. Greten, and M. Karin, *Immunity, inflammation, and cancer.* Cell, 2010. **140**(6): p. 883-99.
45. Chen, X., et al., *Inflamed leukocyte-mimetic nanoparticles for molecular imaging of inflammation.* Biomaterials, 2011. **32**(30): p. 7651-61.
46. Kurzinger, K., et al., *A novel lymphocyte function-associated antigen (LFA-1): cellular distribution, quantitative expression, and structure.* J Immunol, 1981. **127**(2): p. 596-602.
47. Gahmberg, C.G., M. Tolvanen, and P. Kotovuori, *Leukocyte adhesion - Structure and function of human leukocyte beta(2)-integrins and their cellular ligands.* European Journal of Biochemistry, 1997. **245**(2): p. 215-232.
48. Larson, R.S. and T.A. Springer, *Structure and Function of Leukocyte Integrins.* Immunological Reviews, 1990. **114**: p. 181-217.
49. van Kooyk, Y., S.J. van Vliet, and C.G. Figdor, *The actin cytoskeleton regulates LFA-1 ligand binding through avidity rather than affinity changes.* Journal of Biological Chemistry, 1999. **274**(38): p. 26869-26877.
50. Shimaoka, M., J. Takagi, and T.A. Springer, *Conformational regulation of integrin structure and function.* Annu Rev Biophys Biomol Struct, 2002. **31**: p. 485-516.
51. Lee, J.O., et al., *Crystal structure of the A domain from the alpha subunit of integrin CR3 (CD11b/CD18).* Cell, 1995. **80**(4): p. 631-8.
52. Shimaoka, M., et al., *Reversibly locking a protein fold in an active conformation with a disulfide bond: integrin alphaL I domains with high affinity and antagonist activity in vivo.* Proc Natl Acad Sci U S A, 2001. **98**(11): p. 6009-14.
53. Shimaoka, M., et al., *Computational design of an integrin I domain stabilized in the open high affinity conformation.* Nat Struct Biol, 2000. **7**(8): p. 674-8.
54. Jin, M., et al., *Directed evolution to probe protein allostery and integrin I domains of 200,000-fold higher affinity.* Proc Natl Acad Sci U S A, 2006. **103**(15): p. 5758-63.
55. Davis, M.E., Z.G. Chen, and D.M. Shin, *Nanoparticle therapeutics: an emerging treatment modality for cancer.* Nat Rev Drug Discov, 2008. **7**(9): p. 771-82.
56. Allen, T.M. and P.R. Cullis, *Drug delivery systems: entering the mainstream.* Science, 2004. **303**(5665): p. 1818-22.
57. Juliano, R., *Clinical implications of basic research: Bugging tumors to put drugs on target.* New England Journal of Medicine, 2007. **356**(9): p. 954-955.
58. Hambley, T.W. and W.N. Hait, *Is anticancer drug development heading in the right direction?* Cancer Res, 2009. **69**(4): p. 1259-62.
59. Yuan, F., et al., *Vascular permeability in a human tumor xenograft: molecular size dependence and cutoff size.* Cancer Res, 1995. **55**(17): p. 3752-6.

60. Li, S.D. and L. Huang, *Pharmacokinetics and biodistribution of nanoparticles.* Mol Pharm, 2008. **5**(4): p. 496-504.
61. Jain, R.K., *Transport of molecules, particles, and cells in solid tumors.* Annu Rev Biomed Eng, 1999. **1**: p. 241-63.
62. Danquah, M.K., X.A. Zhang, and R.I. Mahato, *Extravasation of polymeric nanomedicines across tumor vasculature.* Adv Drug Deliv Rev, 2011. **63**(8): p. 623-39.
63. Jain, R.K. and T. Stylianopoulos, *Delivering nanomedicine to solid tumors.* Nat Rev Clin Oncol, 2010. **7**(11): p. 653-64.
64. Kong, G., R.D. Braun, and M.W. Dewhirst, *Hyperthermia enables tumor-specific nanoparticle delivery: effect of particle size.* Cancer Res, 2000. **60**(16): p. 4440-5.
65. Chen, B., et al., *Tumor vascular permeabilization by vascular-targeting photosensitization: effects, mechanism, and therapeutic implications.* Clin Cancer Res, 2006. **12**(3 Pt 1): p. 917-23.
66. Watson, K.D., et al., *Ultrasound increases nanoparticle delivery by reducing intratumoral pressure and increasing transport in epithelial and epithelial-mesenchymal transition tumors.* Cancer Res, 2012. **72**(6): p. 1485-93.
67. Sugahara, K.N., et al., *Tissue-Penetrating Delivery of Compounds and Nanoparticles into Tumors.* Cancer Cell, 2009. **16**(6): p. 510-520.
68. Nilsson, F., et al., *Targeted delivery of tissue factor to the ED-B domain of fibronectin, a marker of angiogenesis, mediates the infarction of solid tumors in mice.* Cancer Res, 2001. **61**(2): p. 711-6.
69. Turk, M.J., D.J. Waters, and P.S. Low, *Folate-conjugated liposomes preferentially target macrophages associated with ovarian carcinoma.* Cancer Lett, 2004. **213**(2): p. 165-72.
70. Muzykantov, V.R., *Targeting of superoxide dismutase and catalase to vascular endothelium.* Journal of Controlled Release, 2001. **71**(1): p. 1-21.
71. Muro, S., et al., *Endothelial targeting of high-affinity multivalent polymer nanocarriers directed to intercellular adhesion molecule 1.* Journal of Pharmacology and Experimental Therapeutics, 2006. **317**(3): p. 1161-1169.
72. Kelly, K.A., et al., *Detection of vascular adhesion molecule-1 expression using a novel multimodal nanoparticle.* Circulation Research, 2005. **96**(3): p. 327-336.
73. Muro, S., E.H. Schuchman, and V.R. Muzykantov, *Lysosomal enzyme delivery by ICAM-1-targeted nanocarriers bypassing glycosylation- and clathrin-dependent endocytosis.* Mol Ther, 2006. **13**(1): p. 135-41.
74. Topalian, S.L., C.G. Drake, and D.M. Pardoll, *Immune checkpoint blockade: a common denominator approach to cancer therapy.* Cancer Cell, 2015. **27**(4): p. 450-61.
75. Mitchison, N.A., *Studies on the Immunological Response to Foreign Tumor Transplants in the Mouse .1. The Role of Lymph Node Cells in Conferring Immunity by Adoptive Transfer.* Journal of Experimental Medicine, 1955. **102**(2): p. 157-177.
76. Gross, G., T. Waks, and Z. Eshhar, *Expression of Immunoglobulin-T-Cell Receptor Chimeric Molecules as Functional Receptors with Antibody-Type Specificity.* Proceedings of the National Academy of Sciences of the United States of America, 1989. **86**(24): p. 10024-10028.

77. Goverman, J., et al., *Chimeric Immunoglobulin T-Cell Receptor Proteins Form Functional Receptors - Implications for T-Cell Receptor Complex-Formation and Activation.* Cell, 1990. **60**(6): p. 929-939.
78. Irving, B.A. and A. Weiss, *The Cytoplasmic Domain of the T-Cell Receptor Zeta-Chain Is Sufficient to Couple to Receptor-Associated Signal Transduction Pathways.* Cell, 1991. **64**(5): p. 891-901.
79. Letourneur, F. and R.D. Klausner, *T-Cell and Basophil Activation through the Cytoplasmic Tail of T-Cell-Receptor Zeta-Family Proteins.* Proceedings of the National Academy of Sciences of the United States of America, 1991. **88**(20): p. 8905-8909.
80. Romeo, C. and B. Seed, *Cellular-Immunity to Hiv Activated by Cd4 Fused to T-Cell or Fc Receptor Polypeptides.* Cell, 1991. **64**(5): p. 1037-1046.
81. Aleksic, M., et al., *Different affinity windows for virus and cancer-specific T-cell receptors: implications for therapeutic strategies.* Eur J Immunol, 2012. **42**(12): p. 3174-9.
82. Siegel, D.L., *Translational applications of antibody phage display.* Immunol Res, 2008. **42**(1-3): p. 118-31.
83. Eshhar, Z., et al., *Functional expression of chimeric receptor genes in human T cells.* Journal of Immunological Methods, 2001. **248**(1-2): p. 67-76.
84. Loskog, A., et al., *Addition of the CD28 signaling domain to chimeric T-cell receptors enhances chimeric T-cell resistance to T regulatory cells.* Leukemia, 2006. **20**(10): p. 1819-1828.
85. Brocker, T., *Chimeric Fv-xi or Fv-epsilon receptors are not sufficient to induce activation or cytokine production in peripheral T cells.* Blood, 2000. **96**(5): p. 1999-2001.
86. Krause, A., et al., *Antigen-dependent CD28 signaling selectively enhances survival and proliferation in genetically modified activated human primary T lymphocytes.* Journal of Experimental Medicine, 1998. **188**(4): p. 619-626.
87. Milone, M.C., et al., *Chimeric Receptors Containing CD137 Signal Transduction Domains Mediate Enhanced Survival of T Cells and Increased Antileukemic Efficacy In Vivo.* Molecular Therapy, 2009. **17**(8): p. 1453-1464.
88. Till, B.G., et al., *CD20-specific adoptive immunotherapy for lymphoma using a chimeric antigen receptor with both CD28 and 4-1BB domains: pilot clinical trial results.* Blood, 2012. **119**(17): p. 3940-3950.
89. Porter, D.L., et al., *Chimeric antigen receptor-modified T cells in chronic lymphoid leukemia.* N Engl J Med, 2011. **365**(8): p. 725-33.
90. Brentjens, R.J., et al., *Safety and persistence of adoptively transferred autologous CD19-targeted T cells in patients with relapsed or chemotherapy refractory B-cell leukemias.* Blood, 2011. **118**(18): p. 4817-28.
91. Kochenderfer, J.N., et al., *B-cell depletion and remissions of malignancy along with cytokine-associated toxicity in a clinical trial of anti-CD19 chimeric-antigen-receptor-transduced T cells.* Blood, 2012. **119**(12): p. 2709-20.
92. Kochenderfer, J.N., et al., *Eradication of B-lineage cells and regression of lymphoma in a patient treated with autologous T cells genetically engineered to recognize CD19.* Blood, 2010. **116**(20): p. 4099-102.

93. Ahmed, N., et al., *Human Epidermal Growth Factor Receptor 2 (HER2) -Specific Chimeric Antigen Receptor-Modified T Cells for the Immunotherapy of HER2-Positive Sarcoma.* Journal of Clinical Oncology, 2015. **33**(15): p. 1688-96.
94. Louis, C.U., et al., *Antitumor activity and long-term fate of chimeric antigen receptor-positive T cells in patients with neuroblastoma.* Blood, 2011. **118**(23): p. 6050-6.
95. Harlin, H., et al., *Chemokine expression in melanoma metastases associated with CD8+ T-cell recruitment.* Cancer Res, 2009. **69**(7): p. 3077-85.
96. Howie, D., H. Waldmann, and S. Cobbold, *Nutrient Sensing via mTOR in T Cells Maintains a Tolerogenic Microenvironment.* Front Immunol, 2014. **5**: p. 409.
97. Zhou, Q., et al., *Program death-1 signaling and regulatory T cells collaborate to resist the function of adoptively transferred cytotoxic T lymphocytes in advanced acute myeloid leukemia.* Blood, 2010. **116**(14): p. 2484-93.
98. Cairo, M.S., et al., *Recommendations for the evaluation of risk and prophylaxis of tumour lysis syndrome (TLS) in adults and children with malignant diseases: an expert TLS panel consensus.* British Journal of Haematology, 2010. **149**(4): p. 578-586.
99. Lamers, C.H., et al., *Treatment of metastatic renal cell carcinoma with autologous T-lymphocytes genetically retargeted against carbonic anhydrase IX: first clinical experience.* Journal of Clinical Oncology, 2006. **24**(13): p. e20-2.
100. Di Stasi, A., et al., *Inducible Apoptosis as a Safety Switch for Adoptive Cell Therapy.* New England Journal of Medicine, 2011. **365**(18): p. 1673-1683.
101. Zhao, Y., et al., *Multiple injections of electroporated autologous T cells expressing a chimeric antigen receptor mediate regression of human disseminated tumor.* Cancer Res, 2010. **70**(22): p. 9053-61.

CHAPTER 2

SELF-ASSEMBLED NANOPLATFORM FOR TARGETED DELIVERY OF CHEMOTHERAPY AGENTS VIA AFFINITY-REGULATED MOLECULAR INTERACTIONS

This chapter was originally published in Biomaterials (Park, S., Kang, S., Veach, A.J., Vedvyas, Y., Zarnegar, R., Kim, J.Y., Jin, M.M. *Biomaterials*. 2010;31(30):7766-75. ©2010 Elsevier.), and is reprinted with permission. The following is the detailed contribution of authors: S.P., R.Z., M.M.J., and K.J.Y. designed research, performed research, and wrote the paper; S.K., A.V., and Y.V., performed research.

Summary

Site-specific delivery of drugs while minimizing unwanted distribution has been one of the pursued goals in cancer therapy. In this endeavor, we have developed targeted polymeric nanoparticles called amphiphilic urethane acrylate nonionomer (UAN) for encapsulation of diverse water-insoluble drugs and diagnostic agents, as well as for simple and reproducible surface conjugation of targeting ligands. Using monoclonal antibodies or lymphocyte function-associated antigen-1 (LFA-1) I domain engineered for varying affinities to intercellular adhesion molecule (ICAM)-1, we were able to deliver UAN nanoparticles to human cancer cells with the efficiency dependent on the strength of the molecular interactions and the degree of ICAM-1 expression on cell surface. Compared to non-specific uptake of free drugs, targeted delivery of UAN nanoparticles carrying equal amount of drugs produced more potent cytotoxicity. Notably, without the targeting ligands attached, UAN nanoparticles were largely precluded from non-

specific uptake by the cells, resulting in much lower toxicity. The versatility of our UAN nanoparticles in both payload encapsulation and presentation of targeting ligands may facilitate developing a robust platform for evaluating various combinations of cancer drugs and molecular interactions toward developing effective cancer therapy formulations.

Introduction

Nanoparticles are emerging as a powerful platform for delivery of imaging[1] and therapeutic entities[2], particularly due to their potential applications in cancer therapy for early detection, enhanced therapeutic potency, and reduced side effects[3]. For example, microspheres, liposomes, nanoshells, dendrimers, and biodegradable polymers have been utilized as specific drug delivery systems[4]. Compared to the conventional methods of delivering therapeutic agents directly via intravenous or enteral routes, or as molecular conjugates, nanoparticle-mediated delivery may protect the therapeutic agents from chemical and enzymatic degradation and circumvent the need for chemical modification of therapeutic agents, which often leads to reduced potency and stability of drugs[5, 6]. Yet, a successful targeted delivery of nanoparticles needs to address the challenges in delivering hydrophobic payloads, controlling drug release, and accomplishing specific delivery while minimizing adverse immune response[7, 8].

Recently, polymeric nanoparticles have been reported to exhibit characteristics of sustained release, effective solubilization of hydrophobic drugs, and reduced interactions with the reticuloendothelial system[6, 9, 10]. In order to achieve selective targeting by

nanoparticles, targeting ligands are often attached to the surface of the particles. The high surface-to volume ratio in these nanoparticles increases the surface density of ligands, leading to a multivalent, high affinity binding effect[11]. Specific targeting is additionally improved by the enhanced permeation and retention effect in tumor environments due to a leaky vasculature structure, allowing appropriately sized nanoparticles to extravasate[12]. Nanoparticles of certain size range (10-100 nm) have been shown to accumulate more readily in tumors through the retention effect compared to the larger ones, making them optimal for tumor penetration.

To take advantage of these unique characteristics of polymeric nanoparticles, we have developed a versatile nanoparticle platform using amphiphilic urethane acrylate nonionomer (UAN)[13] with two functional layers. The hydrophilic outer shell is coated with a high density of Nickel-nitrilotriacetic acid (Ni-NTA) for simple conjugation of tumor-specific targeting molecules[14] and the hydrophobic core has a large capacity for water-insoluble chemotherapy drugs and imaging agents, where the encapsulation process occurs through the diffusion of hydrophobic molecules from water into the hydrophobic core[14, 15]. Through this approach, we demonstrate efficient encapsulation of water-insoluble fluorescent dyes, 9,10-diphenylanthracene (DPA) and fluorescein isothiocyanate (FITC), and cytotoxic drugs, such as camptothecin, a topoisomerase inhibitor[16], and celastrol, a proteasome inhibitor[17].

Some of the current approaches in targeting tumors include ligands specific to Her2[18], transferrin receptor[19], epidermal growth factor receptor[20], folate receptor[21], integrin αVβ3[22], hyaluronan receptor[23], and chondroitin sulfate[24]. As the target molecule in the present study, we have chosen intercellular adhesion molecule (ICAM)-1. ICAM-1 is present in

low concentrations in the membranes of endothelial cells, and epithelial cells, and a subset of immune cells but is greatly up-regulated in response to inflammatory signals[25, 26]. In addition, constitutive over-expression of ICAM-1 has also been found in many carcinomas, such as breast, colon, non-small cell lung, renal-cell, pancreas, and gastric carcinomas compared to the respective normal epithelial cells[27-32] as well as in the tumor microenvironments, wherein an inflammatory milieu promotes angiogenesis and tumor growth[33].

Though most molecular targeting approaches have been based on antibodies[34] and small peptides[35], herein, we demonstrate ICAM-1 targeting with a native ligand, called the inserted (I) domain derived from lymphocyte function-associated antigen (LFA)-1. LFA-1 is a member of the integrin family, expressed on all leukocytes[36], that mediates leukocyte adhesion to endothelial cells and transmigration into inflamed tissues[37]. We used the I domains that have previously been engineered by various activating mutations (F292A, F292G, F265S/F292G) to increase the affinity to ICAM-1 in a step-wise manner[38]. Using ICAM-1 expressing HeLa cells[39] as a model cancer cell line, we demonstrate specific delivery of UAN encapsulating hydrophobic dyes and therapeutic agents to the cells, in a manner dependent on the affinity between the LFA-1 I domains and ICAM-1, as well as the expression level of ICAM-1.

Experimental Procedures

Synthesis and characterization of NTA-coupled UAN nanoparticles

The synthesis of UAN was previously described[40]. In brief, glycerol propoxylate (n∼5, MW∼1000, Sigma Aldrich) was mixed with toluene diisocyanate (TDI, Sigma Aldrich) to react

the hydroxyl groups of glycerol propoxylate and the isocyanate (-N=C=O) groups of TDI (Fig. 2.1A). The remaining isocyanate groups in TDI were reacted with the hydroxyl groups of 2-hydroxyethyl methacrylate (2-HEMA, n∼34, Sigma Aldrich) and polyethylene glycol (PEG, MW = 1500, Sigma Aldrich). The final product, urethane acrylate nonionomer, consisted of a 1:3:2:1 molar ratio of glycerol propoxylate:TDI:HEMA:PEG. 50 mg of the UAN monomers were then cross-linked by the reaction between the vinyl groups (-CH=CH2) of HEMA. This polymerization was accomplished by 2 mg of azobisisobutyronitrile (AIBN, Sigma Aldrich), which creates free radical initiators when heated. The cross-linking step was carried out in 10 ml of dimethyl sulfoxide (DMSO, Sigma Aldrich) at 65°C overnight with vigorous stirring (Fig. 1B). The average molecular weight of the synthesized UAN chains was 6,700 (MALDI Micro MX, Waters) with a polydispersity of 2.0 measured via ambient temperature gel permeation chromatography (GPC, Waters). To create the NTA moiety on the hydroxyl end of the PEG groups in polymerized UAN, 10 mg of Nα,Nα-Bis(carboxymethyl)-L-lysine hydrate (NTA analog, Sigma Aldrich) in 0.1 ml DMSO was mixed with 6.4 mg of TDI (molar ratio of NTA to TDI is 1:1) for 2.5 hours at room temperature to prepare NCO-terminated NTA-TDI complexes. Then NTA-TDI was mixed with 50 mg of cross-linked UAN overnight at room temperature to covalently link NCO of NTA-TDI to OH groups of UAN chains. In order to form nanoparticles from these monomers, the UAN chains dissolved in DMSO were diluted in distilled water (dH2O) at a volume ratio of 1:10 (DMSO:dH2O). The payloads such as FITC, camptothecin, and celastrol were added to UAN chains in DMSO at 0-20% of UAN weight prior to dilution with water.

Dynamic light scattering (DLS, Malvern Instruments) was used to measure the average size of the UAN nanoparticles after synthesis, after NTA conjugation, and after payload

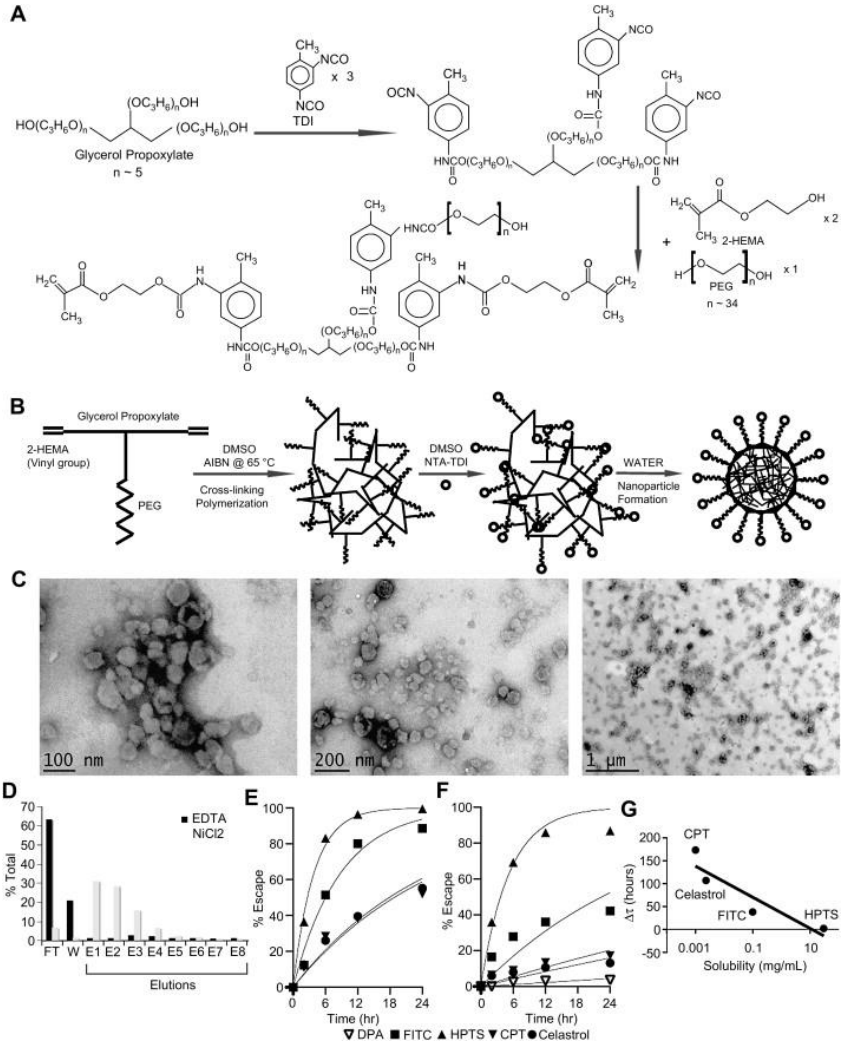

Figure 2.1: Synthesis and characterization of UAN.
(A) UAN monomer is synthesized by covalently linking 2-HEMA, PEG, and glycerol propoxylate at 2:1:1 M ratio. (B) NTA-UAN is formed by cross-linking UAN monomers with AIBN and conjugation of NTA to PEG. NTA-UAN forms nanoparticles when suspended in aqueous solution. (C) TEM images of UAN nanoparticles after staining with uranyl acetate. Scale bar is shown. (D) The function and specificity of Ni-NTA on UAN nanoparticles were confirmed by their binding to a His-peptide column. (E–F) The release kinetics of hydrophobic dyes and drugs from UAN were inferred by measuring the rate of escape through dialysis tubes without (E) or with (F) UAN. The fit of the first-order kinetics to the data is shown as a line. (G) The delay in the rate of escape ($\tau_{UAN}-\tau$) of the payloads (HPTS, FITC, celastrol, CPT) is plotted against their respective solubility values in water on a semi-log plot.

encapsulation. Transmission electron microscopy (TEM; FEI Tecnai™) images of the UAN particles were taken after staining with 1% uranyl acetate. 5 µl of the sample was placed on a glow-discharge grid for two minutes, after which excess solution was removed with filter paper. 5 µl of 1% uranyl acetate was then placed on the grid for one minute and removed with filter paper. Images were taken after air-drying the grid for 30 minutes.

His-peptide column and Ni-NTA functionality test

His-peptide column was made by covalently attaching 2 mg of His-tag peptide (NH2-Cys-Gly4-Trp-Ser-His6-COOH; subscripts denote the number of repeats) to 1 ml of aldehyde-activated agarose resin (AminoLink Coupling Resin and Kit, Pierce). The Schiff base formed between the amine and aldehyde groups was then reduced by cyanoborohydride according to the manufacturer's protocol.

'Escape' Kinetics Assay

The release kinetics of the payloads encapsulated in UAN were indirectly measured using dialysis tubes. A highly water-soluble dye, 8-Hydroxypyrene-1,3,6-trisulfonic acid trisodium salt (HPTS, Anaspec) was used as a comparison with hydrophobic agents such as FITC (Pierce), celastrol (Cayman Chemical), and camptothecin (MP Biomedicals) to demonstrate UAN's ability to delay the 'escape' or the rate of diffusion of hydrophobic molecules through dialysis tubes. 1 ml of each UAN(payload) sample was placed in separate dialysis tubes (MWCO 7,000 Da, Fisher) and subsequently placed in separate 2 liter water-baths with stirring. After overnight dialysis, the concentrations of the payloads encapsulated within UAN were measured

and the samples were subsequently placed in separate fresh dialysis tubes. 2 µl of each of the samples was taken out from the dialysis tubes and the absorbance levels were measured at different time points using a spectrophotometer (Nanodrop™ 2000) set at appropriate wave-lengths (HPTS: λmax = 454 nm, FITC: λmax = 495 nm, celastrol: λmax = 424 nm, camptothecin: λmax = 365 nm). Since DPA (Sigma Aldrich) was completely water-insoluble, DPA precipitated out of solution did not diffuse through the dialysis membrane. Therefore, UAN(DPA) was placed in a 1.7 ml microcentrifuge tube, and the supernatant after removing the DPA pellet that was released from UAN was measured for absorbance (λmax = 413 nm). The extinction coefficient and water solubility of each of the molecules are as follows: HPTS: 20,800 $M^{-1}cm^{-1}$ and highly water soluble, FITC: 70,000 $M^{-1}cm^{-1}$ and 100 µg/ml, celastrol: 10,063 $M^{-1}cm^{-1}$ and 2.33 µg/ml, camptothecin: 42,282 $M^{-1}cm^{-1}$ and 1 µg/ml, and DPA: 14,000 $M^{-1}cm^{-1}$ and water-insoluble. The same procedure was carried out to evaluate the escape kinetics of free materials with the initial concentrations of the payloads set to be equal to those encapsulated in UAN. The percent escape was plotted as 100% $[C_0\text{-}C(t)]/C_0$, where C(t) and C_0 refer to the measured payload concentration inside the dialysis tube at time = t and at time = 0 h, respectively. The rate of escape from dialysis tubes (τ) was then calculated by assuming the first order diffusion model, $C(t) = C_0 \exp(-t/\tau)$ and curve-fitting the resulting equation, $100\% [1- \exp(-t/\tau)]$, to the percent escape data.

Production of I domains, protein A, and R6.5 antibody

LFA-1 I domains and immunoglobulin G-binding recombinant protein A (17 kDa fragment) with a His tag at the C-terminal were produced in *Escherichia coli BL21(DE3)*

(Invitrogen) using pET20b and pET28a vectors, respectively. To produce protein A, a 1 liter bacteria culture with OD600 of 0.4-0.5 was induced with 1 mM isopropyl-b-D-thiogalactoside (IPTG, Gold Biotechnology) for 4 hours, after which it was centrifuged (3000 rpm, 4°C, 10 minutes) to pellet the cells. The soluble fraction of protein A was extracted by sonication and was purified using a Ni-NTA column (Novagen). Elutions from the column were further purified by size exclusion in a liquid chromatography column (Akta, GE Healthcare). Recombinant LFA-1 I domains (Asn-129 to Tyr-307) were produced as described previously[38]. Briefly, after protein induction, inclusion bodies were resuspended in 10 ml of the washing buffer (50 mM Tris (pH 8.0), 23% w/v sucrose, 0.5% w/v Triton X-100, 1 mM ethylenediaminetetraacetic acid (EDTA)), sonicated, and centrifuged again to wash the inclusion body. This process was repeated three times. Then, the inclusion bodies were solubilized with 20 ml of the solubilization buffer (50 mM Tris (pH 8.0), 6 M Guanidine-HCl) for 1.5 hours at 4°C with stirring. This solution was diluted with 2 liter of refolding buffer (50 mM Tris (pH 8.0), 10% glycerol, 1 mM $MgCl_2$) and stirred slowly at 4°C overnight to initiate protein refolding. Finally, the refolded solution was concentrated down to 1-5 ml by centrifugation (Amicon 5 kDa MWCO Millipore), filtered through 0.45 µm, and purified by gel filtration chromatography. Monoclonal antibody (mAb) R6.5 was produced from hybridoma (ATCC), and purified by a Protein A column (Pierce) followed by size exclusion.

Cell culture and labeling with UAN

HeLa cells were grown in Advanced DMEM (Gibco) containing 10% fetal bovine serum (FBS) (Atlanta Biologicals) and 2mM L-glutamine (GlutaMAX™, Gibco) at 37°C in a 5% CO2

humidified incubator. HeLa cells in 96 well plates (~90 % confluency) were washed twice with 100 µl of the labeling buffer (phosphate buffer saline (PBS), pH 7.4, 5% bovine serum albumin (BSA), 5 mM $MgCl_2$) and incubated with UAN (250 µg/ml) conjugated to I domain in 100 µl of labeling buffer at room temperature for 30 minutes. UAN(payload) nanoparticles were kept in a dialysis tube (MWCO 7,000 Da, Fisher) until they were used for cell labeling, with a minimum dialysis time of 48 hours to remove unencapsulated payloads. The unbound UAN particles were aspirated out and the cells were washed three times with the labeling buffer. The cells were then washed with the culture media and kept at 37°C, while being observed at different time points. Human breast adenocarcinomas (MDA-MB-231) were cultured in αMEM containing 10% FBS and 2mM L-glutamine, human thyroid cancer cell line (KTC-1)[41] in RPMI 1640 with 10% FBS and 2mM L-glutamine, and human microvascular endothelial cell (HMEC)-1 in MCDB 131 media (Gibco) containing 10% FBS, 2mM L-glutamine, 10 ng/ml human epidermal growth factor, 1 µg/ml hydrocortisone, and 1% penicillin-streptomycin at 37°C in a 5% CO2 humidified incubator. Human acute monocytic leukemia cell line, THP-1 (ATCC), were cultured in RPMI 1640 media with 10% fetal bovine serum, and 0.05 mM 2-mercaptoethanol at 37°C in a 5% CO2 humidified incubator. In order to induce upregulation of ICAM-1, the cells were treated with 1 µg/ml of lipopolysaccharide (LPS) in the appropriate culture media for 24 hours.

Immunofluorescence Flow Cytometry

HeLa, KTC-1, MDA-MB-231, and HMEC-1 cells (~200,000 cells per labeling) were trypsinized and washed with the labeling buffer. Since THP-1 is a suspension cell line, it was centrifuged (700 rpm, 4°C) and washed with the labeling buffer. 250 µg/ml of UAN coated with I

domain and containing FITC (I domain-UAN(FITC)) in 100 µl was added to the cells. After 15 minutes of incubation, cells were washed and re-suspended in 100 µl of the labeling buffer for flow cytometry (COULTER® EPICS® XL-MCL™ Flow Cytometer, Beckman Coulter). In evaluating the expression level of ICAM-1 in different cell lines, cells were labeled with 10 µg/ml of mAb R6.5 or LB2 (Santa Cruz Biotech), washed, and subsequently labeled with goat-anti-mouse-PE secondary antibody (Santa Cruz Biotech).

Quantification of Cell Viability

To quantify the number of viable cells after drug delivery, cells were fixed with 10% formalin for 5 minutes and stained with 0.05% crystal violet (Fisher Scientific) in distilled water for 30 minutes. After washing out the dye outside of the cells, methanol was added to release the crystal violet from the cells, which was quantified by detecting the absorbance level at 540 nm.

Statistical Analysis

Data were expressed as mean ± standard deviation of at least triplicate samples. One-way ANOVA was performed on the four groups of HeLa cells, each treated with UAN(drug) conjugated to different I domain mutants (WT, F292A, F292G, F265S/F292G). The means of the number of viable cells from each of the groups were compared. Post hoc Tukey's HSD test was carried out in order to assess which groups significantly differed from others. All of the statistical analyses were performed using GraphPad Prism5 (GraphPad Software).

Results

Synthesis and characterization of targeted UAN nanoparticles

When NTA-coupled UAN (NTA-UAN) dissolved in DMSO is diluted in water, polypropylene oxide-based segments associate with each other to form micelle-like nanoparticles with hydrophobic interior. Being covalently bound to the -OH groups of hydrophilic polyethylene oxide, NTA groups are more likely to be exposed on the surface of the UAN nanoparticles (as depicted in Fig. 2.1B). Similar to the surfactant micelles, UAN chains can absorb small hydrophobic payloads within their hydrophobic core. Thus, the hydrophobic agents can be added to NTA-UAN in DMSO (FITC, celastrol, camptothecin) or in water after dilution (DPA), which would cause the agents to be encapsulated in the core of the nanoparticles through hydrophobic interactions. Dynamic light scattering was used to measure the size distribution (hydrodynamic radius) of the following formulations: bare UAN (32.6 nm ± 2.7), NTA-UAN (42.98 nm ± 4.12), and NTA-UAN after encapsulation of various hydrophobic agents (NTA-UAN(DPA): 47.72 nm ± 5.56, NTAUAN(FITC): 44.29 nm ± 2.19, NTA-UAN(camptothecin): 52.22 nm ± 5.3, NTAUAN(celastrol): 43.7 nm ± 1.82). TEM images revealed that bare UAN nanoparticles were spherical, uniformly sized, and well dispersed (Fig. 2.1C).

The presence of NTA on the surface of UAN was studied using a His-peptide column (Fig. 2.1D). NTA-UAN nanoparticles were first charged with nickel ions by incubation with 10 mM $NiCl_2$ in PBS (pH7.4) and loaded to the His-peptide column, after which the amount of flow through and samples eluted with 50 mM EDTA were determined by the absorbance levels at 280 nm. Approximately 90% of NTA-UAN nanoparticles were bound to the column, and eluted

entirely with 50 mM EDTA. On the other hand, NTA-UAN pretreated with EDTA to remove nickel ions from UAN nanoparticles did not bind to the His-peptide column, indicating the binding of NTA-UAN nanoparticles to the column was solely dependent on Ni-NTA interaction with His-peptide.

The amounts of the payloads encapsulated in 1 mg of NTA-UAN nanoparticles after overnight dialysis were 110 μg of FITC, 87.8 μg of celastrol, 4 μg of DPA, and 28.6 μg of camptothecin. To study the release kinetics of the payloads from UAN nanoparticles, we measured the rate of diffusion or the escape rate of the payloads through a dialysis membrane with the appropriate molecular weight cutoff to contain UAN nanoparticles but allow free payloads to diffuse through. We found that the time constants (τ) for the first-order escape kinetics of the payloads from dialysis tubes without UAN were in correlation with their hydrophobicity: the 95% confidence interval for τ values of HPTS, FITC, celastrol, and camptothecin were, respectively, 3.9 ± 0.7, 9.4 ± 2.6, 27.5 ± 7.0, 30.3 ± 9.9 hours (Fig. 2.1E). The rate of escape of the payloads after encapsulation into UAN (τ_UAN) was delayed in proportion to the payloads' hydrophobicity: the τ_UAN values of HPTS, FITC, celastrol, and camptothecin were, respectively, 6.1 ± 2.3, 47.7 ± 27.0, 203.7 ± 115.5, 134.4 ± 61.8 hours (Fig. 2.1F, G). The release rate of DPA from UAN was measured at 757.1 ± 417.4 hour.

Affinity Dependent Cell Labeling Assay

LFA-1 I domain exhibits multiple conformations that are linked to differential affinity to ICAM-1 (Fig. 2.2A, B). Using a directed evolution approach, we have previously isolated a number of point mutations that led to an increase in the affinity of the I domain to ICAM-1 [38].

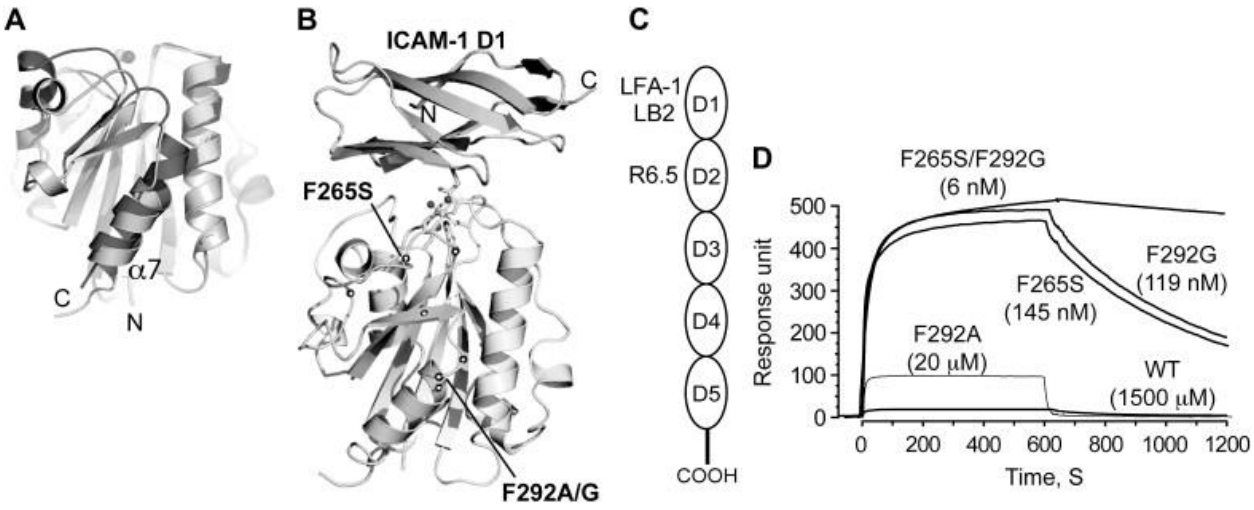

Figure 2.2: LFA-1 I domains engineered for high affinity for targeting ICAM-1.
(A) Structural diagrams of low (inactive) and high affinity (active) conformations of LFA-1 I domains. Structurally conserved regions between the two states are in light gray, while the regions that differ more than 1 Å in their Cα positions are in dark gray (inactive) and in medium gray (active). The metal ions in the metal ion-dependent adhesion site are shown as spheres. (B) The structure of the I domain in complex with ICAM-1 domain 1 (D1). Allosteric activation sites found in our previous study[38] are displayed in spheres along the peptide backbone. The metal ion and three oxygen atoms of water molecules are depicted as spheres, while the residues that coordinate to the metal ion are drawn with the sticks. (A) and (B) are adapted from Fig. 5 of Hu, X., et al[42]. (C) Schematic of ICAM-1 domains. Domain 1 binds to LFA-1 I domain. The mAbs LB2 and R6.5 bind domain 1 and domain 2, respectively. (D) Surface plasmon resonance data for binding of I domains (100 μM of WT (wild-type) and F292A and 1 μM of F265S, F292G, and F265S/F292G) to ICAM-1 immobilized (adapted from Fig. 2 of Jin et al[38]). Compared to the wild-type, each mutation of I domain (F292A, F265S, F292G, F265S/F292G) increases the binding affinity of I domain to ICAM-1 in a step-wise manner. The numbers in parentheses denote the equilibrium dissociation constants, K_D.

The equilibrium dissociation constants (*KD*) for WT, F292A, F292G, and F265S/F292G were determined, respectively, to be 1500 ± 200 μM, 20 ± 0.8 μM, 0.119 ± 0.017 μM, and 0.006 ± 0.0002 μM. (Fig. 2.2D). Compared to the more commonly used targeting approaches based on antibodies or short peptides, the I domain is a native, small (∼20 kDa), and highly specific ligand to the ICAM family molecules, and can be produced in bacteria in a large-scale. The I domain was produced with a His-tag for non-covalent conjugation to NTA-UAN nanoparticles. To estimate a maximum coating capacity of UAN, LFA-1 I domain was added in excess to UAN-NTA, after which the unbound I domain was removed by gel filtration. By the Lowry method (DC Protein Assay Kit, BioRad), the maximum capacity of UAN in binding the I domain was determined to be ∼100 μg of I domain/mg of UAN. In order to obviate the need for removing unbound proteins, the weight ratio of I domain to UAN for conjugation was used at 1:25 throughout this study. This corresponds to a molar ratio of 136:1 (I domain :UAN nanoparticle), given the molecular weight of the I domain of ∼20 kDa, the measured value of UAN density of 1 mg/ml, and the molecular weight of 68 MDa estimated for UAN with a 60 nm diameter.

To determine how the nature of different I domain mutants coating UAN would influence their interactions with ICAM-1, we examined the binding and uptake of nanoparticles by living cells. Cervical cancer cells (HeLa) were used as a model for the study, representing a group of cancer cells expressing high levels of ICAM-1. HeLa cells were labeled with I domain-UAN(FITC), washed with the culture media, and maintained at 37°C, while being observed at different time points (images were taken 2 hours after incubation) (Fig. 2.3A). The fluorescence intensity exhibited by the cells reflected LFA-1 I domain/ICAM-1 affinity dependent labeling:

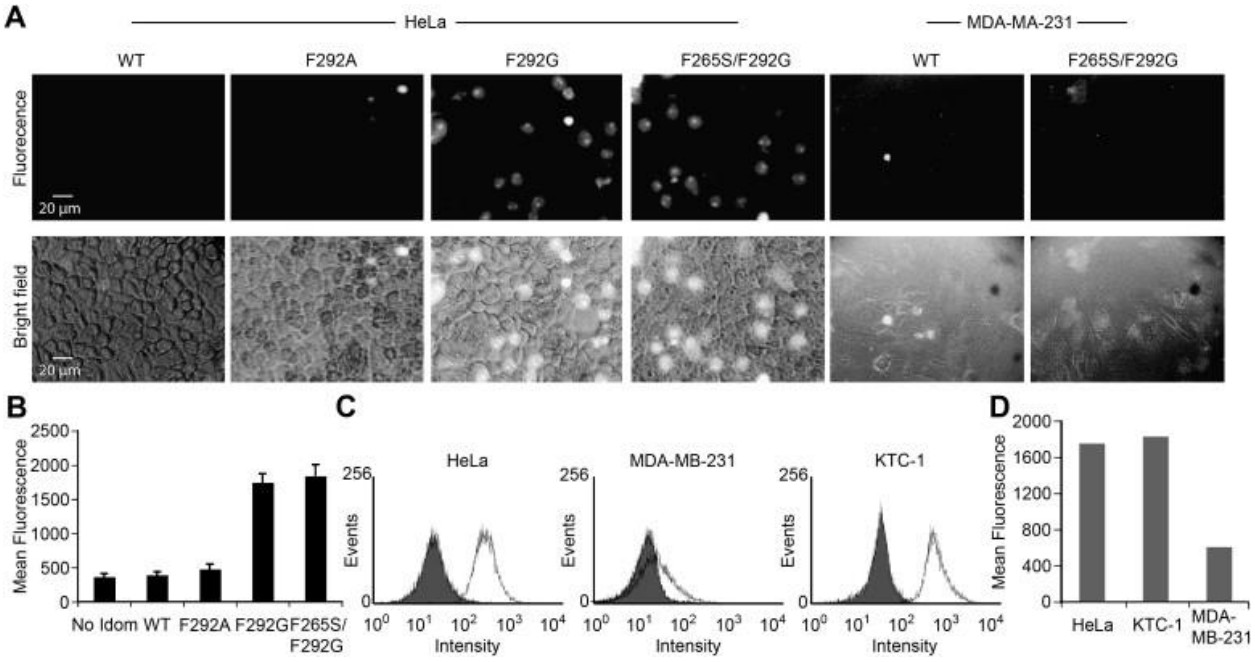

Figure 2.3: Affinity- and expression-dependent delivery of I domain-UAN(FITC) to ICAM-1 expressing cells.
(A) UAN nanoparticles encapsulating FITC and conjugated to different I domains were delivered to HeLa and MDA-MB-231 cells. (B) Immunofluorescence flow cytometry measurement of the delivery into HeLa of UAN(FITC) with no I domain, WT, or I domain variants (*n* = 3). (C) The levels of ICAM-1 expression in HeLa, MDA-MB-231, and KTC-1 cells were measured by mAb R6.5 (open histogram) or with secondary antibody alone as a control (filled histogram). (D) Immunofluorescence flow cytometry measurements of F265S/F292G-UAN(FITC) binding to HeLa, MDA-MB-231, and KTC-1 cells.

while F292A-UAN(FITC) showed only slightly higher cell labeling than the wild-type, F292G-UAN and F265S/F292G-UAN led to greatly enhanced fluorescence. The observed affinity dependent binding of UAN(FITC) was confirmed in a separate experiment, in which trypsinized HeLa cells were labeled with I domain-UAN(FITC) and the fluorescence intensity was measured by flow cytometry (Fig. 2.3B).

In order to examine if the expression level of surface antigen influences the efficiency of nanoparticle delivery, the level of I domain-UAN(FITC) binding to HeLa cells was compared to the association with other cancer cell lines, KTC-1 and MDA-MB-231, which express high and low levels of ICAM-1, respectively (Fig. 2.3C). As expected, the levels of I domain-UAN(FITC) binding to KTC-1 and MDA-MB-231 were in good correlation with the levels of ICAM-1 expression (Fig. 2.3D). The dependence of UAN targeting on the levels of antigen expression will be an important facet in achieving preferential delivery into cells over-expressing tumor-specific antigens.

Affinity Dependent Cellular Cytotoxicity Assay

We examined the cellular cytotoxicity effects of UAN nanoparticles encapsulating celastrol, a quinone methide triterpene derived from the Chinese plant *Tripterygium wilfordii*[17, 43], which is known to inhibit the function of proteasomes[43]. Celastrol has been shown to inhibit the proliferation of a variety of tumor cells, including those of leukemia, gliomas, prostate cancer[44], and melanomas[45]. After incubation with the UAN conjugated to I domains of different affinity (WT, F292A, F292G, F265S/F292G) for 30 minutes, HeLa cells were washed and maintained in culture media for 24 hours before assaying for cell viability.

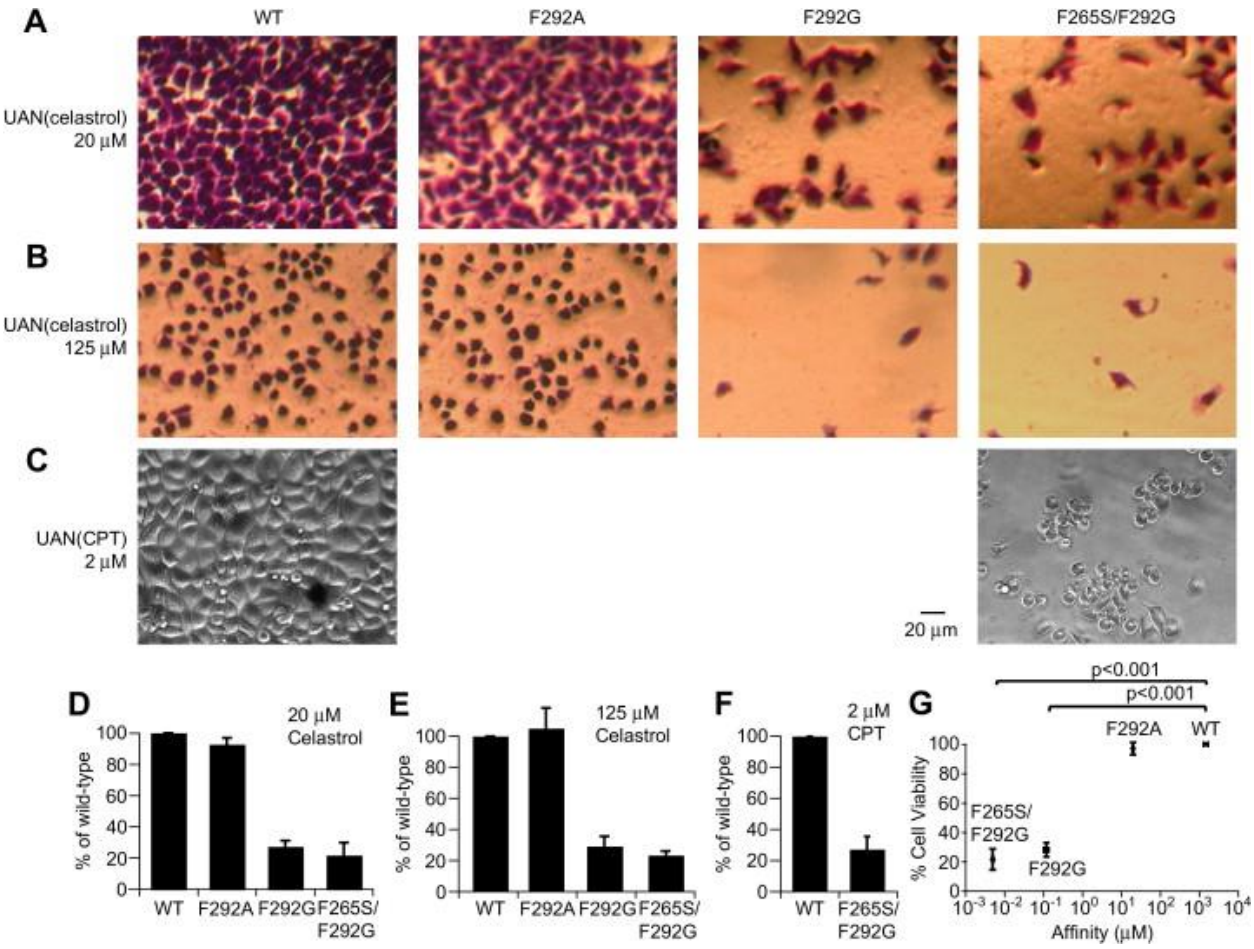

Figure 2.4: Affinity dependent cytotoxicity by I domain-UAN(celastrol or CPT).
I domain-UAN nanoparticles encapsulating celastrol (A, B) or CPT (C) were delivered to HeLa cells. The cells treated with celastrol were stained with crystal violet for better visualization. Cell viability was then quantified by measuring the amount of crystal violet after cell lysis and shown as bar graphs (D–F), normalized to the levels with WT-UAN (*n* = 3). (G) The percentage of viable cells after HeLa cells treated with UAN(celastrol or CPT) was plotted as a function of I domain affinity to ICAM-1 (*n* = 8). Values were normalized to that of the wild-type. The significance of the differences in cell viability due to I domain-UAN was analyzed by one-way ANOVA and Tukey's HSD post hoc test statistics.

UAN encapsulating high (125 μM) and low (20 μM) concentrations of celastrol caused I domain affinity dependent cytotoxicity to cells (Fig. 2.4). In the case of UAN encapsulating 20 μM celastrol, more than 80% cell death was detected with F292G-UAN and F265S/F292G-UAN, and a much lower cytotoxic effect with WT-UAN and F292AUAN (Fig. 2.4A, D). Though a similar pattern was detected with UAN encapsulating 125 μM celastrol, a significant number of cells had died and lifted off from the culture flask when targeted with WT-UAN as well (Fig. 2.4B, E). Monomeric interaction between the wild-type I domain and ICAM-1 is low (1500 ± 200 μM)[46], but the high density of I domains attached to UAN would have increased the effective affinity to ICAM-1 via multivalency or avidity effect, resulting in a sufficient amount of celastrol delivered into the cells. The discrepancy between the minimal cell labeling by WT-UAN(FITC) and the significant cell death caused by WT-UAN(celastrol) can be attributed to the higher sensitivity with which cellular cytotoxicity can be detected compared to the sensitivity of our imaging system in detecting fluorescence. To further explore the efficacy of these nanoparticles in delivering chemotherapeutic agents, we replaced celastrol with camptothecin. Camptothecin loaded at 2 μM produced cytotoxic effect comparable to celastrol loaded at 20 μM, producing a potent cell death when targeted by F265S/F292G and negligible cytotoxicity with the wild-type I domain (Fig. 2.4C, F). Cytotoxicity caused by UAN(camptothecin/celastrol) conjugated to different I domains indicated that the differences in the cell viability were in fact due to the different affinities to ICAM-1 (Fig. 2.4G; $p<0.0001$, one-way ANOVA). Cell viability due to WT-UAN vs. F292G-UAN and WT-UAN vs. F265S/F292G-UAN was also significantly different ($p<0.001$ by Tukey's HSD Post Hoc Test). The observed cell death was not due to the UAN

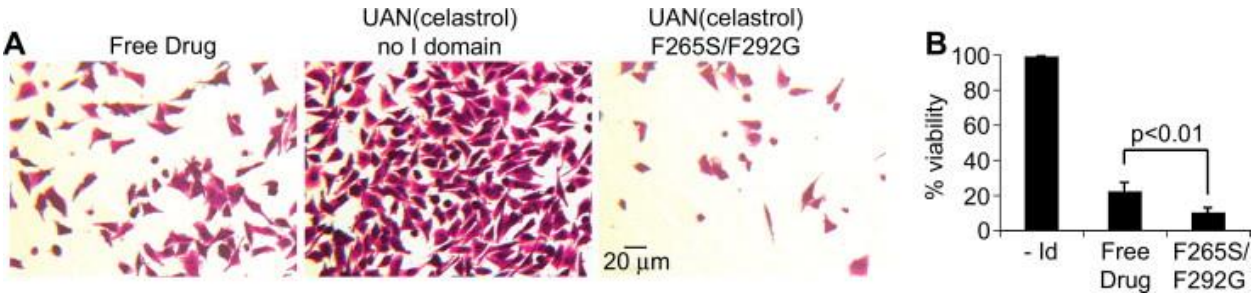

Figure 2.5: Comparison of cytotoxicity due to free celastrol, UAN(celastrol) without targeting, and F265S/F292G-UAN(celastrol).
(A) Cytotoxicity of HeLa due to the treatment with celastrol, UAN(celastrol), or F265S/F292G-UAN(celastrol) was analyzed. HeLa cells were stained with a crystal violet for better visualization (images were taken 28 h after the treatment) and subsequently lysed for quantification of cell viability. Each condition contained 100 µM of celastrol. (B) The measured cell viability was shown in bar graphs, normalized to that of 'No I domain Control' (*n* = 3).

polymer, as the F265S/F292G-UAN without drug encapsulation at up to 500 μg/ml led to negligible cytotoxic effect (data not shown).

Free celastrol vs. UAN(celastrol)

In order to demonstrate that targeted delivery of drugs carried by UAN is more potent than non-specific uptake of free drugs, we treated HeLa cells with UAN(celastrol) with no I domain, F265S/F292G-UAN(celastrol), and celastrol alone, each with 100 μM of celastrol (Fig. 2.5). After 30 minutes of incubation, cells were washed with the culture media and kept at 37°C for 28 hours. The percent cell viability was measured using the crystal violet assay. Though celastrol alone was able to cause substantial amount of cell death (78%), F265S/F292G-UAN(celastrol) induced significantly higher cytotoxicity (∼90%) (Fig. 2.5B). Notably, UAN(celastrol) without the I domain caused negligible amount of cell death, providing strong evidence that cytotoxicity induced by F265S/F292G-UAN was due to the specific uptake of UAN(celastrol) into the cells. Additionally, UAN nanoparticles were effectively precluded from non-specific uptake by the cells, and the cytotoxicity caused by celastrol diffusing out of UAN during the 30 min incubation was insignificant.

Exploiting the Versatility of UAN Nanoparticle Platform

The versatility of our nanoparticle platform comes not only from its ability to encapsulate many different naturally available hydrophobic therapeutic and contrasting agents, but also from the fact that it can be conjugated to any targeting molecules with a His-tag. To demonstrate such versatility, we used a recombinant His-tagged protein A as the linker

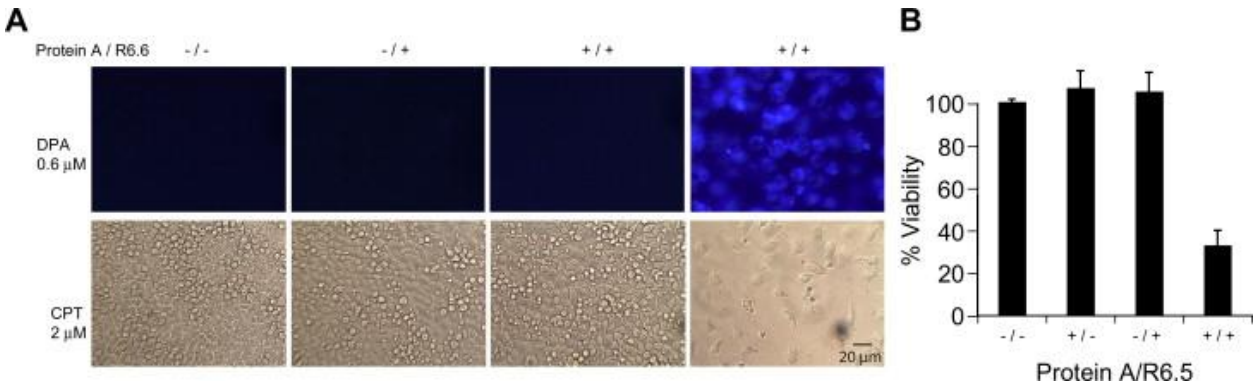

Figure 2.6: Antibody-mediated targeting of ICAM-1.
(A) In order to demonstrate the versatility of UAN platform, UAN nanoparticles were encapsulated with DPA or CPT, while the surface of UAN was coated with four different combinations of protein A and mAb R6.5. HeLa cells were imaged 2 h after incubation with UAN(DPA) and 28 h with UAN(CPT). (B) The bar graphs were normalized to that of no protein A and no R6.5 control ('–/–', *n* = 3).

between our nanoparticle and R6.5, a mAb against ICAM-1. We also encapsulated a different dye, DPA, for cell labeling, and camptothecin for cellular cytotoxicity assay (Fig. 2.6). For encapsulation of DPA, a 'soaking' method [15] of pre-formulated particles was used. DPA was dissolved in dichloromethane at 25 mg/ml and 25 µl of this DPA solution was added to UAN nanoparticles (500 µg/ml) in 10 ml water. The mixture was stirred for 24 hours to evaporate off dichloromethane, during which DPA was encapsulated into the core of UAN. Unencapsulated DPA was precipitated out of solution and removed by a 0.2 µm filter. Protein A was conjugated to NTA-UAN nanoparticle at a weight ratio of 1:25 (protein A:UAN) for 30 minutes at 4°C, which was subsequently incubated with R6.5 at a molar ratio of 1:1 (R6.5:protein A) under the same conditions. Three additional conditions were included as control samples: bare NTA-UAN particles, NTA-UAN mixed with R6.5, and NTA-UAN with protein A. These conditions showed no detectable labeling or cytotoxicity. Only with both protein A and R6.5 conjugated onto the surface of UAN nanoparticles, an efficient delivery was observed resulting in effective cell labeling and cell death. Cell viability was quantified using the crystal violet assay, which showed an approximately 80% decrease in the number of viable cells.

I domain-UAN Shows Minimal Binding to Cells Expressing Basal Levels of ICAM-1

ICAM-1 is ubiquitously present in lymphocytes, macrophages, and endothelial cells at low levels but is greatly upregulated under inflammatory conditions. To examine the possibility of UAN nanoparticle in targeting normal cells with low levels of ICAM-1, we used endothelial (HMEC-1) and monocytic (THP-1) cell lines, and measured the delivery efficiency of UAN into the cells with and without the treatment with LPS, a potent inducer of inflammation and ICAM-

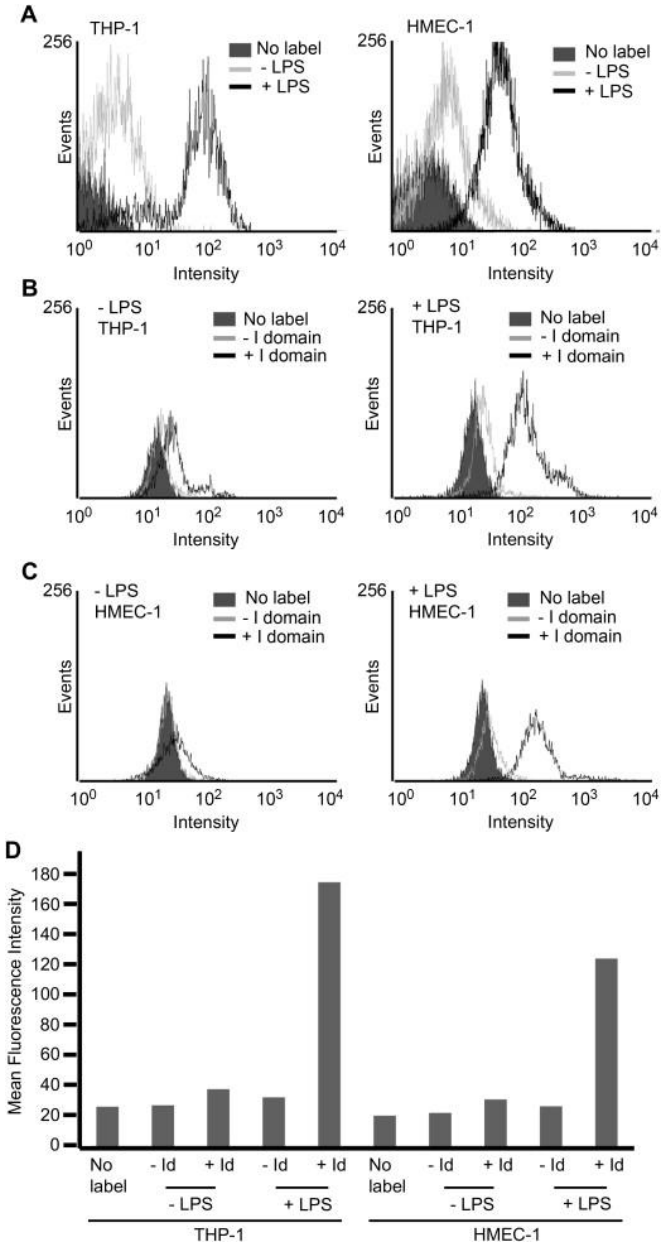

Figure 2.7: Minimal binding of I domain-UAN to cells with basal expression of ICAM-1. (A) Immunofluorescence flow cytometry measurement of mAb LB2 binding to HMEC-1 and THP-1 cells with (black open) or without (gray open) LPS treatment, or without labeling (filled histograms) to show the induction of ICAM-1 expression level. (B, C) Immunofluorescence flow cytometry measurement of F265S/F292G-UAN(FITC) (black open) binding to HMEC-1 and THP-1 cells with or without LPS treatment. UAN(FITC) without the I domain (gray open histograms) was used to measure non-specific binding to cells. Cells without labeling is shown in filled histograms. (D) Immunofluorescence flow cytometry results expressed as a bar graph.

1 expression (Fig. 2.7). The increase in ICAM-1 expression in HMEC-1 and THP-1 cells after 24 hours of LPS treatment was confirmed by immunofluorescence flow cytometry with the mAb, LB2 (Fig. 2.7A). When these cells were labeled with F265S/F292G-UAN prior to LPS induction, little binding was measured (Fig. 2.7B). However, with LPS treatment, a 4-5 fold increase in the levels of UAN binding was observed (Fig. 2.7B, C), implying a requirement for a threshold or minimum concentration of ICAM-1 on cell surface to be targeted by a sufficient dose of UAN nanoparticles to produce cytotoxic effects.

Discussion

The delivery of drugs to the target cells and tissues with minimal distribution into unwanted targets will be critical in maximizing payload concentration at the sites of interest while preventing side effects. Thus far, no molecular target has been identified that is present only in tumors. Enhancing the specificity of drug carriers by controlling the affinity and avidity of molecular interactions will, therefore, aid to minimize binding to normal cells with basal levels of the molecular target. In this study, we have demonstrated that UAN nanoparticles are highly versatile and robust in terms of the methods used for conjugation, selection of optimal surface density of targeting molecules, and encapsulation of hydrophobic imaging and therapeutic agents. Using LFA-1 I domain mutants as tools to validate our UAN platform, we demonstrated affinity dependent delivery of both therapeutic and diagnostic agents to ICAM-1 expressing HeLa cells. We have also found that the level of ICAM-1 on the surface of target cells contributed to a great degree in specific binding of UAN nanoparticles. This finding is evidenced

by the fact that despite ubiquitous expression of ICAM-1 in many different types of cells such as endothelium, epithelium, and a subset of leukocytes, our UAN nanoparticles exhibited little binding to them under resting conditions, and significant binding to endothelium and leukocytes only after induction of ICAM-1 by inflammatory molecules. ICAM-1 expression dependent delivery of UAN was also seen with two other cancer cell lines, KTC-1 and MDA-MB-231, which demonstrated a correlation between the level of UAN binding and ICAM-1 expression.

A large proportion of chemotherapeutic drugs are derived from plants[47] and contain hydrophobic aromatic groups and a chain of hydrocarbon, making them water insoluble[6]. Though much work has been done to modify these drugs to yield better analogues for solubility and bioavailability, these efforts have often resulted in drugs with reduced potency or stability[6]. Studies have shown, however, that chemotherapeutic drugs in their native forms can be encapsulated in the hydrophobic core of polymeric nanoparticles and protected from degradation, leading to an increased potency[5, 48]. The ability of UAN nanoparticles to retain hydrophobic materials was confirmed in the release kinetics study, which showed an increase in retention in correlation with their degree of hydrophobicity. Although the exact mechanism by which the payloads diffuse out of UAN after internalization into the cells is uncertain, the rate of diffusion may change once the UAN nanoparticles are exposed to a lower pH and lipid components in the endosomes.

Due to the presence of Ni-NTA, the versatility of UAN extends to its ability to be linked to any molecule with a His-tag, expanding the repertoire of targeting molecules that can be utilized. Recombinant engineering of His-tagged proteins is a common practice in molecular

biology and these proteins can be produced in a variety of expression systems. Thus, a large library of recombinant His-tagged proteins is available for immobilization onto our nanoparticles[14]. Rather than applying different surface chemistry for conjugation of different targeting molecules, Ni-NTA/His-tag interaction provides a universal and reproducible conjugation process. This non-covalent but high affinity conjugation method obviates the problems associated with the conjugation via chemical activation (e.g., carbodiimide), such as the lack of control over the degree of conjugation and orientation of the molecules, and frequent aggregation of nanoparticles and proteins. By using a ratio of proteins to nanoparticle that does not fully saturate the NTA moieties on UAN while ensuring a coating density sufficiently high for tight binding, we eliminated the purification step of removing unbound proteins from the final formulation of UAN nanoparticles. The fact that encapsulation of drugs and conjugation of targeting molecules to UAN nanoparticles do not require any chemical conjugation and special purification methods will be of significant advantage in the potential therapeutic use of UAN in clinics.

An important facet of targeted delivery of nanoparticles is the prospect of achieving specific and more potent treatment than the conventional therapy methods. Here, we have demonstrated that UAN encapsulating celastrol was much more potent than celastrol alone, which is currently being evaluated in preclinical studies for cancer therapy[45], and that UAN itself causes no toxicity. Furthermore, UAN(celastrol) without the I domain was shown to cause much less cytotoxicity, indicating that non-specific uptake of UAN nanoparticles by the cells was much lower than that of free drugs. This characteristic will be of significant importance since the administration of chemotherapeutic drugs alone lack specificity and cause significant

damage to non-cancerous tissues, leading to serious, unwanted side effects in bone marrow, gut epithelial cells, reticuloendothelial system, and hair loss. Owing to the ability to encapsulate hydrophobic materials and achieve consistent surface modification via the Ni-NTA/His-tag interaction as presented, UAN provides a promising platform for effective drug delivery in numerous disease models.

Conclusion

In this study, we have demonstrated that UAN nanoparticles possess ideal properties to achieve effective encapsulation of hydrophobic agents as well as specific delivery of imaging and cytotoxic agents to the target cells in a manner dependent on the levels of target receptor expression. The versatility of UAN nanoparticles allows for reproducible and controlled conjugation of targeting ligands via the Ni-NTA/His-tag interaction for specific targeting of diverse disease markers, while facilitating encapsulation of various hydrophobic materials in the core. Though we only demonstrated this ability using DPA, FITC, camptothecin and celastrol, the encapsulation method should be applicable to a wide array of hydrophobic materials. A drug carrier system targeting molecules over-expressed in tumor or inflammation, such as ICAM-1, can be effective in not only targeting tumors overexpressing ICAM-1 but also tumor microenvironments, which have been shown to display characteristics of inflammation sites[49-51]. Finally, the use of physiological ligands such as LFA-1 I domain used in this study may be superior to antibodies or short peptides in ensuring target specificity and preventing adverse immune responses associated with foreign antigens.

Acknowledgments

This work was supported, in whole or in part, by an American Heart Association Scientist Development Grant, NIH R01 GM090320, and Business for International Cooperative R&D between Industry, Academy, and Research Institute (Korea Small and Medium Business Administration).

REFERENCES

1. Weissleder, R., *Molecular imaging in cancer.* Science, 2006. **312**(5777): p. 1168-71.
2. Rosi, N.L., et al., *Oligonucleotide-modified gold nanoparticles for intracellular gene regulation.* Science, 2006. **312**(5776): p. 1027-30.
3. Allen, T.M. and P.R. Cullis, *Drug delivery systems: entering the mainstream.* Science, 2004. **303**(5665): p. 1818-22.
4. Mainardes, R.M. and L.P. Silva, *Drug delivery systems: past, present, and future.* Curr Drug Targets, 2004. **5**(5): p. 449-55.
5. Davis, M.E., Z.G. Chen, and D.M. Shin, *Nanoparticle therapeutics: an emerging treatment modality for cancer.* Nat Rev Drug Discov, 2008. **7**(9): p. 771-82.
6. Srivastava, V., et al., *Plant-based anticancer molecules: a chemical and biological profile of some important leads.* Bioorg Med Chem, 2005. **13**(21): p. 5892-908.
7. Ferrari, M., *Cancer nanotechnology: opportunities and challenges.* Nat Rev Cancer, 2005. **5**(3): p. 161-71.
8. Langer, R., *Drug delivery. Drugs on target.* Science, 2001. **293**(5527): p. 58-9.
9. Zentner, G.M., et al., *Biodegradable block copolymers for delivery of proteins and water-insoluble drugs.* Journal of Controlled Release, 2001. **72**(1-3): p. 203-15.
10. Farokhzad, O.C., et al., *Targeted nanoparticle-aptamer bioconjugates for cancer chemotherapy in vivo.* Proc Natl Acad Sci U S A, 2006. **103**(16): p. 6315-20.
11. Hong, S., et al., *The binding avidity of a nanoparticle-based multivalent targeted drug delivery platform.* Chem Biol, 2007. **14**(1): p. 107-15.
12. Bartlett, D.W., et al., *Impact of tumor-specific targeting on the biodistribution and efficacy of siRNA nanoparticles measured by multimodality in vivo imaging.* Proc Natl Acad Sci U S A, 2007. **104**(39): p. 15549-54.
13. Kim, J.Y., S.B. Shim, and J.K. Shim, *Effect of amphiphilic polyurethane nanoparticles on sorption-desorption of phenanthrene in aquifer material.* J Hazard Mater, 2003. **98**(1-3): p. 145-60.
14. Fischer, N.O., et al., *Immobilization of His-tagged proteins on nickel-chelating nanolipoprotein particles.* Bioconjug Chem, 2009. **20**(3): p. 460-5.
15. Zhu, H.G. and M.J. McShane, *Loading of hydrophobic materials into polymer particles: Implications for fluorescent nanosensors and drug delivery.* Abstracts of Papers of the American Chemical Society, 2005. **230**: p. U3640-U3641.
16. Hertzberg, R.P., et al., *Modification of the Hydroxy Lactone Ring of Camptothecin - Inhibition of Mammalian Topoisomerase-I and Biological-Activity.* Journal of Medicinal Chemistry, 1989. **32**(3): p. 715-720.
17. Yang, H.J., et al., *Celastrol, a triterpene extracted from the Chinese "Thunder of God Vine," is a potent proteasome inhibitor and suppresses human prostate cancer growth in nude mice.* Cancer Research, 2006. **66**(9): p. 4758-4765.
18. Park, J.W., et al., *Tumor targeting using anti-her2 immunoliposomes.* Journal of Controlled Release, 2001. **74**(1-3): p. 95-113.

19. Ishida, O., et al., *Liposomes bearing polyethyleneglycol-coupled transferrin with intracellular targeting property to the solid tumors in vivo.* Pharm Res, 2001. **18**(7): p. 1042-8.
20. Mamot, C., et al., *Epidermal growth factor receptor (EGFR)-targeted immunoliposomes mediate specific and efficient drug delivery to EGFR- and EGFRvIII-overexpressing tumor cells.* Cancer Res, 2003. **63**(12): p. 3154-61.
21. Leamon, C.P., D. Weigl, and R.W. Hendren, *Folate copolymer-mediated transfection of cultured cells.* Bioconjug Chem, 1999. **10**(6): p. 947-57.
22. Montet, X., et al., *Nanoparticle imaging of integrins on tumor cells.* Neoplasia, 2006. **8**(3): p. 214-22.
23. Peer, D. and R. Margalit, *Loading mitomycin C inside long circulating hyaluronan targeted nano-liposomes increases its antitumor activity in three mice tumor models.* Int J Cancer, 2004. **108**(5): p. 780-9.
24. Lee, C.M., et al., *Novel chondroitin sulfate-binding cationic liposomes loaded with cisplatin efficiently suppress the local growth and liver metastasis of tumor cells in vivo.* Cancer Res, 2002. **62**(15): p. 4282-8.
25. Dustin, M.L., et al., *Induction by IL 1 and interferon-gamma: tissue distribution, biochemistry, and function of a natural adherence molecule (ICAM-1).* J Immunol, 1986. **137**(1): p. 245-54.
26. Marlin, S.D. and T.A. Springer, *Purified Intercellular-Adhesion Molecule-1 (Icam-1) Is a Ligand for Lymphocyte Function-Associated Antigen-1 (Lfa-1).* Cell, 1987. **51**(5): p. 813-819.
27. Ogawa, Y., et al., *Expression of intercellular adhesion molecule-1 in invasive breast cancer reflects low growth potential, negative lymph node involvement, and good prognosis.* Clinical Cancer Research, 1998. **4**(1): p. 31-36.
28. Kelly, C.P., et al., *Human colon cancer cells express ICAM-1 in vivo and support LFA-1-dependent lymphocyte adhesion in vitro.* Am J Physiol, 1992. **263**(6 Pt 1): p. G864-70.
29. Passlick, B., et al., *Expression of major histocompatibility class I and class II antigens and intercellular adhesion molecule-1 on operable non-small cell lung carcinomas: frequency and prognostic significance.* Eur J Cancer, 1994. **30A**(3): p. 376-81.
30. Tomita, Y., et al., *Expression of intercellular adhesion molecule-1 (ICAM-1) on renal-cell cancer: possible significance in host immune responses.* Int J Cancer, 1990. **46**(6): p. 1001-6.
31. Koyama, S., T. Ebihara, and K. Fukao, *Expression of intercellular adhesion molecule 1 (ICAM-1) during the development of invasion and/or metastasis of gastric carcinoma.* J Cancer Res Clin Oncol, 1992. **118**(8): p. 609-14.
32. Shimoyama, S., et al., *Overexpression of intercellular adhesion molecule-1 (ICAM-1) in pancreatic adenocarcinoma in comparison with normal pancreas.* Pancreas, 1997. **14**(2): p. 181-6.
33. Coussens, L.M. and Z. Werb, *Inflammation and cancer.* Nature, 2002. **420**(6917): p. 860-7.
34. Matsumura, Y., et al., *Phase I and pharmacokinetic study of MCC-465, a doxorubicin (DXR) encapsulated in PEG immunoliposome, in patients with metastatic stomach cancer.* Ann Oncol, 2004. **15**(3): p. 517-25.

35. Pasqualini, R., et al., *Aminopeptidase N is a receptor for tumor-homing peptides and a target for inhibiting angiogenesis.* Cancer Research, 2000. **60**(3): p. 722-727.
36. Kurzinger, K., et al., *A Novel Lymphocyte Function-Associated Antigen (Lfa-1) - Cellular-Distribution, Quantitative Expression, and Structure.* Journal of Immunology, 1981. **127**(2): p. 596-602.
37. Yang, L., et al., *ICAM-1 regulates neutrophil adhesion and transcellular migration of TNF-alpha-activated vascular endothelium under flow.* Blood, 2005. **106**(2): p. 584-592.
38. Jin, M., et al., *Directed evolution to probe protein allostery and integrin I domains of 200,000-fold higher affinity.* Proceedings of the National Academy of Sciences of the United States of America, 2006. **103**(15): p. 5758-5763.
39. Grunert, H.P., et al., *Internalization of human rhinovirus 14 into HeLa and ICAM-1-transfected BHK cells.* Medical Microbiology and Immunology, 1997. **186**(1): p. 1-9.
40. Kim, J.Y., et al., *Synthesis of CdS nanoparticles dispersed within poly(urethane acrylate-co-styrene) films using an amphiphilic urethane acrylate nonionomer.* Macromolecular Chemistry and Physics, 2006. **207**(11): p. 925-932.
41. Kurebayashi, J., et al., *Additive antitumor effects of gefitinib and imatinib on anaplastic thyroid cancer cells.* Cancer Chemotherapy and Pharmacology, 2006. **58**(4): p. 460-470.
42. Hu, X., et al., *Yeast surface two-hybrid for quantitative in vivo detection of protein-protein interactions via the secretory pathway.* Journal of Biological Chemistry, 2009. **284**(24): p. 16369-76.
43. Mu, T.W., et al., *Chemical and biological approaches synergize to ameliorate protein-folding diseases.* Cell, 2008. **134**(5): p. 769-781.
44. Sethi, G., et al., *Celastrol, a novel triterpene, potentiates TNF-induced apoptosis and suppresses invasion of tumor cells by inhibiting NF-kappa B-regulated gene products and TAK1-mediated NF-kappa B activation.* Blood, 2007. **109**(7): p. 2727-2735.
45. Abbas, S., et al., *Preclinical studies of celastrol and acetyl isogambogic acid in melanoma.* Clin Cancer Res, 2007. **13**(22 Pt 1): p. 6769-78.
46. Shimaoka, M., et al., *Structures of the alpha L I domain and its complex with ICAM-1 reveal a shape-shifting pathway for integrin regulation.* Cell, 2003. **112**(1): p. 99-111.
47. Balunas, M.J. and A.D. Kinghorn, *Drug discovery from medicinal plants.* Life Sciences, 2005. **78**(5): p. 431-441.
48. Kawano, K., et al., *Enhanced antitumor effect of camptothecin loaded in long-circulating polymeric micelles.* Journal of Controlled Release, 2006. **112**(3): p. 329-332.
49. Nakashima, Y., et al., *Upregulation of VCAM-1 and ICAM-1 at atherosclerosis-prone sites on the endothelium in the ApoE-deficient mouse.* Arteriosclerosis Thrombosis and Vascular Biology, 1998. **18**(5): p. 842-851.
50. Davies, M.E., H. Sharma, and R. Pigott, *ICAM-1 expression on chondrocytes in rheumatoid arthritis: induction by synovial cytokines.* Mediators Inflamm, 1992. **1**(1): p. 71-4.
51. Hofer, S., et al., *Injury of the blood brain barrier and up-regulation of icam-1 in polymicrobial sepsis.* J Surg Res, 2008. **146**(2): p. 276-81.

CHAPTER 3

Tumor suppression via paclitaxel-loaded drug carriers that target inflammation marker upregulated in tumor vasculature and macrophages

This chapter was originally published in Biomaterials (Park, S., Kang, S., Chen, X., Kim, E.J., Kim, J., Kim, N., Kim, J.Y., Jin, M.M. *Biomaterials*. 2013;34(2):598-605. ©2013 Elsevier.), and is reprinted with permission. The following is the detailed contribution of authors: S.P., M.M.J., and K.J.Y. designed research, performed research, and wrote the paper; S.K., X.C., E.J.K., J.K., and N.K. performed research.

Summary

Clinically approved chemotherapeutic nanoparticles may provide advantages over free drugs by achieving slower clearance and preferential accumulation in tumors. However, the lack of leaky vasculatures can create barriers to the permeation of ~100 nm-sized nanoparticles in solid tumors. We hypothesized that nanoparticles designed to target both tumor and tumor stroma would penetrate deeper into the tumors. To construct such comprehensive drug carriers, we utilized cross-linked amphiphilic polymer nanoparticles and functionalized them to target ICAM-1, a biomarker prevalent in various tumors and inflamed tumor stroma. The targeting moiety was derived from the modular domain present in α_L integrin, which was engineered for high affinity and cross-reactivity with human and murine ICAM-1. ICAM-1-selective delivery of paclitaxel produced potent tumor suppression of not only ICAM-1-positive cervical cancer cells but also ICAM-1-negative tumors, presumably by causing cytotoxicity in tumor-associated endothelium ($CD31^+$) and macrophages ($CD68^+$) over-expressing ICAM-1.

Contrary to the strategies of targeting only the tumor or specific tumor stromal constituents, we present a strategy in delivering therapeutics to the major cellular components of solid tumors. Drug carriers against inflammation-biomarkers may be effective against many different types of tumors, while being less susceptible to the highly mutable nature of tumor markers.

Introduction

Achieving site-specific delivery of drug carriers, while minimizing unwanted distribution, has been one of the pursued goals in cancer therapy. Current drug carriers of ~100 nm in size can be selectively delivered into tumors through the enhanced permeability and retention (EPR) effect[1]. Several different nanoparticles employing the EPR effect have been approved for clinical use, e.g., Doxil and Abraxane. Tumor killing by non-molecularly targeted carriers may be accomplished via slow release of drugs within the tumor interstitial space or from the release of drugs inside cells after non-specific uptake[2]. However, current drug delivery systems fall short on achieving adequate concentrations of drugs in tumor cells in hypoxic regions as well as in malignancies that lack leaky vasculature, promoting the development of drug-resistance[3].

Much of the limitations of non-targeted nanoparticle-based drug carriers come from the fact that (i) leaky pores in tumor vessels are often sparsely distributed and some tumors completely lack well-perfused vasculatures, leading to heterogeneous or limited dissemination of nanoparticles[1, 4], (ii) increased interstitial pressure within tumors tends to rapidly clear nanoparticles distributed outside of cells, and (iii) surface modifications of drug carriers to

reduce non-specific uptake by phagocytic cells and opsonization also disfavor the uptake of nanoparticles by tumors[2, 5, 6].

To overcome such physiological barriers, local applications of hyperthermia[7], photosensitization[8], and ultrasound[9] have been used to increase the permeability of tumor vessels and thus, the penetration of drug carriers throughout the tumor. Alternatively, new types of nanoparticles to address the aforementioned problems have also been engineered. For example, drug carriers possessing the ability to target tumor stromal constituents, including the vasculature[10, 11] and/or tumor-associated macrophages[12], have shown promising results. Similarly, we have previously found that a molecule called intercellular adhesion molecule (ICAM)-1 was highly induced in endothelial cells within and in the vicinity of tumors[13]. ICAM-1 is a cell adhesion molecule normally expressed at low levels in a variety of cell types but over-expressed in inflammation and neoplastic conditions, likely due to the activation of the transcriptional factor, NF-κB. ICAM-1 is upregulated in many carcinomas including breast, colon, non-small cell lung, and gastric tumors[14-19], where the overexpression of ICAM-1 is correlated with tumor progression, metastatic capability, and poor prognosis[20-22]. Upregulation of ICAM-1 within the tumor stroma is, therefore, consistent with the increasing reports on the implication of inflammation in tumor initiation, progression, and metastasis[23, 24]. More importantly, it can be speculated that drug carriers designed to target ICAM-1 would be broadly effective in eradicating not only carcinoma cells expressing ICAM-1 but also those lacking ICAM-1 by killing the tumor stromal cells that are critical to tumor growth and metastasis. The delivery of drugs against multi-cellular components comprising tumors may also be less susceptible to the development of drug-resistance.

In order to create ICAM-1-specific drug carriers, we used a modular domain called the inserted (I) domain derived from the integrin, leukocyte function associated antigen-1 (LFA-1; also known as αLβ2 or CD11a/CD18), where the I domain is the only region that provides molecular contact with ICAM-1. The I domain in its native sequence, separated from LFA-1, exhibits a low level of binding to ICAM-1, and was therefore engineered for high affinity and cross-reactivity with human and murine ICAM-1[25-27]. LFA-1 I domain's reaction with murine ICAM-1 is an important property that permits selectivity studies of drug carriers against both the ICAM-1-expressing human tumors and the inflamed murine tumor microenvironment in mouse models of human cancer. At the same time, this feature enables us to analyze the unintended delivery to the low, yet widespread, expression of ICAM-1 in many different cellular types. As a drug carrier, we employed nanoparticles synthesized with cross-linked amphiphilic copolymer, providing a hydrophobic core for encapsulation of hydrophobic molecules and hydrophilic corona for stability in vivo as well as facile conjugation with targeting moieties[28]. Drug carriers designed to target markers prevalent in carcinomas and inflamed tumor microenvironment may prove effective against many different types of cancers.

Experimental Procedures

Production of high-affinity LFA-1 I domain

Recombinant LFA-1 I domain with a His-tag at the N-terminal was produced in BL21(DE3) *Escherichia coli* cells (Invitrogen) as described previously[26]. Briefly, after protein induction with 1 mM IPTG (isopropyl-β-D-thiogalactoside), *E. coli* cells were resuspended in 10

ml of the washing buffer (50 mM Tris (pH 8.0), 23% w/v sucrose, 0.5% w/v Triton X-100, 1 mM ethylenediaminetetraacetic acid (EDTA)), sonicated, and centrifuged again to purify the inclusion body. The inclusion bodies were solubilized with 20 ml of the solubilization buffer (50 mM Tris (pH 8.0), 6 M Guanidine-HCl) for 1.5 h at 4°C with stirring, after which the solution was diluted with 2 l of refolding buffer (50 mM Tris (pH 8.0), 10% glycerol, 1 mM $MgCl_2$) and stirred slowly at 4°C overnight for the refolding process. Finally, the protein was concentrated down to 1-5 ml (Amicon 3 kDa MWCO Millipore), filtered through a 0.45 mm filter (Nalgene), and purified by gel filtration chromatography (Superdex-75, GE Healthcare Life Sciences ÄKTApurifier™).

Preparation of I domain-coated urethane acrylate nonionomer (UAN) nanoplatforms

The synthesis of cross-linked UAN bound to nickel-nitriloacetic acid (NTA-UAN) was previously described[29]. In brief, UAN consists of 1:3:2:1 molar ratio of glycerol propoxylate:toluene diisocyanate:2-hydroxyethyl methacrylate (HEMA):-polyethylene glycol (PEG). 50 mg of the UAN monomers were cross-linked by the reaction between the vinyl groups of HEMA in 10 ml of dimethyl sulfoxide (DMSO, Sigma Aldrich) at 65°C overnight with vigorous stirring, catalyzed by 2 mg of azobisisobutyronitrile (AIBN, Sigma Aldrich). The average molecular weight of the resulting UAN chains was 6700 Da (measured by mass spectrometer (MALDI Micro MX, Waters)) with a polydispersity of 2.0 (measured via ambient temperature gel permeation chromatography (GPC, Waters)). To incorporate the NTA moiety on the hydroxyl end of the PEG groups in polymerized UAN, 10 mg of Nα,Nα-Bis(carboxymethyl)-L-lysine hydrate (NTA analog, Sigma Aldrich) in 0.1 ml DMSO was mixed with 6.4 mg of TDI (molar ratio

of NTA to TDI was 1:1) for 2.5 h at room temperature to prepare NCO-terminated NTA-TDI complexes. Then the NTA-TDI solution was added to 5 ml of DMSO containing 50 mg of cross-linked UAN and mixed overnight at room temperature to covalently link NCO of NTA-TDI to OH groups of UAN chains. In order to form nanoparticles, the cross-linked UAN chains dissolved in DMSO were diluted in HEPES buffer saline (HBS) at a volume ratio of 1:100 (DMSO:HBS).

Previously, the size distribution (hydrodynamic radius) of NTA-UAN formulations encapsulating various hydrophobic agents was determined to be ~45-60 nm using dynamic light scattering (Malvern Instruments)[29]. In addition, transmission electron microscopy images revealed that bare UAN nanoparticles were spherical, uniformly sized, and well dispersed[29]. The payloads such as DiO (Invitrogen), DiR (Invitrogen), and Paclitaxel (PTX) (Sigma) were added to UAN chains in DMSO at 0-20% of UAN weight prior to dilution with HBS. The NTA moiety of UAN was charged with 10 mM $NiCl_2$ for 30 min at RT. Excess payloads, $NiCl_2$, and DMSO were removed via dialysis and subsequent concentration of the solution down to appropriate volume. Ni-NTA-UAN was then incubated with I domain at a weight ratio of 25:1 (Ni-NTA-UAN:I domain) at 4°C for 30 min to form I domain-coated cross-linked UAN (Id-UAN) before being used in subsequent experiments.

EC_{50} analyses

HeLa cells cultured in a 24-well plate were treated with 300 ml of the labeling buffer (pH 7.4 PBS, 1% (w/v) BSA, 1 mM $MgCl_2$) containing varying concentrations of UAN(PTX) (non-targeted cross-linked UAN carrying PTX), Id-UAN(PTX) (I domain-bound UAN(PTX)), or PTX. The amount of PTX ranged from 0.1% to 17% of UAN (w/w). Ten minutes after the treatment, cells

were washed twice with the labeling buffer and resuspended in 300 ml of the culture media without FBS for 72 h. Cell viability was then measured by directly counting cells on a hemocytometer. Cells labeled with trypan blue were excluded in cell counting.

Developing subcutaneous lipopolysaccharde (LPS) mouse model

100 ml of LPS (1 mg/ml in PBS) and PBS were bilaterally injected into the lower flanks of 7-week-old female severe combined immunodeficiency (SCID) mice. All animal experiments were conducted in compliance with the regulations defined by the Institutional Laboratory Animal Use and Care Committee of Cornell University.

Developing subcutaneous tumor xenograft mouse model

$3x10^6$ human cervical cancer HeLa cells and human embryonic kidney 293T cells mixed with Matrigel (BD) in equal volume (150 ml each) were injected bilaterally into front lower flank areas of 7-week-old female SCID mice. Once the tumor size reached approximately 100 mm^3 (7-10 days), mice were used for subsequent treatments.

Near-IR optical imaging of mice

Ex vivo imaging was performed 18-24 h after retro-orbital injection of UAN(DiR) or Id-UAN(DiR) using an NIR camera (Luca, Andor Technology). Each injection consisted of 200 mg of UAN. Image analysis was performed using Matlab R2007a (MathWorks) and ImageJ (NIH).

Tumor cytotoxicity assay

Mice were randomized into three groups (n = 10 each) for the following treatments given every 3 days for a total of three interventions: retro-orbital intravenous (i.v.) injection of HBS as a control, i.v. injection of 200 mg (UAN weight) of UAN(PTX), or i.v. injection of 200 mg (UAN weight) of Id-UAN(PTX). Tumor size was measured daily, while the blood collection from tail-vein (~200 μl) and body weight measurement for the toxicity assays were carried out on the days of injection.

Liver toxicity assay

Blood samples from tail-vein collected in capillary tubes were snap-frozen in liquid nitrogen and kept at -80°C until being analyzed for the activity levels of aspartate transaminase (AST) and alanine transaminase (ALT) according to the manufacturer's protocol (BioVision).

Flow cytometry and immunofluorescence analysis of ex vivo tissues

Tissues from tumors and other organs were collected from tumor bearing mice with or without in vivo injections of Id-UAN(DiO) or UAN(DiO). Harvested tissues were diced and digested with collagenase A (1 mg/ml) for 8 h before being strained. Collected cells were washed once with labeling buffer and incubated for 30 min using rat anti-mouse CD31 monoclonal antibody (mAb) (MEC13.3, BD), rat anti-mouse CD68 mAb (FA-11, BioLegend), rabbit anti-murine ICAM-1 polyclonal antibody (M-19, SantaCruz), rabbit anti-human ICAM-1 mAb (LB-2, SantaCruz). After labeling with primary antibodies, cells were washed with labeling buffer and incubated with anti-rat or anti-rabbit phycoerythrin (PE)-labeled secondary antibodies (Invitrogen). Subsequently, flow cytometry experiment was carried out to measure

the fluorescence intensity of DiO as well as the antibodies (Beckman Coulter EPICS XL-MC). The data were analyzed using FlowJo (Tree Star).

Statistical analysis

Data were expressed as mean ± standard deviation of at least triplicate samples. Two-way ANOVA and Bonferroni post hoc test were carried out in order to assess which groups significantly differed from others. All of the statistical analyses were performed using GraphPad Prism 5 (Graphpad Software).

Results

Biodistribution, selectivity, and toxicity of drug carriers

Prior to testing the efficacy of ICAM-1-specific nanoparticles in eradicating tumors, we first evaluated their biodistribution, selectivity to ICAM-1, and toxicity with or without surface conjugation with I domain. The engineered I domain we utilized in this study contains F265S/F292G mutations and binds human and murine ICAM-1 with high affinity (2 nM K_D)[30]. Cross-linked UAN nanoparticles contain a core formed by polypropylene oxide networks, which can retain hydrophobic molecules at up to 20% w/w of UAN, and exhibit slower release kinetics with increasing hydrophobicity of payloads[29]. Almost irreversible retention of water-insoluble near-infrared dye, DiR, by cross-linked UAN suspended in an aqueous solution was exemplified by negligible partitioning of DiR into chloroform, while free DiR was almost entirely dissolved in chloroform (Fig. 3.1A).

Biodistribution of UAN(DiR) or Id-UAN(DiR) into the major organs and the sites of interest was quantified by near-infrared imaging of organs *ex vivo*. Two different mouse models were chosen to examine the difference in biodistribution caused by the presence of I domain on UAN: (1) untreated mice to assess the targeting of basal expression of ICAM-1 and (2) mice with subcutaneous injection of lipopolysaccharide (LPS) to examine the ability of Id-UAN to localize to the site of ICAM-1 over-expression. Major organs and the subcutaneous treatment sites were harvested 18 h post-injection of UAN particles for biodistribution analysis. In untreated mice, irrespective of the conjugation with I domain, liver and spleen accounted for 66% of UAN nanoparticles that accumulated into major organs (Fig. 3.1B). Although at much lower levels, Id-UAN(DiR) showed a higher level of accumulation than UAN(DiR) in lungs and kidneys. Next, using a mouse model with subcutaneous bilateral injections of LPS and PBS (12 h), we examined the influence of localized induction of ICAM-1 on nanoparticle distribution (Fig. 3.1C). Notably, the presence of I domain on the surface of UAN caused a 3-fold higher concentration at the LPS injection site compared to the PBS injection site. In contrast to Id-UAN(DiR), UAN(DiR) accumulated significantly less into both LPS and PBS sites, displaying insignificant difference between the two regions. Although the overall pattern of biodistribution into the major organs in LPS mouse model was comparable to that of the untreated mice, the higher level of uptake was observed in the liver and spleen, likely caused by the LPS seeping into circulation and triggering a mild systemic inflammation. This would then enhance the phagocytic activity of immune cells and dilate the vessels, resulting in elevated accumulation into some of the major organs.

The high accumulation of the particles in the liver, however, raised a concern for possible systemic side effects. We carried out a liver toxicity assay by measuring the serum activity levels of aspartate transaminase (AST) and alanine transaminase (ALT), two enzymes that often serve as markers for liver damage (Fig. 3.1D). AST and ALT levels measured between 0 and 48 h after LPS injection, used to artificially induce liver toxicity were gradually elevated, peaking at 24 h and dropping back to normal levels by 48 h. In contrast, ALT/AST levels after UAN(DiR) injection remained below the threshold for liver toxicity, and did not differ greatly from mice treated with PBS.

Tumor targeting: tissue- and cell-level distribution analysis

To confirm the selectivity of UAN conferred by the I domains toward ICAM-1 over-expressed in tumors or in inflamed tumor stroma, we used a mouse model harboring bilateral subcutaneous xenografts of ICAM-1-positive HeLa and ICAM-1-negative 293T tumors. When tumors grew to ~100 mm^3 in size, mice were intravenously injected with UAN nanoparticles and imaged at 24 h post-injection. Id-UAN(DiR) was found at both tumor sites, whose fluorescence levels were significantly higher than those in the tumors injected with UAN(DiR) (5.1-fold in HeLa and 2.1-fold in 293T tumor) (Fig. 3.2A). Furthermore, 2.9-fold increase in accumulation into HeLa over 293T was observed with Id-UAN(DiR), while comparable amounts were found in both tumors with UAN(DiR).

We then examined if increased delivery of Id-UAN(DiR) into 293T tumor was from targeting of ICAM-1 induced in tumor stromal cells, such as vasculature endothelium and/or tumor-associated macrophages. To first confirm if 293T cells have induced ICAM-1 in the course

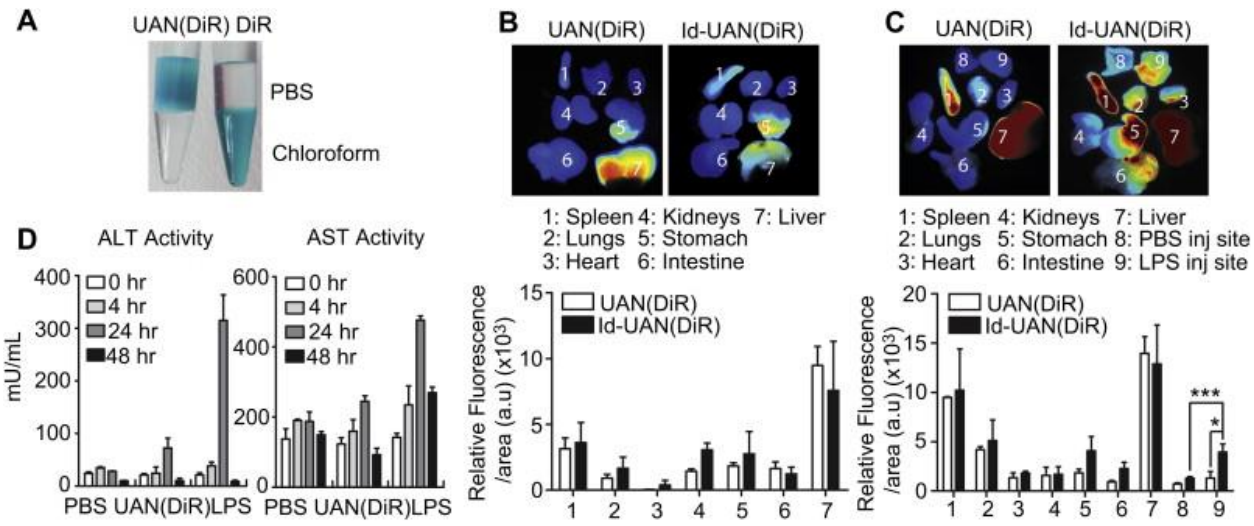

Figure 3.1: Biodistribution, selectivity, and toxicity of drug carriers.
(A) Partitioning of DiR from chloroform into the hydrophobic core of UAN dispersed in PBS. 0.05 mg of DiR was dissolved in 0.05 ml of DMSO or DMSO containing cross-linked UAN (1 mg) before being added to a liquid bilayer of PBS/chloroform (0.5 ml each) and shaken gently for 4 h. (B) NIR imaging and quantification of UAN(DiR) and Id-UAN(DiR) dispersed throughout the major organs after intravenous injection at 24 h post-injection (n = 6; a.u. = arbitrary unit). (C) UAN(DiR) and Id-UAN(DiR) distribution at 24 h post-injection in LPS mouse model. Nanoparticles were injected 12 h after subcutaneous LPS/PBS injection (n = 4). (D) Liver toxicity of UAN(DiR) compared to LPS and PBS. Bar graphs represent serum activity levels of ALT and AST (n = 6) (Error bars are standard deviations (SD) *$p < 0.05$, ***$p < 0.001$; Two-way ANOVA test followed by Bonferroni post hoc test).

of tumor growth, we carried out immunofluorescence flow cytometry on the cells isolated from untreated HeLa and 293T tumors (Fig. 3.2B). From labeling of cells with antibodies against human or murine ICAM-1 (CD54), we found only murine ICAM-1 was induced in 293T tumors while both human and murine ICAM-1 were present in HeLa tumors, proving the lack of ICAM-1 expression in 293T cells and upregulation of ICAM-1 in tumor stromal cells. Next, to test if $CD31^+$ and $CD68^+$ cells were the cellular types responsible for the presence of ICAM-1 in tumor stroma, we labeled the cells isolated from tumors with antibodies against ICAM-1 along with antibodies against either CD31 or CD68. Indeed, significantly higher percentage of tumor-associated $CD31^+$ and $CD68^+$ cells exhibited over-expression of ICAM-1, while corresponding cellular types derived from skin and spleen were mostly negative for ICAM-1 expression (CD31/CD68 from skin; CD31 from spleen) or induced at lower levels (CD68 from spleen) (Fig. 3.2C and D).

Tumor-targeting nanoparticles that have escaped from circulation through leaky vasculature would diffuse through the tumor interstitial space. Subsequent uptake of these particles is influenced by the intrinsic properties of particles (i.e., size, charge, shape) and the presence of active molecular targeting moieties. Therefore, some of the signals coming from the tumors and organs may be due to the particles being merely trapped in the extracellular or interstitial space. Since UAN nanoparticles are designed to deliver drugs directly into cells for effective cytotoxicity rather than through slow release within extracellular space, we carried out flow cytometry to quantify cellular uptake of UAN particles loaded with a hydrophobic green fluorescent dye, DiO (Fig. 3.2E). Similar to the tissue-level analysis, Id-UAN(DiO) was taken up by higher percentages of cells harvested from both tumors, with DiO^+ cells in HeLa

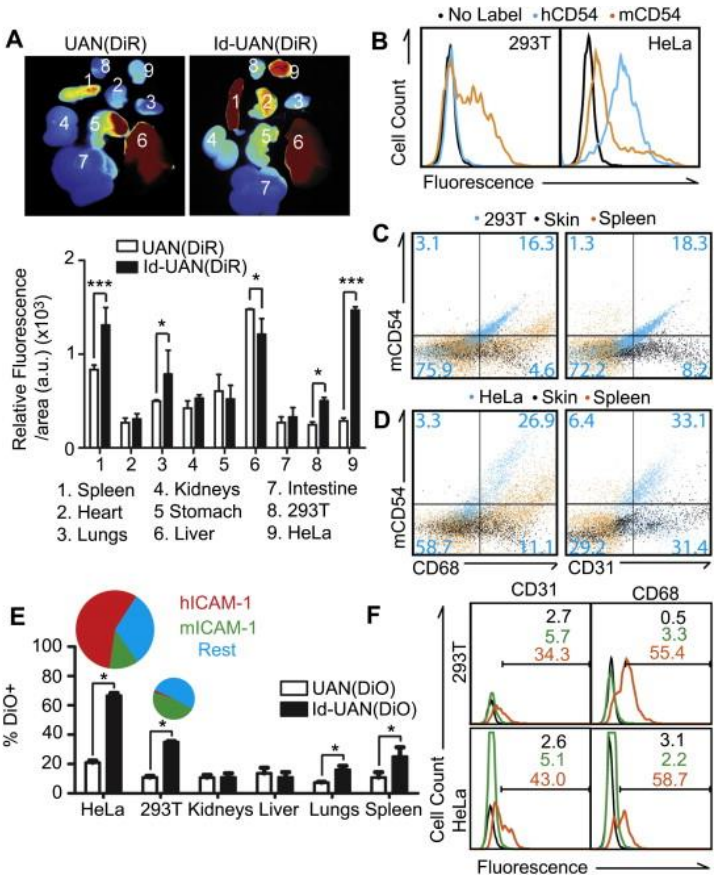

Figure 3.2: Tumor targeting: tissue-/cell-level distribution analysis.
(A) Major organs and tumors at 24 h post-injection of nanoparticles. Mice bearing bilateral HeLa and 293T tumors were injected with either UAN(DiR) or Id-UAN(DiR) (n = 8). (B) CD54 induction in tumor stroma. Cells isolated from untreated HeLa/293T tumors were labeled with antibodies against human (hCD54) or murine ICAM-1 (mCD54). (C and D) Cells isolated from tumors (C: 293T, D: HeLa), skin, and spleen were dual-labeled for mCD54 and mCD68/mCD31 to identify cellular types expressing mCD54. Numbers indicate the percentage of gated populations of cells isolated from tumors. (E) Differentiating cellular uptake of UAN particles from those trapped in an extracellular space. Fluorescence of isolated cells from tumors was measured using flow cytometry (n = 4). Specificity of Id-UAN(DiO) against ICAM-1 is shown in pie charts. After injection of Id-UAN(DiO) or UAN(DiO), cells from tumors were isolated and labeled with antibodies against hCD54 or mCD54. (F) Mice carrying bilateral HeLa and 293T tumors were intravenously injected with Id-UAN(DiO) (orange), UAN(DiO) (green), or PBS (black) 24 h preceding the excision and cell isolation. The cellular components of tumors labeled with Id-UAN(DiO) vs. UAN(DiO) were identified via labeling for mCD31, or mCD68 (Error bars are SDs. *$p < 0.05$, ***$p < 0.001$; two-way ANOVA test followed by Bonferroni post hoc test.).

tumor being 2.0-fold higher compared to the DiO^+ cells in 293T. Cellular uptake of Id-UAN nanoparticles in both tumors was specific to ICAM-1; 50-80% of DiO-positive cells were also positive for either human or murine ICAM-1 (Fig. 3.2E; shown in the pie charts). Cellular-level analysis, however, showed that larger amounts of nanoparticles were internalized by the tumors than the organs (e.g., liver and spleen) which is in contrast to the ex vivo imaging of the organs and tumors that showed higher levels in the organs. This discrepancy, therefore, should point to the possibility of the particles being present in the extracellular spaces of these organs, causing them to be removed during the process of isolating cells for flow cytometry.

In order to quantify the percentage of tumor stromal cells that had internalized Id-UAN(DiO) and UAN(DiO), HeLa and 293T tumors were excised and digested for another series of flow cytometry analyses, conducted at 24 h after the injection of Id- UAN(DiO) and UAN(DiO). Collected cells were labeled with antibodies against CD31 and CD68. We found that among DiO-positive cells that were analyzed, 35-60% of the cells were positive for CD31 or CD68, proving that Id-UAN(DiO) was indeed taken up by both the vasculature endothelium and macrophages, as the two major constituents in tumor stroma (Fig. 3.2F).

Greatly enhanced EC_{50} via molecular interaction-guided drug delivery

In an attempt to validate UAN as an effective drug delivery vehicle, we used paclitaxel, a water-insoluble chemotherapeutic drug. After encapsulation of PTX, we first examined the effectiveness of Id-UAN(PTX) in specifically attenuating the growth of ICAM-1-expressing cells in vitro (Fig. 3.3A). HeLa cells were exposed to either free paclitaxel, UAN(PTX), or Id-UAN(PTX) for only 10 min to model the transient exposure of drugs to a tumor in an in vivo system. Cells

were then cultured for 72 h prior to cell viability quantification. Compared to UAN(PTX), which would induce cell death through slow release of PTX or non-specific uptake, the attachment of the I domain to the particles drastically improved the cytotoxic effects (EC_{50} = 1 μM by Id-UAN(PTX) vs. 37.5 μM by UAN(PTX)), highlighting the added advantage of active targeting for drug carriers such as UAN. Free PTX resulted in EC_{50} = 63 μM, significantly higher than those reported in other studies with longer incubation times, indicating PTX was not efficiently taken up by the cells during the 10-min exposure. Possible cytotoxic effects induced by UAN particles themselves were also examined by treating the cells with only the carrier, Id-UAN, at different concentrations. The results demonstrated that empty vehicles on their own (EC_{50} = 4.4 mg/ml) would have minimal cell killing effect at the concentrations used in the subsequent in vivo experiments (200 μg of UAN per mouse). The difference in cytotoxicity made by the presence of I domain on the surface of UAN was reexamined using the following PTX concentrations: 35, 1, and 0.2 μM (Fig. 3.3B). Although all other formulations were only marginally effective at PTX concentrations up to 35 μM, Id-UAN(PTX) was able to confer ~50% specific cell death at 1 μM.

Molecular interaction-guided tumor attenuation and systemic toxicity *in vivo*

After confirming selective delivery by the I domain, which targeted not only ICAM-1-positive tumor cells but also the stromal cells over-expressing ICAM-1, we evaluated the therapeutic efficacy of paclitaxel-loaded UAN particles in HeLa and 293T tumor xenografts. When the tumors reached a size of ~100 mm^3, mice were intravenously injected three times over 6 days with PBS, UAN(PTX), or Id-UAN(PTX). 3-4 days after the last injection, mice were sacrificed for further ex vivo analyses (Fig. 3.4A). Consistent with the tissue- and cellular-level

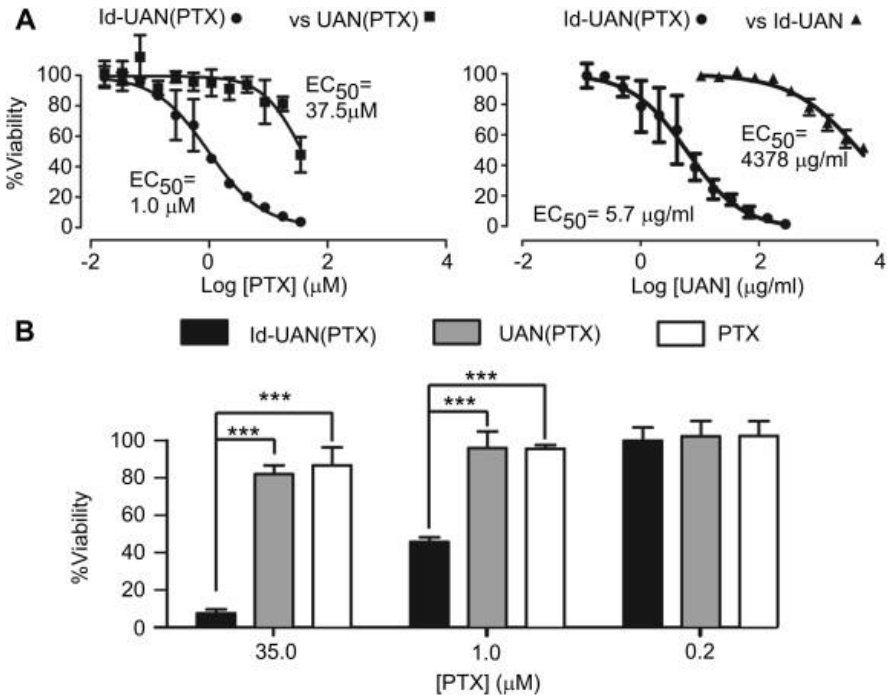

Figure 3.3: In vitro EC_{50} comparison between Id-UAN(PTX), UAN(PTX), and PTX.
(A) HeLa cells subcultured in 24-well plates were treated for 10 min with varying concentrations of Id-UAN(PTX), UAN(PTX), PTX, or Id-UAN. At 72 h, cells were stained with trypan blue for differentiation of live/dead cells (n = 3). (B) Cell viability at select concentrations of PTX is shown in a bar graph (Error bars are SDs. *p < 0.05, ***p < 0.001; Two-way ANOVA test followed by Bonferroni post hoc test).

biodistribution of UAN particles (Fig. 3.2), Id-UAN(PTX) treatment resulted in significant inhibition of tumor growth in both HeLa and 293T tumors (Fig. 3.4B), while little inhibition was observed in mice treated with UAN(PTX) compared to the PBS control (Fig. 3.4C). The image of the tumors recapitulated the notable difference between the efficacy of Id-UAN(PTX) and UAN(PTX) in tumor suppression (Fig. 3.4D). In addition to the difference in tumor size, the tumors treated with UAN(PTX) appeared darker due to abundant vasculatures in these tumors. On the other hand, tumors from mice administered with Id-UAN(PTX) seemed to lack the dark-red appearance, possibly due to the disruption of the tumor-associated vessels. Here, it needs to be reemphasized that the growth inhibition of 293T tumors by Id-UAN(PTX) should mainly come from the delivery of paclitaxel into the tumor stroma, presenting an evidence for tumor suppression achieved via drug carriers targeting the inflamed tumor microenvironment. To gauge the potential use of targeted UAN as drug carriers in clinics, we carried out a systemic toxicity assay associated with Id-UAN(PTX) by measuring the activity levels of ALT/AST enzymes in serum as well as the body weight of the mice (Fig. 3.4E and F). The ALT activity levels increased slightly 9-12 days after the first treatment but were below the levels indicative of liver toxicity (~56 mU/ml). Overall, no significant differences in ALT/AST levels and the rate of increase in body weight during the treatments were observed between the mice treated with UAN(PTX) and those treated with Id-UAN(PTX). Despite Id-UAN(PTX)'s cytotoxic effect on the tumors, the low to minimum levels of liver toxicity as well as the normal rate in body weight increase indicate that the particles were inert to non-specific interaction and were residing mostly in the extracellular space in the major organs.

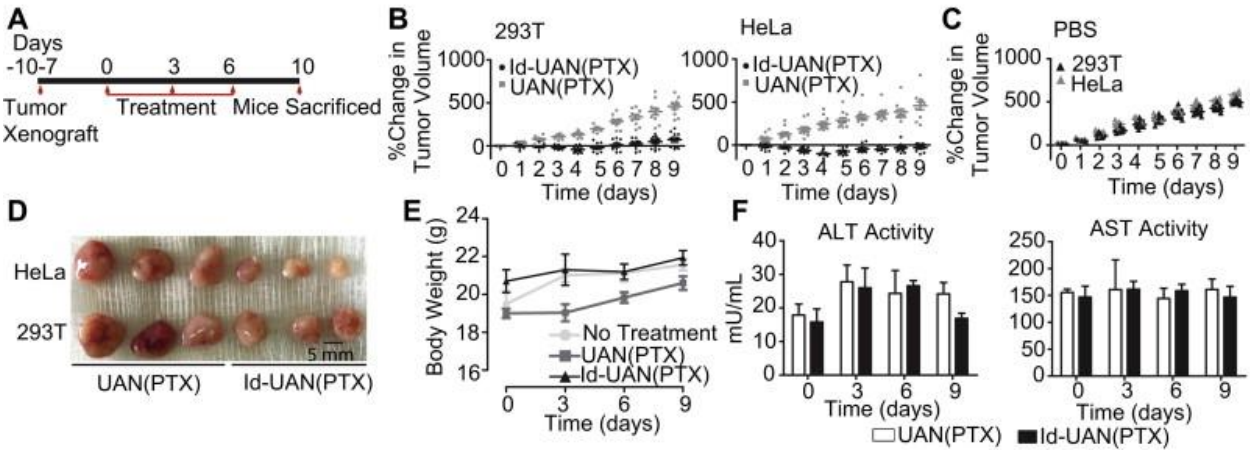

Figure 3.4: Effects of Id-UAN(PTX) therapy on tumor growth in HeLa/293T xenografts and toxicity.

(A) Timeline of tumor xenograft, nanoparticle injections, and ex vivo analysis is shown. (B) Mice bearing bilateral HeLa and 293T tumors were injected with either PBS, UAN(PTX), or Id-UAN(PTX). Tumor size in each mouse was measured daily. The difference in tumor size due to the treatment with Id-UAN(PTX) vs. UAN(PTX) was statistically significant beginning on day 3 for 293T and day 2 for HeLa ($p < 0.001$). (C) Change in tumor volume in mice receiving PBS. (D) Representative image of tumors excised from each group (scale bar, 5 mm). (E) Mean body weight of mice after each round of injections of UAN(PTX) or Id-UAN(PTX) on days 0, 3, 6, and 9. (F) Measurement of activity levels of ALT and AST in serum over the course of treatment. Blood was collected on days 0, 3, 6, and 9, prior to injection of nanoparticles (error bars are SDs).

Discussion

Utilizing polymeric nanoparticles as drug carriers, here we report that molecular markers induced in pro-inflammatory tumor microenvironment may provide a therapeutic strategy that is applicable to the suppression of different types of tumors independent of their tumor surface antigens. Among the surface markers that closely follow the degree of inflammation, we have chosen ICAM-1, a molecule that is rapidly upregulated in response to inflammation. With a targeting moiety against ICAM-1 incorporated into our nanoparticles, UAN was found to be internalized into not only ICAM-1-positive tumors but also the tumor-associated vasculature ($CD31^+$) and macrophages ($CD68^+$). The ability of ICAM-1-targeted nanoparticles to deliver paclitaxel into CD31/CD68-positive cells resulted in suppression of ICAM-1-negative 293T tumors.

Nanoparticle-based drug carriers that are devoid of molecular targeting rely heavily on leaky tumor vessels. However, tumor vessels available to many drug carriers of ~100 nm in size are sparsely distributed, particularly near high-level expression of vascular endothelial growth factor receptors[31]. Though nonleaky tumor microvasculature may still be permeable to molecules much smaller (less than ~12 nm), the large size of most drug carriers renders them inadequate for delivery in this route[32]. In order to address this problem, substantial research has been dedicated to identifying molecular markers in tumor-associated vasculature, also called the 'vascular zip codes'[10]. The luminal side of tumor-associated vessels is available to blood-borne particles and, once bound, the drug carriers can easily access the tumor interior[33]. Several molecules have been reported to be over- or uniquely expressed in tumor-

associated vessels and used as therapy targets (e.g., αv integrin[10, 34, 35]; ED-B domain of fibronectin[11], and VCAM-1[36]). Recently, it has been demonstrated that VCAM-1, a cell adhesion molecule that interacts with α4β1 integrin, was induced in the cerebral vasculature in the vicinity of brain metastases[36, 37]. Similarly, we have found overexpression of ICAM-1 in the vascular endothelium associated with tumors[13, 38-40]. Multimeric binding and clustering of ICAM-1 triggers cellular internalization of bound particles, and it has been shown that ICAM-1 can be recycled back to the cell surface after endocytosis[41], providing a mechanism to deliver drug agents in repeated doses. We have also found that ICAM-1 is induced in other tumor microenvironment mediators besides tumor-associated endothelium, such as macrophages and the tumors themselves[38, 41-43]. Hence, using a targeting probe with tumor-homing properties for a molecular signature shared between tumor stroma and tumor cells can provide synergistic advantages.

The majority of drug carriers are designed to either induce nonspecific cellular uptake or rapidly release drugs outside of cells after extravasation into or in the vicinity of tumors to achieve maximum therapeutic effect. However, nanoparticles possessing such properties would inevitably cause systemic toxicity as they would be prone to release cytotoxic drugs to phagocytic and parenchyma cells in major organs[2]. UAN nanoparticles used in this study were, however, designed to encapsulate and stably retain hydrophobic molecules. Without internalization into the cells, the release rate of cancer drugs from UAN would be too slow to produce significant cytotoxicity[29]. Polyethylene moiety forming the outer layer of UAN was introduced to greatly reduce opsonization and non-specific uptake by parenchyma and phagocytic cells. These properties of UAN nanoparticles in the absence of active targeting led to

their accumulation mainly into interstitial space within the major organs, resulting in low levels of toxicity. The insignificant tumor attenuation by the non-targeted UAN is also ascribed to the need for a much higher dose of PTX required to have cytotoxic effects compared to that of ICAM-1-selective delivery (EC_{50} = 1 μM with targeted vs. 37.5 μM with non-targeted). The nickel-NTA moiety present at the terminal hydroxyl group of polyethylene makes UAN particles highly versatile for facile conjugation with targeting ligands with a His-tag, obviating highly unpredictable chemical conjugations. The ability of drug carriers to actively bind target cells is vital to lessen the barriers created by the elevated interstitial fluid pressure[39, 44, 45], which retards the penetration of drug carriers deep into tumors and even forces them back into circulation. Rapid binding and subsequent receptor-mediated endocytosis, therefore, may overcome such limitations of many non-targeted drug carriers.

Conclusions

In this work, we have successfully engineered polymeric drug carriers to target ICAM-1-expressing tumors as well as inflamed tumor microenvironment. UAN has exhibited its advantages as a targeted drug carrier for its ability to evade the mononuclear phagocytic system and cause low levels of systemic toxicity. By targeting an inflammatory marker in tumor vessels, Id-UAN particles may act as a double-edged sword: Not only will they be able to localize drug delivery to the tumor site, they may also inhibit the infiltration of LFA-1-expressing pro-tumor immune cells by occupying ICAM-1 on endothelium or by promoting internalization of the receptors. As demonstrated with ICAM-1-negative 293T tumor, the upregulation of ICAM-1

in the tumor environment can be utilized to deliver chemotherapeutics to tumors lacking unique markers. UAN's ability to encapsulate and deliver a cocktail of hydrophobic drugs may also aid in addressing the problems of drug-resistance.

Acknowledgments

This work was funded by a National Science Foundation (NSF) GK-12 Fellowship Award and Business for International Cooperative R&D between Industry, Academy, and Research Institute (Korea Small and Medium Business Administration, Grant No. 00042115).

REFERENCES

1. Yuan, F., et al., *Vascular permeability in a human tumor xenograft: molecular size dependence and cutoff size.* Cancer Res, 1995. **55**(17): p. 3752-6.
2. Li, S.D. and L. Huang, *Pharmacokinetics and biodistribution of nanoparticles.* Mol Pharm, 2008. **5**(4): p. 496-504.
3. Hambley, T.W., *Is Anticancer Drug Development Heading in the Right Direction?* Cancer Research, 2009. **69**(4): p. 1259-1261.
4. Jain, R.K., *Transport of molecules, particles, and cells in solid tumors.* Annual Review of Biomedical Engineering, 1999. **1**: p. 241-263.
5. Danquah, M.K., X.A. Zhang, and R.I. Mahato, *Extravasation of polymeric nanomedicines across tumor vasculature.* Advanced Drug Delivery Reviews, 2011. **63**(8): p. 623-639.
6. Jain, R.K. and T. Stylianopoulos, *Delivering nanomedicine to solid tumors.* Nature Reviews Clinical Oncology, 2010. **7**(11): p. 653-664.
7. Kong, G., R.D. Braun, and M.W. Dewhirst, *Hyperthermia enables tumor-specific nanoparticle delivery: Effect of particle size.* Cancer Research, 2000. **60**(16): p. 4440-4445.
8. Chen, B., et al., *Tumor vascular permeabilization by vascular-targeting photosensitization: Effects, mechanism, and therapeutic implications.* Clinical Cancer Research, 2006. **12**(3): p. 917-923.
9. Watson, K.D., et al., *Ultrasound Increases Nanoparticle Delivery by Reducing Intratumoral Pressure and Increasing Transport in Epithelial and Epithelial-Mesenchymal Transition Tumors.* Cancer Research, 2012. **72**(6): p. 1485-1493.
10. Sugahara, K.N., et al., *Tissue-Penetrating Delivery of Compounds and Nanoparticles into Tumors.* Cancer Cell, 2009. **16**(6): p. 510-520.
11. Nilsson, F., et al., *Targeted delivery of tissue factor to the ED-B domain of fibronectin, a marker of angiogenesis, mediates the infarction of solid tumors in mice.* Cancer Research, 2001. **61**(2): p. 711-716.
12. Turk, M.J., D.J. Waters, and P.S. Low, *Folate-conjugated liposomes preferentially target macrophages associated with ovarian carcinoma.* Cancer Letters, 2004. **213**(2): p. 165-172.
13. Chen, X.Y., et al., *Inflamed leukocyte-mimetic nanoparticles for molecular imaging of inflammation.* Biomaterials, 2011. **32**(30): p. 7651-7661.
14. Ogawa, Y., et al., *Expression of intercellular adhesion molecule-1 in invasive breast cancer reflects low growth potential, negative lymph node involvement, and good prognosis.* Clinical Cancer Research, 1998. **4**(1): p. 31-36.
15. Kelly, C.P., et al., *Human colon cancer cells express ICAM-1 in vivo and support LFA-1-dependent lymphocyte adhesion in vitro.* Am J Physiol, 1992. **263**(6 Pt 1): p. G864-70.
16. Passlick, B., et al., *Expression of major histocompatibility class I and class II antigens and intercellular adhesion molecule-1 on operable non-small cell lung carcinomas: frequency and prognostic significance.* Eur J Cancer, 1994. **30A**(3): p. 376-81.

17. Tomita, Y., et al., *Expression of intercellular adhesion molecule-1 (ICAM-1) on renal-cell cancer: possible significance in host immune responses.* Int J Cancer, 1990. **46**(6): p. 1001-6.
18. Koyama, S., T. Ebihara, and K. Fukao, *Expression of intercellular adhesion molecule 1 (ICAM-1) during the development of invasion and/or metastasis of gastric carcinoma.* J Cancer Res Clin Oncol, 1992. **118**(8): p. 609-14.
19. Shimoyama, S., et al., *Overexpression of intercellular adhesion molecule-1 (ICAM-1) in pancreatic adenocarcinoma in comparison with normal pancreas.* Pancreas, 1997. **14**(2): p. 181-6.
20. Buitrago, D., et al., *Intercellular Adhesion Molecule-1 (ICAM-1) is Upregulated in Aggressive Papillary Thyroid Carcinoma.* Annals of Surgical Oncology, 2012. **19**(3): p. 973-980.
21. Schroder, C., et al., *Prognostic value of intercellular adhesion molecule (ICAM)-1 expression in breast cancer.* Journal of Cancer Research and Clinical Oncology, 2011. **137**(8): p. 1193-1201.
22. Roland, C.L., et al., *Tumor-derived intercellular adhesion molecule-1 mediates tumor-associated leukocyte infiltration in orthotopic pancreatic xenografts.* Experimental Biology and Medicine, 2010. **235**(2): p. 263-269.
23. Coussens, L.M. and Z. Werb, *Inflammation and cancer.* Nature, 2002. **420**(6917): p. 860-7.
24. Grivennikov, S.I., F.R. Greten, and M. Karin, *Immunity, inflammation, and cancer.* Cell, 2010. **140**(6): p. 883-99.
25. Shimaoka, M., et al., *Structures of the alpha L I domain and its complex with ICAM-1 reveal a shape-shifting pathway for integrin regulation.* Cell, 2003. **112**(1): p. 99-111.
26. Jin, M., et al., *Directed evolution to probe protein allostery and integrin I domains of 200,000-fold higher affinity.* Proceedings of the National Academy of Sciences of the United States of America, 2006. **103**(15): p. 5758-5763.
27. Kang, S., et al., *Tunable physiologic interactions of adhesion molecules for inflamed cell-selective drug delivery.* Biomaterials, 2011. **32**(13): p. 3487-98.
28. Park, E.J., et al., *Dietary and genetic obesity promote liver inflammation and tumorigenesis by enhancing IL-6 and TNF expression.* Cell, 2010. **140**(2): p. 197-208.
29. Park, S., et al., *Self-assembled nanoplatform for targeted delivery of chemotherapy agents via affinity-regulated molecular interactions.* Biomaterials, 2010. **31**(30): p. 7766-75.
30. Wong, R., et al., *Visualizing and Quantifying Acute Inflammation Using ICAM-1 Specific Nanoparticles and MRI Quantitative Susceptibility Mapping.* Annals of Biomedical Engineering, 2012. **40**(6): p. 1328-1338.
31. Karathanasis, E., et al., *Tumor Vascular Permeability to a Nanoprobe Correlates to Tumor-Specific Expression Levels of Angiogenic Markers.* Plos One, 2009. **4**(6).
32. Sarin, H., et al., *Physiologic upper limit of pore size in the blood-tumor barrier of malignant solid tumors.* Journal of Translational Medicine, 2009. **7**.
33. Ruoslahti, E., S.N. Bhatia, and M.J. Sailor, *Targeting of drugs and nanoparticles to tumors.* Journal of Cell Biology, 2010. **188**(6): p. 759-768.

34. Hood, J.D., *Tumor regression by targeted gene delivery to the neovasculature (vol 296, pg 2404, 2002).* Science, 2002. **298**(5592): p. 364-364.
35. Murphy, E.A., et al., *Nanoparticle-mediated drug delivery to tumor vasculature suppresses metastasis.* Proceedings of the National Academy of Sciences of the United States of America, 2008. **105**(27): p. 9343-9348.
36. Serres, S., et al., *Molecular MRI enables early and sensitive detection of brain metastases.* Proceedings of the National Academy of Sciences of the United States of America, 2012. **109**(17): p. 6674-6679.
37. Dienst, A., et al., *Specific occlusion of murine and human tumor vasculature by VCAM-1-targeted recombinant fusion proteins.* Journal of the National Cancer Institute, 2005. **97**(10): p. 733-747.
38. Melder, R.J., et al., *During angiogenesis, vascular endothelial growth factor and basic fibroblast growth factor regulate natural killer cell adhesion to tumor endothelium.* Nat Med, 1996. **2**(9): p. 992-7.
39. Fukumura, D. and R.K. Jain, *Tumor microvasculature and microenvironment: targets for anti-angiogenesis and normalization.* Microvasc Res, 2007. **74**(2-3): p. 72-84.
40. Yoong, K.F., et al., *Vascular adhesion protein-1 and ICAM-1 support the adhesion of tumor-infiltrating lymphocytes to tumor endothelium in human hepatocellular carcinoma.* J Immunol, 1998. **160**(8): p. 3978-88.
41. Mizoi, T., et al., *Intercellular adhesion molecule-1 expression by macrophages in human gastrointestinal carcinoma: possible roles as host immune/inflammatory reaction.* Pathol Int, 1995. **45**(8): p. 565-72.
42. Blank, C., et al., *ICAM-1 contributes to but is not essential for tumor antigen cross-priming and CD8(+) T cell-mediated tumor rejection in vivo.* Journal of Immunology, 2005. **174**(6): p. 3416-3420.
43. Fukumura, D., S. Kashiwagi, and R.K. Jain, *The role of nitric oxide in tumour progression.* Nature Reviews Cancer, 2006. **6**(7): p. 521-534.
44. Heldin, C.H., et al., *High interstitial fluid pressure - An obstacle in cancer therapy.* Nature Reviews Cancer, 2004. **4**(10): p. 806-813.
45. Padera, T.P., et al., *Lymphatic metastasis in the absence of functional intratumor lymphatics.* Science, 2002. **296**(5574): p. 1883-1886.

CHAPTER 4

Affinity-tuned leukocyte integrin chimeric antigen receptor T cells for increased therapeutic index against tumors in mice

Summary

Due to the lack of tumor-specific antigens that demarcate tumor from normal tissue, on-target off-tumor toxicity has become a significant hurdle encountered in the development of chimeric antigen receptor (CAR) T cells for solid tumors. The target antigen recognition site within the CAR design is often a single chain variable fragment (scFv) derived from antibodies that exhibit affinities that are sufficiently high to bind physiologic levels of target antigens. In this study, we have replaced the scFv region with a natural ligand recognizing an adhesion molecule that is highly inducible in inflammatory settings, such as tumor microenvironment. By tuning the affinities of CAR, we engineered T cells to have a wide range of binding capabilities against target. A panel of CAR T cells with affinities varying over six orders of magnitude was generated to functionally screen for CAR T cells that can discriminate tumors and stromal cells overexpressing target from normal tissues that express it at physiologic levels. High-affinity CAR T cells recognized the target antigen at all levels of expression, consistently leading to fatalities in hosts. Affinity-tuning, however, allowed us to isolate CAR T cells displaying robust antitumor efficacy while sparing normal cells expressing low target density. The proposed affinity-tuning methodology endows the potent CAR T cell technology a strategy to selectively target antigens overexpressed on solid tumors with improved therapeutic index.

Introduction

Chimeric antigen receptor (CAR) T cells are composed of synthetic binding moieties that direct T cells to target antigens for subsequent eradication. Using this technology, adoptive immune therapy has achieved extraordinary success in eradicating blood-borne cancers, prominently, the CD19 CAR T cells in B cell leukemias and lymphomas[1-4]. However, the application of this powerful technology in solid tumors has been limited due to the scarcity of tumor antigens that are deemed safe for targeting. As such, in spite of the increasing clinical trials focusing on solid tumor target antigens[5, 6], the clinical results have not been promising and ways to improve the performance are being actively investigated.

Ideally, a target tumor antigen is highly expressed on the surface of tumor cells but not on healthy normal tissues. However, many commonly targeted tumor antigens, such as human epidermal growth factor receptor 2 (ErbB2), epidermal growth factor receptor (EGFR), mucine 1 (MUC1), prostate-specific membrane antigen (PSMA), and diganglioside (GD2)[5] are also expressed by non-tumor tissues. This means with sufficiently high affinity to such antigens, healthy cells can also be recognized by CAR T cells. Toxicities arising from this, known as on-target, off-tumor toxicity, has therefore become the major limiting factor in the progress of CAR technology. Though in the case of CD19 CAR T cells, the expression of CD19 on all B cells has not been a critical factor since depletion of B cells is manageable, recent reports on severe adverse toxicities associated with CAR T cells[7-9] illustrate the importance of ligand/receptor pair selection for safe and efficient therapy.

The single chain variable fragment (scFv) domain of the CAR design against target antigen is derived from antibodies selected for high affinity to target. Though this trait allows CAR T cells to bind efficiently to target tumor cells, it also renders it difficult for CAR T cells to distinguish between tumor cells and normal tissues expressing lower levels of antigen. Such methods for generating CARs by selecting high affinity scFvs have shown to exhibit lower activation thresholds compared to low affinity scFvs[10]. In addition, others have found that there is an optimum range of recognition affinity for T cell activation, and further increasing the affinity only decreases selectivity[11, 12].

In this study, we have equipped T cells with affinity-tuned CARs that specifically target intercellular adhesion molecule (ICAM)-1, a molecule that has been shown to be dynamically upregulated in many carcinomas compared to normal tissues. The recognition domain of this CAR design is composed of the inserted (I) domain of a leukocyte integrin called lymphocyte function-associated antigen (LFA)-1. Previously, the I domain has been engineered using directed evolution to isolate variants exhibiting affinities to ICAM-1 that spanned six orders of magnitude (K_D ~1 nM to 1 mM)[13]. We found that increasing the affinity of I domain to the natural TCR/pMHC affinity range could significantly increase the therapeutic index of CARs, while increasing the affinity further caused unbiased reactivity against all ICAM-1-expressing cells. After arming CAR T cells with the various I domain mutants, we sought to determine whether the ability of T cells to discriminate tumors from normal tissues could be recovered at lower affinities. Since human LFA-1 I domain exhibits the unique quality of cross reacting with both murine and human ICAM-1 with comparable affinities[14], it allowed for simultaneous comparison of performance against high density of human ICAM-1 expressed on tumors and

low density murine ICAM-1 expressed on normal tissue. To our knowledge, this study presents the first robust examination of on-target, off-tumor toxicity to host in a preclinical setting.

Experimental Procedures

Cell lines and primary human lymphocytes

Human dermal microvascular endothelial cells (HMEC-1) were obtained from the Center for Disease Control. HMEC-1 was cultured in MCDB 131 medium (Invitrogen) supplemented with 10% (v/v) fetal bovine serum (FBS; Atlanta Biologicals), 10 mM L-alanyl-L-glutamine dipeptide (Gibco), Penicillin-Streptomycin (Pen-strep; 100 units/ml), 1 ug/ml hydrocortisome (MP Biomedicals), and 10 ng/ml recombinant human epidermal growth factors (Invitrogen). Mouse brain microvascular endothelial cells (bEnd.3, ATCC) were maintained in Advanced Dulbecco's Modified Eagle Medium (DMEM) medium supplemented with 4 mM L-glutamine, Pen-strep, and 10% FBS. HeLa cells (ATCC) were cultured in Advanced DMEM medium (Invitrogen) containing 10% FBS, 2 mM L-glutamine, and Pen-strep. 8505c cells (DSMZ) were cultured in RPMI-1640 medium (Invitrogen) containing 10% FBS, 2 mM L-glutamine, and Pen-strep. HMEC-1, bEnd.3, HeLa, and 8505c cells were transduced with lentivirus encoding Firefly Luciferase-F2A-GFP (Biosettia) followed by fluorescence activated cell sorting (FACS) to purify GFP expressing cells.

Human peripheral blood was obtained from healthy volunteer donors by venipuncture. Peripheral blood mononuclear cells (PBMC) were isolated over Ficoll-Paque PLUS (GE Healthcare) and cultured in GIBCO Optimizer CTS T-cell Expansion SFM (Thermo) supplemented

with 5% human AB serum (Sigma), 2 mM L-alanyl-L-glutamine dipeptide, Pen-Strep, and 30 IU/ml human IL-2 (Cell Sciences). Non-adherent cells were removed after 24hr and magnetically enriched for T cells with Dynabeads CD3/CD28 T cell expander (Thermo) at a 2:1 bead:T cell ratio. Dynabead-bound T cells were subsequently cultured in IL-2 containing media at a density of 1 - 2 x 10^6 cells/ml. All cells were incubated at 37°C in a 5% CO_2 humidified incubator.

Construction of I domain mutant CAR genes

The genes for LFA-1 I domain exhibiting varying affinities to ICAM-1 were derived from the a previous study[13]. I domain variants were then fused with the transmembrane and cytoplasmic domains of CD28, CD137, and CD3ζ of an independent third generation CAR gene (a kind gift from Dr. Carl June at University of Pennsylvania[15]). The complete CAR inserts were then subcloned into a pLenti backbone.

Lentivirus production and transduction of T cells

Lentivirus was produced by transiently transfecting HEK 293 cells using calcium phosphate. Briefly, 10 µg of transfer gene, 7.5 µg of pCMV-dR8.2 (Addgene) and 5 µg of pCMV-VSVG (Addgene) were mixed and incubated with 2 M $CaCl_2$ followed by 2x HBSS. Resulting solutions were added dropwise to 10 cm^2 cell culture dishes seeded with 3.2 x 10^6 HEK 293 in 10 ml DMEM 24hr previously. Transfection media was replaced after 6 hr. Media containing lentivirus was harvested at 48 and 72hr post transfection, filtered through 0.45 µm filters, and concentrated by ultracentrifugation at 75,000x g for 2hr at 4°C. Lentivirus was then resuspended in serum containing media at an approximate titer of 10^8/ml and frozen at -80°C.

Human T cells were transduced 24 - 72hr post activation with anti-CD3/CD28 Dynabeads either by spinfection at 1,000x g for 1hr at 32°C or by overnight incubation of lentivirus in the presence of Synperonic F108 (Sigma)[16]. T cells were transduced once more 24hr after initial transduction. During and following transduction, media containing IL-2 was replaced with media containing human IL-7 (10 ng/ml) and IL-15 (5 ng/ml) (Peprotech). Jurkat T cells were transduced by a single incubation with lentivirus overnight in the presence of Synperonic F108.

Luciferase-based cytolytic T cell assay

2 x 10^5 target cells (HMEC-1, bEnd.3, HeLa, and 8505c) stably transduced to express GFP and firefly luciferase were co-cultured with either non-transduced or I domain CAR T cells at varying E:T ratios as indicated. In additional conditions, the ICAM-1 gene was deleted from 8505c using CRISPR (Santa Cruz, #sc-400098; denoted as 8505c$^-$) or 8505c was exposed to lipopolysaccharide (LPS) for 12 hours and washed prior to the assay to induce the expression level of ICAM-1 (denoted as 8505c$^+$). Co-cultures were carried out in T cell culture medium containing 150 µg/ml D-Luciferin (Gold Biotechnology) with no cytokine supplementation. Luminesence was measured with a plate reader (TECAN infinite M1000 PRO) with readings in each E:T condition normalized to the non-transduced T cell:target co-culture controls.

8505C mouse model, measurement of ex vivo organs and whole-body tumor growth

7.5 x 10^5 8505c cells were injected into NSG mice via tail vein. 3 x 10^6 T cells were injected via tail vein 10 days after tumor cell injection. Luminescence imaging of tumor xenografts in live mice was performed using a whole body optical imager (In-Vivo Extreme,

Bruker). Mice were anesthetized first with 3% isoflurane in 2 L/min O_2 and subsequent to this, maintained at 2% isoflurane in 2 L/min O_2. Tumor burden was estimated by integration of luminescence over chest cavity and the entire mouse body.

Flow cytometry

Tumor xenografts were resected from mice at appropriate time points. Resected tumors were diced and flushed through an 80 µm cell strainer to yield single cell suspensions. Red blood cells were lysed by incubating with 1x RBC lysis buffer (eBiosciences). Remaining cells were washed, re-suspended in 1x HBSS containing 2% normal goat serum, and then blocked with mouse IgG at 2 µg/ml for 10 min. This was followed by staining with 1 µg/ml Propidium Iodide (Invitrogen) in combination with 2 µg/ml murine anti-human CD3-Alexa Fluor 647 (Biolegend) or 2 µg/ml rabbit anti-c-myc-Alexa Fluor 647 (Biolegend). Flow cytometry gates were determined based on live cell gating (Propidium Iodide negative). ICAM-1 expression on tumor cell lines was determined using a murine anti-human R6.5 monoclonal antibody (10 µg/ml) obtained from hybridoma (ATCC). I domain-CAR expression on T cells was detected using 2 µg/ml rabbit anti-c-myc-Alexa Fluor 647 (Biolegend).

ICAM-1 binding assay

I domain Jurkat T cell variants were incubated with 10 ug/ml recombinant human ICAM-1 fused to human Fc (R&D Systems). The cells were then washed and resuspended in 1 ug/ml rabbit anti-human PE (Santa Cruz Biotechnology) prior to FACS analysis.

ELISA assays

Target cells were washed and suspended at 1×10^6 cells/ml in T cell culture medium without cytokines. 100 µl each target cell type was added in triplicate to a 96-well round bottom plate (Corning). Effector T cells were washed and resuspended at 5×10^6 cells/ml in T cell culture medium without cytokines and then 100 µl of T cells were combined with target cells in the indicated wells. The plates were incubated at 37°C for 24 - 48 hours. After the incubation, supernatant was harvested and subjected to an ELISA assay (Biolegend).

CD25 staining

Cells were plated at an effector to target ratio of 1:1 (1×10^5 effectors: 1×10^5 targets) in 150 µl of Jurkat cell culture medium in a 96-well plate. The plate was incubated at 37°C for 6 hours. After incubation, the cells were washed with PBS containing 0.1% bovine serum albumin (BSA) (FACS buffer) prior to being labeled with 2 ug/ml anti-human CD25-allophycocyanin (APC; Biolegend) for 30 minutes on ice. After incubation, samples were washed with the FACS buffer and analyzed by flow cytometry.

Statistical analysis

One-way ANOVA and unpaired Student's t-test were performed using Prism (GraphPad) on data indicated.

Results

Altering the affinity of I domains against ICAM-1

Monovalent affinities of the LFA-1 I domain variants for ICAM-1 span six orders of magnitude (K_D ~1 nM to 1 mM) as measured by surface plasmon resonance (SPR) or flow cytometry (Fig. 4.1A)[13]. Various I domain mutations in the region known as the metal-ion dependent adhesion site (MIDAS; F265S) and the C-terminal α7-helix (F292A, F292G), whose downward shift has been shown to cause allosteric changes in the conformation of MIDAS, led to step-wise increases in the affinity against ICAM-1 (Fig. 4.1B). A combination of mutations (F265S/F292G) coupled with an insertion of a disulfide bond to stabilize the MIDAS in its high-affinity conformation (G311C), has led to a remarkable increase in the affinity, dubbed triple-mutant (TM). Together, the affinity of wild-type I domain to ICAM-1 was increased from 1500 mM to 1 nM (Table 1), to allow a rigorous study on the effect of protein binding affinity in CAR T cell therapy. An additional advantage of using human I domain is its ability to bind murine ICAM-1 with comparable affinity (K_D ~2 nM vs. 6 nM respectively), which helps us to examine the way various I domain CAR T cells interact with host's ICAM-1 expressed on healthy cells in preclinical mouse models (Fig. 4.1C). In essence, it helps us determine the on-target, off-tumor toxicity in mouse tumor models to project how the CAR T cells may behave in human patients.

The R6.5 scFv (adopted from the mouse hybridoma clone, R6.5) only binds human ICAM-1 (K_D ~10 nM) (Table 1) and therefore is used in this study as a model system representing CAR T cells that only cause on-target, on-tumor toxicity. This is useful to help us

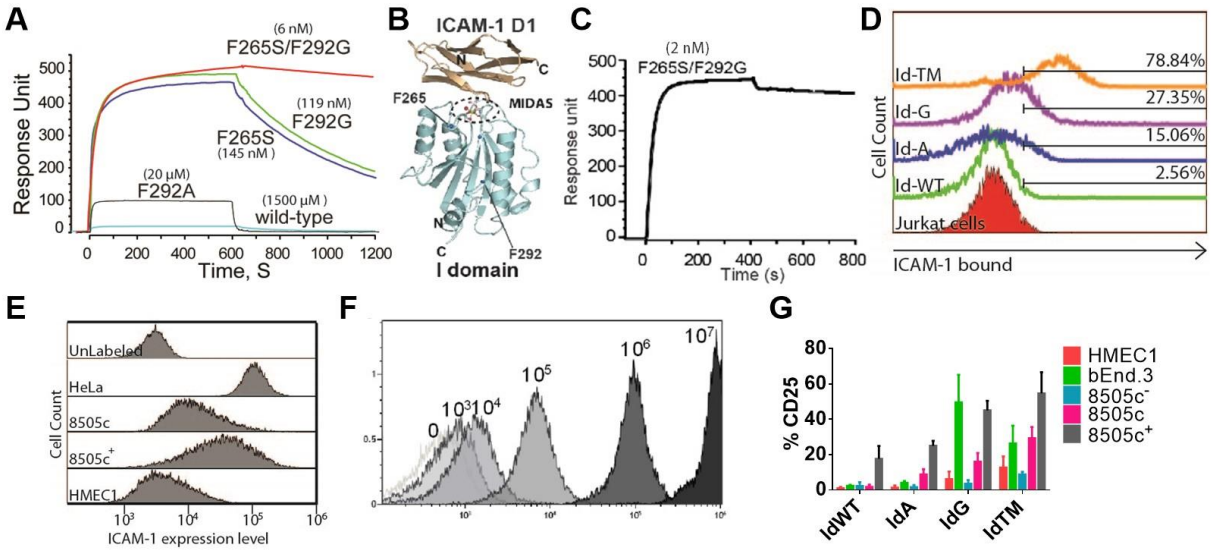

Figure 4.1: ICAM-1 interaction with monovalent LFA-1 I domain variants and I domain-CAR T cells.

(A) SPR measurements of I domain variants to human ICAM-1. (B) Structural model of LFA-1 I domain and ICAM-1. (C) SPR measurement of F265S/F292G I domain to murine ICAM-1. (D) Soluble human ICAM-1 binding to I domain-CAR T cells of varying affinities. (E) ICAM-1 expression on various cell lines. (F) FACS histograms of latex beads coated with 10^3 – 10^6 R6.5 antibody per bead. (G) Induction of activation (CD25) in Jurkat T cells stably expressing I domain-CARs of varying affinities to ICAM-1 after stimulation by cell lines expressing different levels of ICAM-1.

Table 1: Affinity variants of LFA-1 I domain

Name	Affinity
Wild-type (IdWT)	1.5 mM
F292A (IdA)	20 μM
F265S (IdS)	145 nM
F292G (IdG)	119 nM
F265S/F292G/G331C (IdTM)	~1 nM
R6.5 scFv	10 nM*

*Estimated from titrated R6.5 binding to HeLa cells

interpret the degree of toxicity to host caused by off-tumor activity from I domain CAR T cells attacking the basal ICAM-1 expression in normal mouse tissues.

Careful interplay between CAR affinity and target antigen density influences T cell activation and the therapeutic index of I domain CAR T cells in vitro

Theoretically, the binding capabilities of the different I domain CAR T cells should adhere to the pattern exhibited by monovalent I domain mutants. When Jurkat T cells (JC) stably expressing I domain-CARs of varying affinities were exposed to soluble ICAM-1, affinity-dependent increase in binding was observed (Fig. 4.1D). The expected affinity-dependent behavioral pattern of I domain-CAR T cells allowed the subsequent systematic evaluation of affinity and avidity thresholds for activation of T cells. To accomplish this, we assembled a collection of target cells, characterized by a wide range of ICAM-1 expression as measured by flow cytometry (Fig. 4.1E). The expression levels of ICAM-1 in the target cells were estimated by utilizing latex beads coated with known densities of human ICAM-1 as reference (Fig. 4.1F). HMEC-1 represents human non-tumor cells expressing a physiologic level of human ICAM-1 ($<10^5$ per cell). Anaplastic thyroid carcinoma (8505c) and cervical cancer (HeLa) cell lines expressed intermediate (10^5 - 10^6 per cell) and high human ICAM-1 ($>10^6$ per cell). In $8505c^-$, ICAM-1 gene is deleted by CRISPR, while $8505c^+$ is treated with lipopolysaccharides (LPS) to upregulate the expression of ICAM-1.

Different I domain CAR-JCs were stimulated with the target cells and cell activation was assessed by upregulation of CD25, which demonstrated activation correlating with ICAM-1 affinity (Fig. 4.1G). Lowest-affinity WT I domain (IdWT) CARs were activated only in the

presence of high density of ICAM-1 on 8505c^{+}, but could not discriminate among the cells expressing lower levels. Highest-affinity I domain CAR (IdTM), on the other hand, were non-selectively activated to all levels of ICAM-1. Another high-affinity I domain CAR (IdG) also behaved in a promiscuous manner, recognizing moderate to high levels of human ICAM-1 and low levels of murine ICAM-1. However, IdA-CAR T cells successfully recognized only 8505c as well as 8505c^{+}, becoming activated against the tumor cell lines but not the normal cells expressing basal levels of ICAM-1.

Then, primary human T cells transduced with different I domain CAR designs (IdWT, IdA, IdG, and IdTM) were tested against the same panel of target cells to determine the cytotoxic capabilities (Fig. 4.2A). Our results indicate that for all the I domain CAR T cells, the rate of target killing correlated with increasing levels of ICAM-1 expression, with higher ICAM-1 expressing cells being more sensitive to CAR T cell lysis. The rate of killing also correlated well with ICAM-1 affinity. Cytokine release during target cell lysis, measured by IFN-γ, exhibited a similar pattern (Fig. 4.2B). To quantitatively compare the efficacy of killing by affinity variant CAR T cells, values for the time required to achieve 50% killing (t_50%) were obtained from a best fit variable slope sigmoidal curve (%live = $100/[1+10^{(t\_50\%-t)*\,Slope}]$) (Fig. 4.2C). Our analyses demonstrate, in addition to the previously observed patterns, that high affinity CAR T cells (IdG and IdTM) are less sensitive to variations in target antigen density, and that low-affinity I domain CAR T cells were insensitive to low levels of target antigen density.

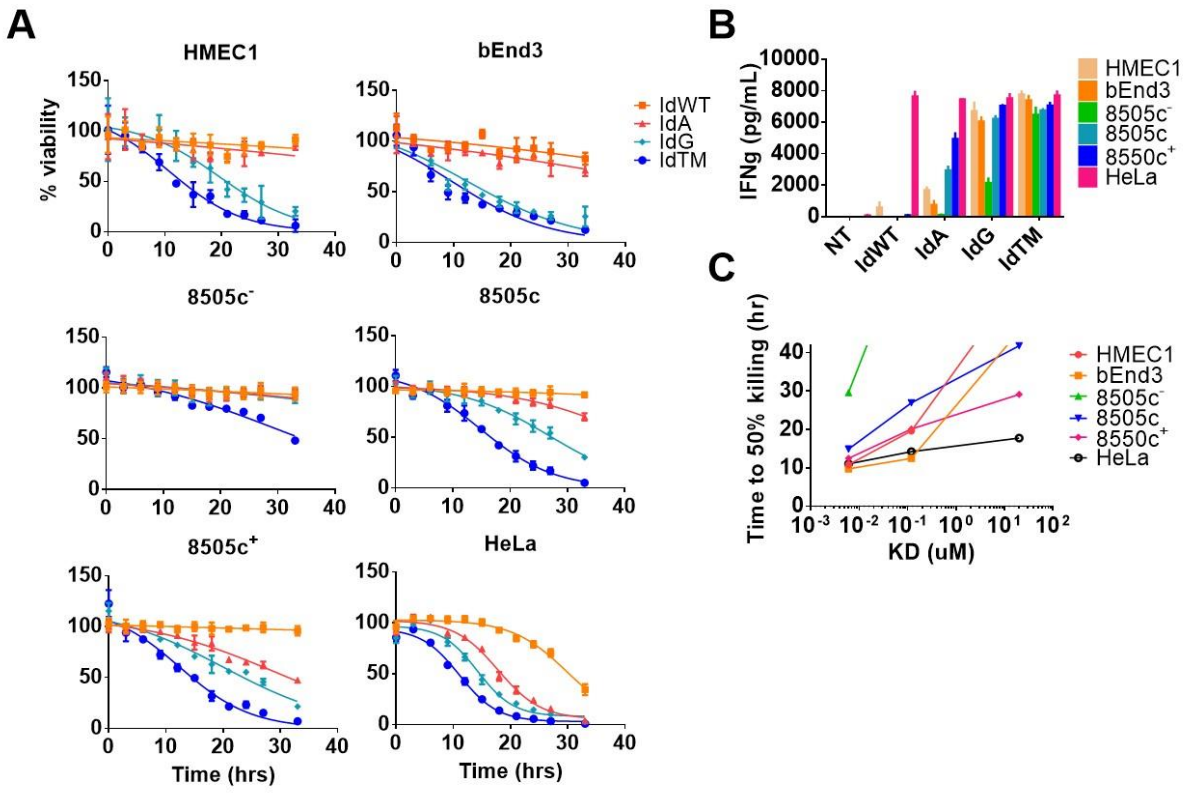

Figure 4.2: Control of target recognition density via affinity-tuning.
(A) Luminescence-based cytolytic activity measurement against different expression densities of ICAM-1 (solid lines are fitted sigmoidal curves). E:T ratio used was 5:1. (B) IFNγ secretion by the panel of I domain-CAR T cells stimulated by different cell lines (ELISA). (C) Values for time required to achieve 50% target lysis obtained from fitted sigmoidal curves as a function of CAR affinity.

Affinity-tuned I domain CAR T cells eliminate tumor in vivo and significantly reduce on-target, off-tumor toxicity against physiologic levels of ICAM-1

To extend the above *in vitro* results, the efficacy of affinity-tuned CAR T cells was examined in both systemic and subcutaneous tumor xenograft models *in vivo*. NSG mice were xenografted systemically with 8505c followed by treatment with the I domain variant CAR T cells (IdWT, IdA, IdS, and IdTM), R6.5-CAR T cells, mock-transduced T cells (Mock), control non-transduced T cells (NT), and no T cells (NoT) 10 days after xenoplantation. Tumor burden was evaluated by whole-body luminescence imaging of firefly luciferase activity. Primary tumors localized to the lungs and liver with distant metastatic foci evident throughout the body[18]. 8505c, which expresses ICAM-1 at a level only moderately higher than normal cells, was used as the model tumor cell line to highlight the applicability and potential of the affinity-tuning method we present here.

Independent 8505c tumor growth, observed in mice receiving no treatment or NT cells, resulted in approximately 100-fold increase in luminescence over a three-week period (Fig. 4.3A). In contrast, human ICAM-1-specific R6.5 CAR T cells began to show decrease in tumor burden 6 days after T cell infusion (Fig. 4.3B). Similarly, IdA, IdS and IdTM-CAR T cells displayed patterns of rapid tumor lysis (Fig. 4.3B, C). However, after approximately 7-10 days after receiving T cell infusion, all of the IdTM-CAR T-treated mice began to show symptoms of systemic toxicity (Fig. 4.3D) and eventually succumbed to death by day 14 after treatment. Subsequent autopsy and flow cytometry revealed drastic expansion of IdTM-CAR T cells in the lungs (~55% human CD3 T cells as a percentage of total lung cells) and spleen combined with severe lung tissue hemorrhaging, suggesting the occurrence of on-target, off-tumor toxicity

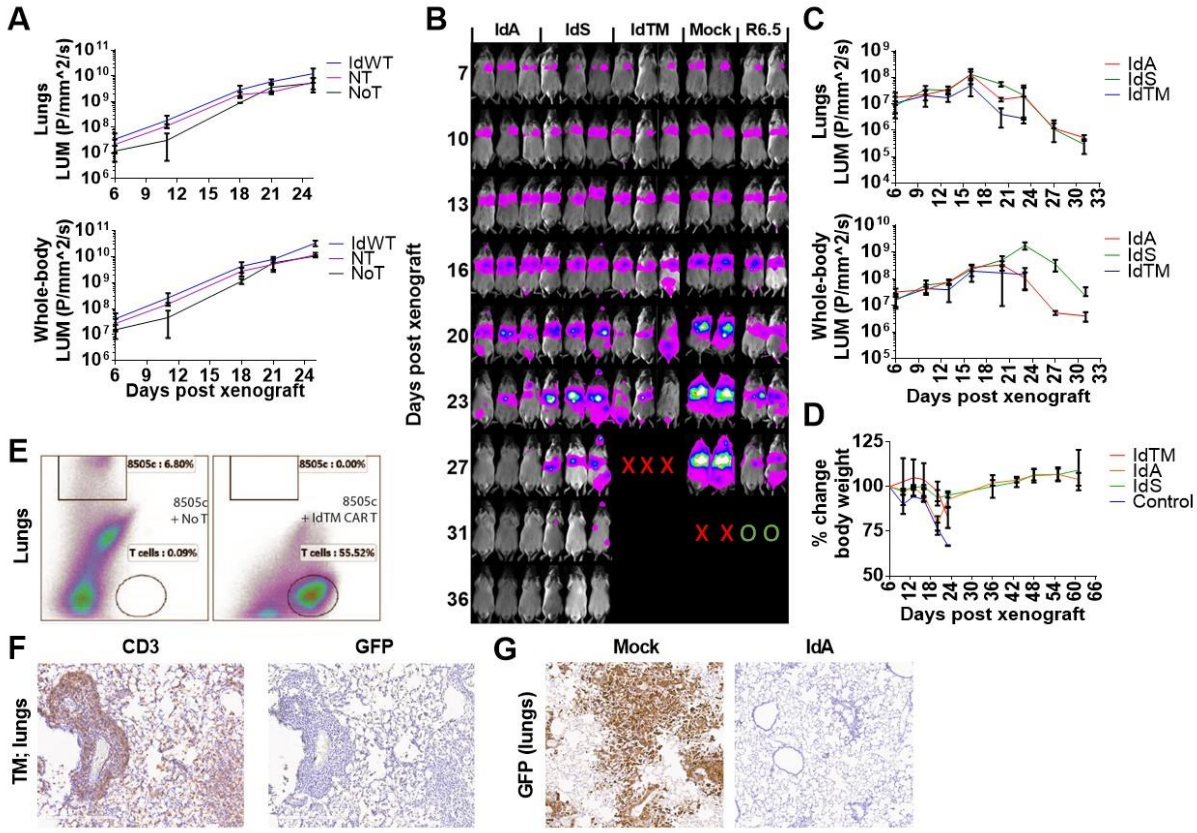

Figure 4.3: Affinity-tuned I domain CAR T cells and regression of advanced tumors in mice. Treatment administered 10 days after systemic 8505c xenotransplantation. Lung and whole-body luminescence of 8505c tumors after treatment with (A) IdWT-CAR T cells, NT cells, NoT cells, (B, C) IdA-CAR T cells, IdS-CAR T cells, IdTM-CAR T cells, mock transduced T cells, and R6.5-CAR T cells. (D) Percent body weight change in mice treated with IdA, IdS, and IdTM-CAR T cells compared to non-transduced T cells (control). (E) FACS and (F, G) histological validation of tumor growth and T cell expansion in the lungs. Red 'X': death, green 'O': imaging discontinued.

mediated by IdTM-CAR T cells cross-reacting with murine ICAM-1 in lung tissue (Fig. 4.3E). Substantial accumulation of IdTM-T cells in lungs was confirmed by histology, which showed T cell localization to tumor lesions as well as wide-spread presence within normal alveoli (Fig. 4.3F).

Despite a slower *in vitro* tumor lysis by IdA and IdS-CAR T cells, they displayed similar rate of tumor eradication as IdTM-CAR T cells *in vivo*. Complete eradication of tumor cells from the lungs as well as the normalization of the alveoli structures were observed in histology (Fig. 4.3G). In addition, no physical signs of systemic or local toxicity was observed in these mice (Fig. 4.3D). IdWT-CAR T cells, on the other hand, failed to induce tumor eradication (Fig. 4.3A). Based on the *in vitro* data, it can be postulated that the rate of killing by IdWT-CAR T cells was too slow to overtake tumor growth rate.

In order to further evaluate the efficacy of the affinity-tuned CAR T cells *in vivo*, a NSG mouse model was designed to harbor subcutaneous 8505c tumors. The tumors were created bilaterally in the lower flanks by injecting 1.5 x 10^6 8505c cells in 150 ul of matrigel. Different I domain CAR T cells (3 x 10^6) were injected when tumor size reached approximately 100 mm^3 and serial bioluminescence imaging and tumor size assessments were conducted.

Unfortunately, the efficacy of CAR T cells was much less drastic (Fig. 4.4). Only sign of tumor reduction was observed 17 days after treatment with IdTM-CAR T cells and as observed with the systemic tumor model, these mice showed severe systemic toxicity. IdA and IdS-CAR T cells, which accomplished near-complete lung tumor eradication previously, were unable to limit the subcutaneous tumor growth.

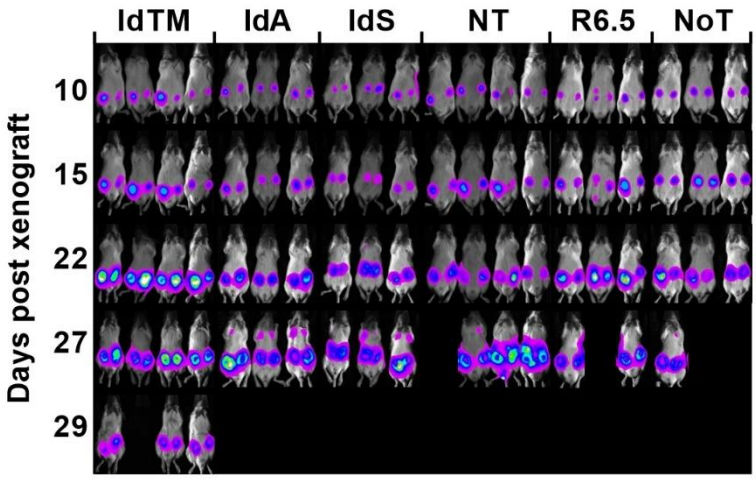

Figure 4.4: Insufficient I domain-CAR T cell efficacy against subcutaneous 8505c xenograft mouse model. Treatment with various CAR T cells administered 10 days after subcutaneous bilateral 8505c xenografts. Whole-body bioluminescence images taken on indicated days post-xenograft.

Discussion

The compelling accomplishment by CAR T cell therapy in blood-borne malignancies is fueling the development of CARs that can overcome the problems inherent in solid tumor landscape. Similar to many other cancer therapies, identifying a target to allow specific elimination of tumor while sparing normal tissue is the top priority. Candidate targets may be mutated or upregulated on tumor cell surfaces, but even trace amounts on normal tissues can lead to serious side effects. The same issue complicates the delicate balance between T cell persistence and safety, since greater persistence often leads to better clinical response as well as increased chance for damage to normal tissues with low levels of target antigen.

Though CARs specific for the B-cell lineage antigens CD19 and CD20 displayed potent efficacy in B-cell malignancies[19], in solid tumors, with the exception of tumor-specific neoantigens such as EGFRviii[20], on-target, off-tumor toxicity is anticipated to be detrimental. Our results demonstrate that CARs with possible on-target, off-tumor toxicities can be engineered to exhibit higher selectivity and reduced toxicity. For example, in our study, the IdTM-CAR caused lethal toxicity in host due to recognition of physiologic levels of ICAM-1 expressed in normal tissues like the lungs. By reducing the affinity of TM I domain down to the physiologically natural affinity (low micromolar K_D), a substantial improvement in the therapeutic index was achieved.

Similar to previously reported studies[11], our results showed that the high-affinity I domain CAR T cells (K_D ranging from 1-100 nM) exhibited little to no discrimination between high and low target antigen density. In addition to the decreased selectivity in target

identification, our high-affinity I domain CAR T cells were strongly reactive to model endothelial cells *in vitro* as well as to all the hosts in aggressive mouse tumor models. However, the IdA-CAR that exhibits “natural” affinity (1-100 uM)[21] displayed higher selectivity by better mimicking the binding half-life of natural TCR/pMHC interaction, which may have aided in improved serial engagement.

The success in systemic 8505c tumor treatment was not extrapolated to the subcutaneous model. Among the many obstacles faced by T cells in efficient infiltration and lysis of solid tumors, hypoxia, low pH, high interstitial pressure, dysregulated blood vessels, and dense collagen networks have been presented as major limitations[22]. We hypothesize that these factors hamper efficient killing of subcutaneous tumors compared to systemic counterparts by CAR T cells. Local administration of TLR agonists in these instances could therefore increase ICAM-1 antigen density but also increase T cell localization and diapedesis through cytokine signaling and stronger chemokine gradients, which can increase therapeutic efficacy with particular regard to the lower affinity CAR T cells.

On-going studies are exploring other strategies to maximize the therapeutic index of CAR T in managing on-target, off-tumor toxicity. Notable endeavors include the inclusion of inhibitory CARs or chimeric co-stimulatory receptors[23, 24], which depend on more than one target antigen to increase specificity. Other strategies include combining suicide genes with the CAR design or transiently expressing CAR molecules using expression systems of mRNA[25-27]. Our work on the affinity-tuning strategy presented here has the potential to improve the therapeutic index of CAR T cell therapy against many of the validated targets previously

considered risky because of on-target, off-tumor toxicities. Developing safer CAR designs would also benefit the potential usage of CAR technology in other diseases, such as autoimmunity.

REFERENCES

1. Kochenderfer, J.N., et al., *Eradication of B-lineage cells and regression of lymphoma in a patient treated with autologous T cells genetically engineered to recognize CD19.* Blood, 2010. **116**(20): p. 4099-102.
2. Porter, D.L., et al., *Chimeric antigen receptor-modified T cells in chronic lymphoid leukemia.* N Engl J Med, 2011. **365**(8): p. 725-33.
3. Grupp, S.A., et al., *Chimeric antigen receptor-modified T cells for acute lymphoid leukemia.* N Engl J Med, 2013. **368**(16): p. 1509-18.
4. Brentjens, R.J., et al., *CD19-targeted T cells rapidly induce molecular remissions in adults with chemotherapy-refractory acute lymphoblastic leukemia.* Science Translational Medicine, 2013. **5**(177): p. 177ra38.
5. Cheever, M.A., et al., *The prioritization of cancer antigens: a national cancer institute pilot project for the acceleration of translational research.* Clin Cancer Res, 2009. **15**(17): p. 5323-37.
6. Kakarla, S. and S. Gottschalk, *CAR T Cells for Solid Tumors Armed and Ready to Go?* Cancer Journal, 2014. **20**(2): p. 151-155.
7. Lamers, C.H., et al., *Treatment of metastatic renal cell carcinoma with autologous T-lymphocytes genetically retargeted against carbonic anhydrase IX: first clinical experience.* Journal of Clinical Oncology, 2006. **24**(13): p. e20-2.
8. Parkhurst, M.R., et al., *T Cells Targeting Carcinoembryonic Antigen Can Mediate Regression of Metastatic Colorectal Cancer but Induce Severe Transient Colitis.* Molecular Therapy, 2011. **19**(3): p. 620-626.
9. Morgan, R.A., et al., *Case Report of a Serious Adverse Event Following the Administration of T Cells Transduced With a Chimeric Antigen Receptor Recognizing ERBB2.* Molecular Therapy, 2010. **18**(4): p. 843-851.
10. Hudecek, M., et al., *Receptor Affinity and Extracellular Domain Modifications Affect Tumor Recognition by ROR1-Specific Chimeric Antigen Receptor T Cells.* Clinical Cancer Research, 2013. **19**(12): p. 3153-3164.
11. Chmielewski, M., et al., *T cell activation by antibody-like immunoreceptors: Increase in affinity of the single-chain fragment domain above threshold does not increase T cell activation against antigen-positive target cells but decreases selectivity.* Journal of Immunology, 2004. **173**(12): p. 7647-7653.
12. Schmid, D.A., et al., *Evidence for a TCR affinity threshold delimiting maximal CD8 T cell function.* J Immunol, 2010. **184**(9): p. 4936-46.
13. Jin, M., et al., *Directed evolution to probe protein allostery and integrin I domains of 200,000-fold higher affinity.* Proc Natl Acad Sci U S A, 2006. **103**(15): p. 5758-63.
14. Wong, R., et al., *Visualizing and Quantifying Acute Inflammation Using ICAM-1 Specific Nanoparticles and MRI Quantitative Susceptibility Mapping.* Annals of Biomedical Engineering, 2012. **40**(6): p. 1328-1338.
15. Carpenito, C., et al., *Control of large, established tumor xenografts with genetically retargeted human T cells containing CD28 and CD137 domains.* Proc Natl Acad Sci U S A, 2009. **106**(9): p. 3360-5.

16. Hofig, I., et al., *Poloxamer synperonic F108 improves cellular transduction with lentiviral vectors.* J Gene Med, 2012. **14**(8): p. 549-60.
17. Leelawattanachai, J., et al., *Side-by-Side Comparison of Commonly Used Biomolecules That Differ in Size and Affinity on Tumor Uptake and Internalization.* Plos One, 2015. **10**(4).
18. Zhang, L., et al., *An in vivo mouse model of metastatic human thyroid cancer.* Thyroid, 2014. **24**(4): p. 695-704.
19. Maus, M.V., et al., *Antibody-modified T cells: CARs take the front seat for hematologic malignancies.* Blood, 2014. **123**(17): p. 2625-35.
20. Morgan, R.A., et al., *Recognition of glioma stem cells by genetically modified T cells targeting EGFRvIII and development of adoptive cell therapy for glioma.* Hum Gene Ther, 2012. **23**(10): p. 1043-53.
21. Liu, X.J., et al., *Affinity-Tuned ErbB2 or EGFR Chimeric Antigen Receptor T Cells Exhibit an Increased Therapeutic Index against Tumors in Mice.* Cancer Research, 2015. **75**(17): p. 3596-3607.
22. Newick, K., E. Moon, and S.M. Albelda, *Chimeric antigen receptor T-cell therapy for solid tumors.* Mol Ther Oncolytics, 2016. **3**: p. 16006.
23. Kloss, C.C., et al., *Combinatorial antigen recognition with balanced signaling promotes selective tumor eradication by engineered T cells.* Nat Biotechnol, 2013. **31**(1): p. 71-5.
24. Lanitis, E., et al., *Chimeric Antigen Receptor T Cells with Dissociated Signaling Domains Exhibit Focused Antitumor Activity with Reduced Potential for Toxicity In Vivo.* Cancer Immunology Research, 2013. **1**(1): p. 43-53.
25. Di Stasi, A., et al., *Inducible Apoptosis as a Safety Switch for Adoptive Cell Therapy.* New England Journal of Medicine, 2011. **365**(18): p. 1673-1683.
26. Wang, X., et al., *A transgene-encoded cell surface polypeptide for selection, in vivo tracking, and ablation of engineered cells.* Blood, 2011. **118**(5): p. 1255-63.
27. Beatty, G.L., et al., *Mesothelin-specific chimeric antigen receptor mRNA-engineered T cells induce anti-tumor activity in solid malignancies.* Cancer Immunology Research, 2014. **2**(2): p. 112-20.

CHAPTER 5

CONCLUSIONS AND FUTURE DIRECTIONS

Sequencing of the human genome has classified 18 alpha and 8 beta subunits of integrins, resulting in 24 currently identified functional integrins in humans. These numerous integrins mediate stable adhesion to basement membranes, the formation of and migration on extracellular matrices, the formation of platelet aggregates, the establishment of intercellular junctions in the immune system, and bacterial and viral entry during infectious diseases. Integrin-mediated adhesions, especially, modulates signaling cascades in control of cell motility, survival, proliferation, and differentiation.

In this dissertation, I have demonstrated various applications of such interactions involving a leukocyte integrin, LFA-1, for development of therapeutics. One of the major breakthroughs that allowed for my thesis work was the directed evolution engineering of the α_L I domain to various affinity states that ranges six orders of magnitude. The specificity and affinity of the I domain mutants to their native ligand, ICAM-1, provide ways to specifically target therapeutics to many human carcinomas and the associated inflammation therein. I demonstrated affinity-dependent targeted delivery of anti-tumor drug compounds as well as plasmids, using the engineered LFA-1 I domains. From these studies I have confirmed the presence of inflammation in the tumor stroma and demonstrated the possibility of targeting an inflammation marker, such as ICAM-1, in delivery of therapeutics targeting even tumors that lack the expression of unique tumor antigens.

Combining therapy and diagnostics in one dose is a novel idea that will be a key part of advancing predictive medicine. This approach allows real-time tracing of the drug-carriers, while also tracking the progress of the tumor growth/suppression. I have shown here the ability of the UAN platform to encapsulate high concentrations of various different payloads simultaneously. Incorporating Zr-89 into drug-carriers would bestow theranostic capabilities, allowing concurrent chemotherapy and tumor tracing using PET imaging. Such method will facilitate gaining real-time information about the trafficking pathway, kinetics of delivery, and therapeutic efficacy. Combining therapeutic and diagnostic capabilities in this fashion has potential for effective personalized medicine.

One of my major goals in developing targeted therapy has been to establish a system that can initiate on-target, on-tumor potency while minimizing off-tumor toxicities. Many years of engineering and optimizations have led to better understanding for safer drug delivery vehicles. Necessary qualifications include longer circulation time using blood proteins or molecules like PEG, slow or controlled release of payloads for non-promiscuous uptake by cells, optimal range of size to take advantage of the EPR effect, and surface characteristics to minimize uptake by phagocytic cells. Our studies utilized such safety mechanisms to counteract the possible problems that arising from targeting a protein that is widely expressed in healthy tissues. Ultimately, the transient presence of our drug-carriers in hosts has led to insignificant increase in systemic toxicity.

However, in the field of targeted immunotherapy, especially those utilizing the CAR-T technology, this achievement has been more elusive. Once engineered T cells encounter the target antigen with sufficient avidity and affinity, they become activated, proliferate, and

secrete toxic substances to lyse cells presenting the target antigen. We observed that their ability to kill serially, proliferate, and persist triggers a chronic response leading to host fatalities if the target recognition becomes sensitive enough to react against physiologic levels of target density. As described in Chapter 4, the strategy to fine tune the affinity of LFA-1 I domain has allowed us to identify a variant that can endow much improved therapeutic index against a target antigen that was previously considered too risky due to the prevalence in healthy tissues. I envision that such methods for safe immunotherapy will become the major tool for development of targeted immunotherapy technologies against debilitating diseases, and will greatly aid the translation into the clinic.

APPENDIX A

VIRUS-MIMETIC POLYPLEX PARTICLES FOR SYSTEMIC AND INFLAMMATION-SPECIFIC TARGETED DELIVERY OF LARGE GENETIC CONTENTS

This chapter was originally published in Gene Therapy (Kang, S., Lu, K., Leelawattanachai, J., Hu, X., Park, S., Park, T., Min, I.M., Jin, M.M. *Gene Therapy*. 2013;20(11):1042-52.), and is reprinted with permission. Park S contributed to the validation of virus-mimetic particles *in vitro*. This included the experiments related to Figures 4, 7, and 10.

Summary

Systemic and target-specific delivery of large genetic contents has been difficult to achieve. Although viruses effortlessly deliver kilobase-long genome into cells, its clinical use has been hindered by serious safety concerns and the mismatch between native tropisms and desired targets. Nonviral vectors, in contrast, are limited by low gene transfer efficiency and inherent cytotoxicity. Here we devised virus-mimetic polyplex particles (VMPs) based on electrostatic self-assembly among polyanionic peptide (PAP), cationic polymer polyethyleneimine (PEI) and nucleic acids. We fused PAP to the engineered ligand-binding domain of integrin $\alpha_L\beta_2$ to target intercellular adhesion molecule-1 (ICAM-1), an inducible marker of inflammation. Fully assembled VMPs packaged large genetic contents, bound specifically to target molecules, elicited receptor-mediated endocytosis and escaped endosomal pathway, resembling intracellular delivery processes of viruses. Unlike conventional PEI-mediated transfection, molecular interaction-dependent gene delivery of VMPs was

unaffected by the presence of serum and achieved higher efficiency without toxicity. By targeting overexpressed ICAM-1, VMPs delivered genes specifically to inflamed endothelial cells and macrophages both *in vitro* and *in vivo*. Simplicity and versatility of the platform and inflammation-specific delivery may open up opportunities for multifaceted gene therapy that can be translated into the clinic and treat a broad range of debilitating immune and inflammatory diseases.

Introduction

Viruses have evolved ways to efficiently deliver their genetic materials into cells that can be as large as multiples of kilobase-long nucleic acids. The use of viral gene delivery vectors for clinical applications[1-5] however, poses serious safety issues, including pathogenicity by insertional mutagenesis[6] and anaphylactic response to the virus[7, 8]. On the other hand, synthetic nonviral vectors suffer from inherent cytotoxicity and are severely limited due to low gene transfer efficiency in systemic parenteral applications. Particularly, cationic nonviral vectors, which can disrupt the integrity of plasma membrane during entry into cells[9, 10], are easily inactivated by negatively charged molecules such as glycosaminoglycans in circulation[11-13].

To achieve cell type- or cell state-specific targeted systemic delivery, it often requires the use of complex molecules such as antibodies and proteins that specifically bind to target molecules.

However, systemic site-directed delivery of large nucleic acid molecules has met limited success. In fact, studies have been mostly constrained to the delivery of small nucleic acids, such as siRNA[14-17]. Although viruses possess the ability to overcome many barriers of gene delivery such as cell entry through the membrane and escape from lysosomal nuclease degradation, engineering the tropism of viral vectors for site-directed delivery to a range of different targets[18-20] has been challenging. Nonviral vectors are capable of delivering large content of nucleic acids such as plasmids, but modifications to confer specific targeting have been mostly confined within chemical/covalent attachments of small molecules[21], peptides[22] and several types of proteins[23, 24], which would inevitably affect the original physicochemical properties of the vectors.

In this study, we devised a polyanionic peptide (PAP) comprised of 18 randomly ordered glutamic and aspartic acids that can be expressed as a fusion to proteins to mediate electrostatic attachment to cationic transfection agents. Polyethyleneimine (PEI) was used as a scaffold to hold both a large content of nucleic acid and PAP-fused targeting moieties. PEI has been extensively studied as a cationic polymer-mediated gene delivery agent and has been considered to have relatively high gene transfer efficiency[25-29] PEI has all primary, secondary and tertiary amines, providing buffering capacity at low pH of late endosomes[30]. This promotes an influx of counter-ions such as chloride[31], raising osmotic pressure that eventually bursts the vesicles and releases nucleic acid payload, which has been termed as the proton sponge effect[32].

To achieve targeted gene delivery to inflammatory diseases, we fused the PAP to the major ligand-binding domain (I domain) of integrin lymphocyte function-associated antigen-1

(LFA-1; $\alpha_L\beta_2$) as a targeting moiety. The physiological counter receptor for LFA-1 is the intercellular adhesion molecule-1 (ICAM-1), which is highly expressed on inflamed cell surfaces[33, 34] that often colocalizes at various disease sites[35]. ICAM-1 is also subverted as a receptor for the major human rhinoviruses (HRVs)[36], which gain cell entry by multivalent interaction with ICAM-1 that promotes rapid endocytosis[37, 38]. We have previously engineered the I domain into a high-affinity (HA) mutant to ICAM-1 by directed evolution[39]. The I domain is a globular Rossmann fold protein of approximately the size of a single-chain variable-fragment antibody. We previously used the HA I domain as a targeting moiety for various types of carriers to deliver drugs[40, 41] and imaging contrast agents[42] specifically to inflamed endothelial cells and immune cells, and to cancer cells and their stroma.

Here we show that, by fusing the PAP to the I domain (PAP-Id) and using a cationic nonviral vector PEI, we were able to establish a molecular interaction-dependent gene delivery platform based on their stepwise electrostatic self-assembly, which creates virus-mimetic polyplex particles (VMPs) that mimic the processes involved in virus infection. Similarly as to how cell entry is gained by HRVs, our VMPs were also able to mediate cellular endocytosis by clustering ICAM-1 via multivalent binding of the I domains. Because the attachment of targeting moieties is a self-assembling process, we were able to precisely control the moiety density or avidity, optimal for efficient endocytosis and gene transfer. Not only did the association of DNA and PEI particles with PAP-Id reduce the inherent cytotoxicity of PEI, it also enabled the delivery to be unaffected by the presence of serum. Similarly as acid-catalyzed conformational change in HRV capsid leads to penetration of the membrane, VMPs escaped endosomal degradation and

led to efficient gene expression. Moreover, by targeting ICAM-1, we were able to deliver genes specifically to inflamed endothelial cells and immune cells both *in vitro* and systemically *in vivo*.

Experimental Procedures

Cell culture conditions

HeLa, bEnd.3, RAW 264.7 (ATCC, Manassas, VA, USA) and primary mouse lung cells were cultured in Advanced Dulbecco's modified Eagle's medium (Invitrogen, Carlsbad, CA, USA) containing 2 mM L-glutamine, Pen-step (100 units/ml penicillin and 100 μg/ml streptomycin) and 10% fetal bovine serum (FBS; endotoxin free, PAA Laboratories, Piscataway, NJ, USA). Primary mouse lung cells were harvested from fetus lungs of mouse strain Gt(ROSA)26Sor$^{tm4(ACTB\text{-}tdTomato,\text{-}EGFP)Luo}$(Jackson Laboratory, Bar Harbor, ME, USA). Lungs were aseptically minced and digested in 1 mg/ml collagenase A (Roche, Basel, Germany) for 3 h at 37 °C, which were then filtered through 70-μm nylon mesh cell strainer and washed twice in complete media for culture. HMEC-1 (Center for Disease Control, Atlanta, GA, USA) was propagated in MCDB 131 medium (Invitrogen) supplemented with 10% FBS, 10 mM L-glutamine, Pen-strep, 1 μg/ml hydrocortisone (MP Biomedicals, Solon, OH, USA) and 10 ng ml^{-1} human epidermal growth factor (Invitrogen). THP-1 cells (ATCC) were cultured in RPMI 1640 medium (Invitrogen) with 10% FBS and Pen-strep. Endothelial cells and primary mouse lung cells were trypsinized at confluency and washed to remove residual trypsin before plating. All mammalian cells were maintained at 37 °C in a 5% CO_2 humidified incubator.

Protein construction, design, and purification

Wild-type LFA-1 I domain sequence (Asn-129 to Tyr-307) followed by a stop codon was subcloned into pET28a vector (Novagen, Madison, WI, USA) between BamH1 and Xho1. QuickChange (Stratagene, La Jolla, CA, USA) site-directed mutagenesis was used to create F265S/F292G and D137A mutants. For GFP-Id, a superfolder GFP[43] was inserted between Nhe1 and BamH1. To construct PAP-Id, complementary primers encoding 5′-ctagcgaggatgaagatgaggaagacgaagaagatgaagaggacgaagaggacgaggatg-3′ and 5′-gatccatcctcgtcctcttcgtcctcttcatcttcttcgtcttcctcatcttcatcctcg-3′ were annealed and directly ligated between Nhe1 and BamH1. Constructs were transformed into *Escherichia coli*, BL21 (DE3) cells (Novagen) for production of the fusion proteins. Overnight starter culture was used to inoculate a larger Luria Bertani medium at 1:40 volume ratio and was grown at 37 °C to OD600 of 0.4–0.5 (~2 h). Then cells were induced with freshly prepared 1 mM isopropyl-*β*-D-thiogalactopyranoside at 25 °C overnight (~15 h). Cells were recovered by centrifugation and sonicated in buffer A (50 mM NaH_2PO_4, 300 mM NaCl, 10 mM imidazole, protease inhibitor cocktail (ProteCEASE-EDTA free, G-Biosciences, St. Louis, MO, USA)) with pH adjusted to 8.0 for GFP-Id and 6.0 for PAP-Id. Soluble fraction of GFP-Id was purified by passage over a Ni-NTA column (Pierce, Rockford, IL, USA). Insoluble fraction of PAP-Id was washed in buffer A with four cycles of sonication and super-centrifugation at 20 000 *g* for 30 min. Protein pellet was then solubilized in buffer B (buffer A plus 6 M guanidine HCl, pH 8.0) and purified by Ni-NTA. GFP-Id and PAP-Id were washed in buffer C (50 mM NaH_2PO_4, 300 mM NaCl, 20 mM imidazole, pH 8.0) and then eluted in buffer D (50 mM NaH_2PO_4, 300 mM NaCl, 250 mM imidazole, pH 8.0).

Eluted proteins were then subjected to gel filtration chromatography using Superdex S200 column in phosphate-buffered saline (PBS) connected to AKTA Purifier (GE Healthcare, Pittsburgh, PA, USA).

Electrostatic self-assembly of VMPs

For any given mass ratios, plasmid and PEI (branched, M_W 25 000, Sigma-Aldrich, St. Louis, MO, USA) were each diluted in one volume of PBS (pH 7.4) and PAP-Id in two volumes of PBS. Solutions containing plasmid and PEI were first vortex mixed and incubated at room temperature for 40 min. Plasmid/PEI mixture was then gently mixed with PAP-Id solution and incubated at room temperature for 40 min. Vector for GFP expression (pGFP) was constructed by subcloning a complete Kozak consensus sequence and enhanced GFP sequence followed by a stop codon between EcoRI and BglII of pAAV-MCS vector (AAV Helper-Free System, Agilent Technologies, Santa Clara, CA, USA). Vectors for expression of diphtheria toxin A (pDTA) and Cre recombinase (pCRE) were obtained from Addgene (Cambridge, MA, USA), originally named as PGK-DTA-bpA[44] (plasmid 13440) and pLOX-CW-CRE[45] (plasmid 12238), respectively. All components used for assembly of VMPs, including plasmids, PAP-Id, PEI and PBS, were filter sterilized through 0.2-μm centrifugal or syringe filters before assembly.

Dynamic light scattering and zeta-potential measurements of VMPs

The size distribution and zeta-potential of VMPs were determined using Zetasizer Nano ZS (Malvern Instruments (Malvern, Worcestershire, UK)). VMPs prepared with 1 μg of plasmid

and the relative mass of PEI and/or PAP-Id were each diluted in 750 µl of PBS (pH 7.4). The solution was added to the cell and the measurements were carried out at 25 °C.

In vitro delivery of VMPs

Cells were grown in 24-well plates to confluence and pretreated with complete media containing 1 µg/ml of LPS (*E. coli*, 026:B6, Sigma) to induce inflammation. Each well received VMPs prepared with 0.4 µg of plasmid and the relative mass and volumes of PEI and PAP-Id. Final VMPs were then mixed with an equal volume of FBS and incubated at room temperature for 40 min before delivery to cells. After delivery, cells were washed twice with media, followed by addition of fresh complete media.

In vivo delivery of polyplex particles

Eight-to-ten-week-old female BALB/c mice (Jackson Laboratory) were used. All administrations performed in this study were given intravenously, using 29G × 0.5'' insulin syringes via lateral tail vein route injections. To induce systemic inflammation, 20 µg per mouse of LPS (*E. coli*, 026:B6, Sigma) in PBS (pH 7.4) was injected. VMPs bearing 5 µg of plasmid was formed in a mass ratio of the components (plasmid:PEI:PAP-Id) fixed to 1:6:16 in a final volume of 200 µl. All animal procedures were approved by the Cornell University IACUC and were conducted in accordance with recommendations in the Guide for the Care and Use of Laboratory Animals published by the National Institutes of Health.

Immunofluorescence for imaging and flow cytometric analysis

Mean fluorescence intensity and percentage of GFP-positive cells were quantified by flow cytometry (Beckman Coulter EPICS XL-MC, Brea, CA, USA). After *in vitro* delivery of VMPs for GFP expression, cells were trypsinized, washed with washing buffer (PBS, 0.5% bovine serum albumin, pH 7.4) and subjected to flow cytometer. Total fluorescence was quantified by lysing cells with 1% (v/v) Triton X-100 in PBS and measuring with a fluorescence plate reader Infinite M1000, TECAN (Männedorf, Switzerland). Confocal microscopy (Zeiss LSM 710, Zeiss (Oberkochen, Germany)) was used to assess endocytosis of VMPs and protein expression in HeLa cells. PAP-Id was conjugated to Alexa Fluor 555 (succinimidyl ester, Invitrogen) and pGFP was labeled with Cy5 (Label IT Nucleic Acid Labeling Kit, Mirus Bio (Madison, WI, USA)). HeLa cells were grown in 35 mm glass bottom dishes (0.16–0.19 mm cover glass, In Vitro Scientific (San Jose, CA, USA)) and fixed in 3.7% formaldehyde for 1 h at different time points after delivery of fluorescently labeled VMPs. Expression of ICAM-1 in mouse lungs were assessed by GFP-Id. Lungs were collected at different time points after systemic LPS treatment (20 μg per mouse, *E. coli*, 026:B6, Sigma) and were minced and digested in 1 mg ml^{-1} collagenase A (Roche) for 3 h at 37 °C. Singlet lung cells were prepared by passage through 70-μm nylon mesh cell strainer and incubation with red blood cell lysis buffer (eBiosciences, San Diego, CA, USA) for 5 min on ice. Cells were then washed and labeled for ICAM-1 with 10 μg/ml GFP-Id in ice-cold labeling buffer (PBS, 0.5% bovine serum albumin, 10 mM $MgCl_2$, pH 7.4) for 1 h. Cells were then labeled with either rat IgG anti-mouse CD31 (1:20, BD Pharmingen, San Diego, CA, USA) or rat IgG anti-mouse F4/80 (1:50, Abcam, Cambridge, UK) for 1 h, followed by goat anti-rat IgG-PE

(Santa Cruz, Santa Cruz, CA, USA) as secondary antibody for 1 h. For detection of GFP expression after delivery of VMPs bearing pGFP, singlet lung cells were fixed with 3.7% formaldehyde for 1 h and permeabilized with 1% (v/v) Triton X-100 for 30 min. Permeabilized cells were then labeled with rabbit IgG anti-GFP antibody (1:20, Invitrogen) for 1 h, followed by goat anti-rabbit IgG-PE (1:100, Santa Cruz) for 1 h. Cells were then labeled for CD31 and F4/80 similarly as described, followed by goat anti-rat IgG-FITC (1:100, Santa Cruz) for 1 h.

Real-time quantitative PCR

Total RNAs from harvested lungs were extracted using TRI Reagent (Ambion, Austin, TX, USA). Briefly, mouse lung tissue (~150 mg) was homogenized in 1 ml of TRI Reagent solution followed by brief sonication. Homogenized lysates were mixed with 200 µl chloroform and centrifuged at 12 000 *g* for 15 min. In all, 400 µl of colorless upper aqueous phase was collected and mixed with 500 µl isopropanol and loaded to spin columns (Zymo-Spin II, Zymo Research, Irvine, CA, USA). Eluted RNA (1 µg) was converted to cDNA using a reverse transcription kit (High Capacity cDNA RT kits, Applied Biosystems, Foster City, CA, USA) in a thermal cycler (GeneAmp PCR System 2700, Applied Biosystems). Real-time gene amplification analysis (MyiQ iCycler, Bio-Rad) was performed using a quantitative PCR kit (Sybr Green 2 × Master Mix, Bio-Rad, Hercules, CA, USA) to measure gene expression of GFP relative to CYC1 housekeeping gene. Primers for GFP were previously reported[46] and for CYC1 (NM_025567) were obtained from Mouse qPrimerDepot of the National Cancer Institute.

Quantification of cell viability

Cell viability of HeLa cells treated with VMPs bearing pDTA was analyzed by trypan blue exclusion test. Cells were incubated with 0.2% trypan blue for 5 min, and microscopic images were taken at random places of culture wells. Viable cells that excluded trypan blue and nonviable cells with blue cytoplasm were counted per given image field for analysis. Viability measurements presented in Figures 3, 4, 5 were quantified by MTT (3-(4,5-dimethylthiazol-2-yl)-2,5-diphenyltetrazolium bromide) assay. Cells were incubated with basal media containing 0.5 mg/ml MTT for 4 h at 37 °C. Blue formazan products were solubilized in dimethyl sulfoxide and quantified by absorbance at 570 nm.

Statistical analysis

Data were expressed as mean ± s.d. of at least quadruplicate samples. Statistical analysis of data was carried out using GraphPad Prism 5; GraphPad Software Inc. (La Jolla, CA, USA). Unpaired Student's *t*-test was used to determine statistical significance in comparison to matching controls. One-way analysis of variance was used to compare mean responses among the different groups, followed by Tukey's *post-hoc* test to determine statistical significance.

Results

Molecular interaction-specific VMPs for targeted gene delivery

VMPs were designed to mimic the components of non-enveloped viruses (for example, HRVs) and their entry into a specific range of host cells (Fig. A1a). VMPs were assembled in a sequential manner: first PEI and DNA plasmids were mixed together, to which proteins were added. The ratio of protein, DNA, and PEI was adjusted so that unsaturated positive charges in PEI would assemble with the negatively charged residues (PAP) and DNA (Fig. A1b). When added to cells with ICAM-1 expression, VMPs that were assembled with integrin LFA-1 I domain would cluster ICAM-1 and trigger the cells for endocytosis. A decrease in pH in late endosomes would increase the degree of protonation in PEI, whereby it attracts counter-ions and bursts the vesicle by proton sponge effect[31, 32]. Escaped plasmid payloads are then transported into the nucleus and leads to the expression of encoding genes.

To visualize VMPs throughout the processes of cell entry, endosomal escape and gene expression, we fluorescently labeled plasmids and PAP-Id to track the particles by confocal microscopy. We used the I domain engineered for HA with double mutations F265S/F292G[39] (denoted as PAP-Id(HA)). We used a plasmid encoding enhanced green fluorescent protein (GFP) under cytomegalovirus promoter (denoted as pGFP). VMPs were constructed using Cy5-labeled pGFP and Alexa Fluor 555-conjugated PAP-Id(HA) at a mass ratio determined to be within an optimal range for delivery (1:6:16 for pGFP:PEI:PAP-Id(HA); see Fig. A2). We then delivered the fluorescently labeled VMPs in the presence of serum to HeLa cells, which express a high level of ICAM-1. Cells were fixed at 3, 24 and 48 h after delivery. At 3 h post delivery, VMPs were found mostly inside cells, confirmed by confocal microscopy (Fig A1c,

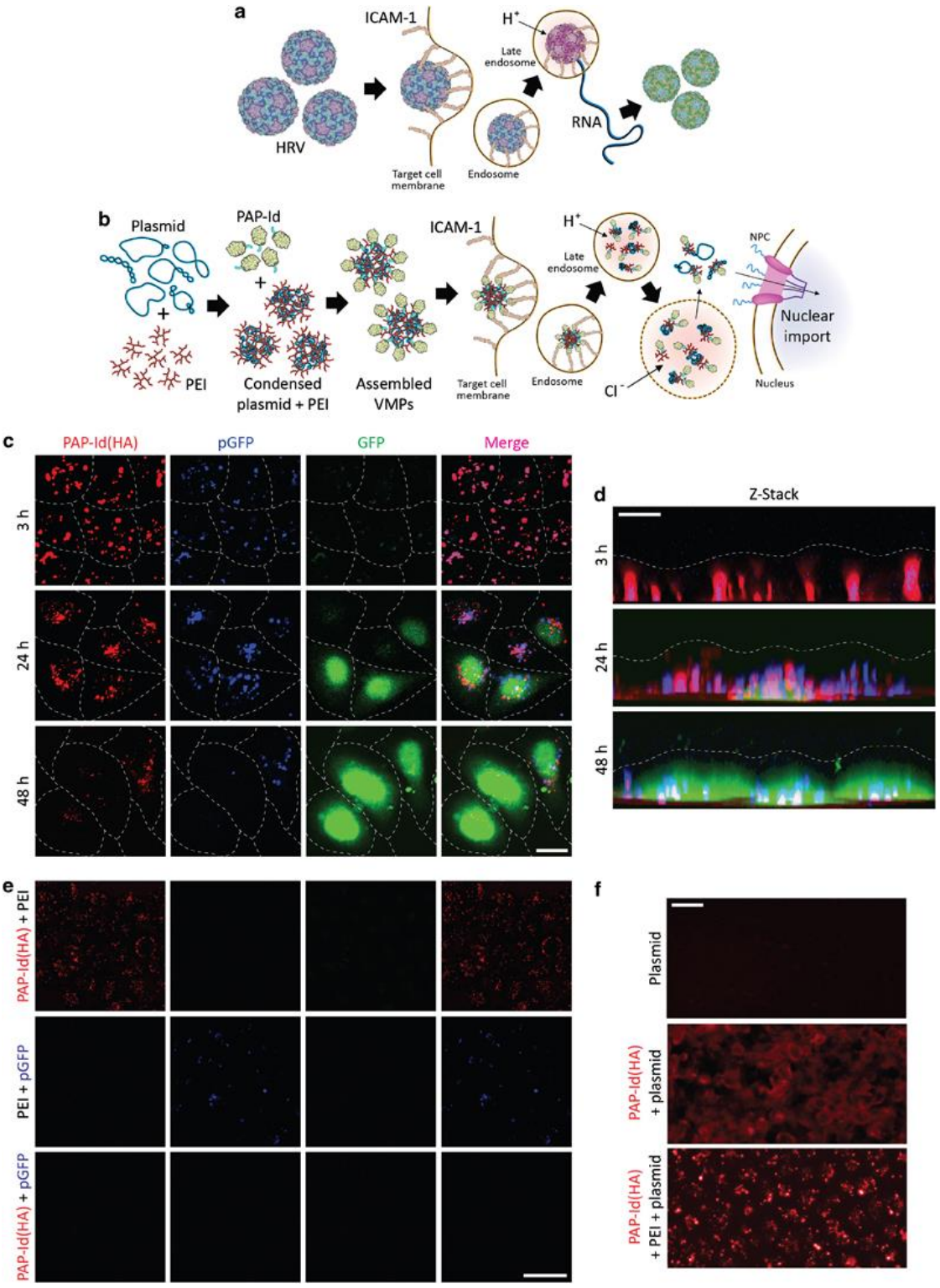
a
ICAM-1
H+
Late endosome
HRV
RNA
Target cell membrane
Endosome
b
Plasmid
PAP-Id
PEI
Condensed plasmid + PEI
Assembled VMPs
ICAM-1
H+
Late endosome
NPC
Nuclear import
Target cell membrane
Endosome
Cl -
Nucleus
c
PAP-Id(HA)
pGFP
GFP
Merge
3 h
24 h
48 h
d
Z-Stack
3 h
24 h
48 h
e
PAP-Id(HA) + PEI
PEI + pGFP
PAP-Id(HA) + pGFP
f
Plasmid
PAP-Id(HA) + plasmid
PAP-Id(HA) + PEI + plasmid

Figure A1: Cell entry, endosomal escape and gene expression of polyplex particles. (a) HRV gains cell entry by binding and clustering ICAM-1, which is overexpressed on inflamed cell surfaces. Acid-catalyzed conformational change in the viral capsid (violet) penetrates the membrane of late endosomes, through which it releases the RNA genome that leads to the synthesis of more viruses (green). (b) Self-assembly of VMPs is mediated by stepwise electrostatic interactions among negatively charged nucleic acids, positively charged PEI and PAP-Id. VMPs similarly gain cell entry by multivalent ICAM-1 clustering-mediated endocytosis. A decrease in pH in late endosomes protonates PEI, attracting counterions (Cl^-) and exerting osmotic pressure and eventually bursting the vesicle. Plasmid payloads that escaped endosomal nuclease degradation are then transported into the nucleus through the nuclear pore complex (NPC), leading to the expression of encoding genes. (c–e) Confocal microscopy was used to track intracellular localization of PAP-Id(HA) (high affinity) conjugated to Alexa Fluor 555 (red), pGFP labeled with Cy5 (blue) and GFP expression (green) in HeLa cells. (c) VMPs were self-assembled at its optimal mass ratio of pGFP:PEI:PAP-Id(HA) adjusted to 1:6:16. Cells received VMPs in the presence of serum, which then were fixed at time points of 3, 24 and 48 h after delivery. Colocalization of red and blue appears in magenta in merged image. Focal plane was set through the middle of cells to capture VMPs inside cells. Dotted lines mark the cell boundaries. Bar = 20 μm. (d) Z-stack confocal images also show localization of VMPs inside HeLa cells at 3, 24 and 48 h after delivery. Dotted lines indicate the top surface of cells. Bar = 10 μm. (e) Similarly, confocal images were taken at 3 h post delivery to assess the uptake of control particles (formed with PEI and PAP-Id(HA), PAP-Id(HA) and pGFP or PEI and pGFP). Note that focal plane for imaging was set through the middle of cells to visualize only the particles internalized into cells. Bar = 50 μm. (f) Fluorescence microscope images (top view) of HeLa cells at 3 h post delivery are shown (imaged without fixation). PAP-Id(HA), conjugated to Alexa Fluor 555 for fluorescent detection, was either assembled with only plasmid or with PEI and plasmid. The particles were incubated with HeLa cells in the presence of serum. Bar = 50 μm.

d). PAP-Id(HA) (red) and pGFP (blue) appeared to be in complex with each other, evidenced by colocalization of the two in the merged image. At 24 h post delivery, some cells began to express GFP, which coincided with the observation that the components of VMPs appeared to be dissociated from each other. At 48 h, most cells expressed GFP, while much of the components of VMPs were no longer detectable. PEI/DNA plasmids polyplex without the I domain (PEI:pGFP=6:1 w/w) exhibited a size of 169 nm and a zeta potential of +26 mV. With the addition of the I domain (PEI:eGFP:I domain=6:1:12), VMPs increased in size (245.5 nm) but displayed a reduced zeta potential (+20 mV), presumably due to the presence of negatively charged peptides (PAP) fused to the I domains.

To show that all three components are necessary for gene delivery by VMPs, we assembled fluorescently labeled particles with one component omitted (that is, PAP-Id(HA)/PEI, PEI/pGFP and PAP-Id(HA)/pGFP) and delivered to HeLa cells in the presence of serum (Fig. A1e). At 3 h post-delivery, the particles that were formed without pGFP (that is, PAP-Id(HA)/PEI) were found as small vesicles inside the cells but to a lesser extent than fully assembled VMPs. Particles that were assembled without PAP-Id(HA) (that is, PEI/pGFP) were sparsely found inside the cells. The mixture without PEI (that is, PAP-Id(HA)/pGFP), where PAP-Id(HA) would not associate with pGFP and remain as monomers, were not found inside the cells (Fig. A1e). In order to show that clustering of ICAM-1 is necessary for internalization of particles by the cells, we imaged cells without fixation under conventional fluorescence microscopy (Fig. A1f). The mixture of PAP-Id(HA)/plasmid was indeed smoothly distributed over the cell surfaces, which was in contrast to fully assembled VMPs appearing as endocytosed intracellular speckles (Fig. A1f). As a negative control for the HA I domain, we used the PAP-fused I domain containing a

loss-of-function mutation D137A[47] (denoted as PAP-Id(D137A)). Particles that were assembled with Id(D137A) were neither observed on the cell surface nor inside the cells, proving that it is ICAM-1-mediated internalization by which our VMPs were delivered inside the cells (images and functional data shown throughout Fig. 2, 3, 4, 5, 6).

Determining optimal ratios of protein, DNA and PEI for efficient gene delivery

In an effort to assemble VMPs for the highest gene transfer efficiency, we varied the mass ratios of individual components and examined the efficiency of gene expression (Figure 2). With a fixed amount of pGFP, we varied the amount of PEI ranging from 3 to 8 mass ratios of PEI to plasmids. To the mixture of pGFP/PEI particles, PAP-Id(HA) or PAP-Id(D137A) were added at mass ratios varying from 2 to 32 of proteins to plasmids (Fig. A2a). Assembled VMPs were delivered to HeLa cells in the presence of serum. As additional controls and for comparison to conventional transfection methods, pGFP/PEI particles were used without proteins, both with or without serum (Fig. A2a). Gene transfer efficiency was assessed by two different assays, that is, total fluorescence measured from cell lysates, and mean fluorescence intensity and the percentage of GFP-positive cells measured by flow cytometry. Overall, VMPs formulated with the mass ratios of 8–16-fold excess of PAP-Id(HA) and 5–7-fold excess of PEI over pGFP led to the highest readouts of total fluorescence and a percentage of GFP-positive cells (Figure 2a). Higher than optimal ratios of I domains mixed with pGFP/PEI resulted in a decrease in delivery efficiency due to the inhibition of VMP binding to cells by free I domains occupying available ICAM-1 on cell surface. Although VMPs assembled with PAP-Id(HA) produced over 80% GFP-positive cells and total fluorescence as high as 20-fold over the mixture of PAP-Id(HA)/pGFP,

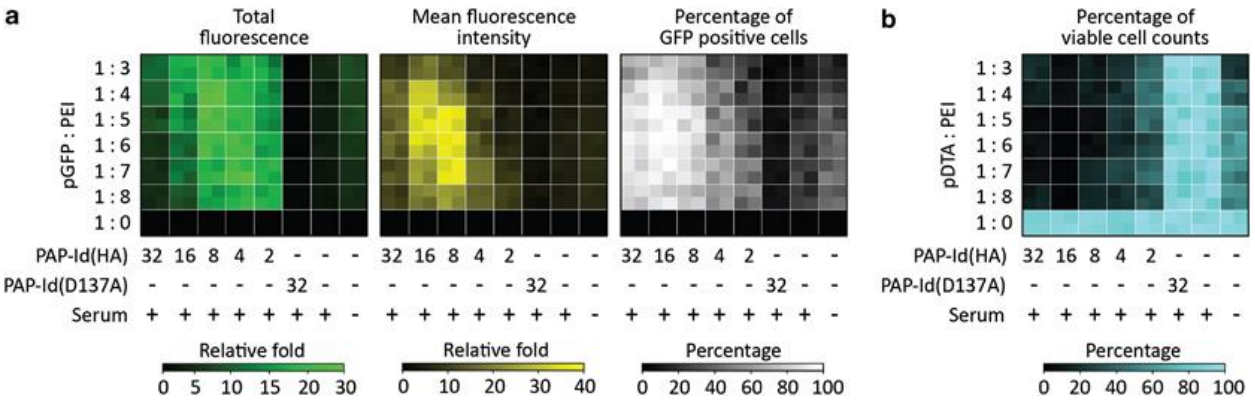

Figure A2: Molecular interaction-specific gene delivery of VMPs.
(a, b) VMPs were assembled with varying mass ratios among the three components: pGFP, PEI and PAP-Id. The mass ratio of plasmid to PEI was titrated from 1:3 to 1:8, which were then assembled with various mass ratios of PAP-Id(HA) to probe optimal gene transfer efficiency. PAP-Id(D137A) (no affinity) was used as a negative control as the loss-of-function point mutation abrogates the interaction with ICAM-1. (a) Heat map in green shows the total fluorescence measured by a fluorescence microplate reader after cell lysis (n = 4), in yellow shows the mean fluorescence intensity measured by flow cytometry (n = 4) and in white is the percentage of GFP-positive cells as compared with non-transfected control cells (n = 4). Fluorescence values are shown in relative fold difference compared with the negative control, of which the particles were assembled without PEI. (b) VMPs bearing pDTA (diphtheria toxin subunit A) were delivered to HeLa cells in a similar manner. Heat map in cyan shows the percentage of viable cells counted per image field (n = 4) relative to untreated normal HeLa cells. Trypan blue exclusion assay was used to stain nonviable cells and exclude those from the counts.

VMPs assembled with PAP-Id(D137A) did not show any sign of GFP expression. Particles assembled without the I domains, a formulation identical to conventional PEI-based transfection method, overall resulted in much lower GFP expression compared with VMPs. Furthermore, the addition of serum almost completely abolished GFP expression induced by conventional PEI-based transfection (Fig. A2a).

To demonstrate ICAM-1-specific delivery of functional genes, we assembled the particles with a plasmid encoding a catalytic domain (subunit A) of diphtheria toxin without the other two domains responsible for receptor-binding and endosomal escape[48] (pDTA). This would limit a potent cell killing only to the transfected cells but not to the neighboring non-transfected cells. Cell death mediated by pDTA-encapsulating VMPs would thus indicate that our delivery system was able to compensate for the functions provided by the other two missing domains: cell binding/entry and endosomal escape. Potent cytotoxicity in HeLa cells was evident at similar mass ratios found to be optimal for the delivery of pGFP (Fig. A2b). In contrast to highly efficient and ICAM-1-dependent cell killing by PAP-Id(HA)-mediated delivery, pDTA/PEI particles in the presence of serum and the VMPs assembled with PAP-Id(D137A) were completely ineffective in causing cell death. Altogether, these assays provided evidence that Id(HA), but not PEI, was responsible for specific targeting of ICAM-1 and cell entry of VMPs.

Inflammation-specific gene delivery to endothelial cells and monocytes/macrophages

Major cellular culprits of inflammatory diseases[49, 50] are endothelial cells that line the luminal surface of blood vessels and immune cells that actively elicit immune responses. Cell-surface expression of ICAM-1 is highly upregulated in the course of acute and chronic

inflammation, which makes ICAM-1 a target for inflammatory diseases. We chose human dermal microvascular endothelial cells (HMEC-1) and human acute monocytic leukemia cells (THP-1) as representative *in vitro* cellular models. As a model of inflammation, HMEC-1 and THP-1 were treated with endotoxin lipopolysaccharides (LPS) (Fig. A3a) that would initiate nuclear factor-kappa B transcription factor-dependent inflammatory response[51]. VMPs formulated with a fixed mass ratio of pGFP to PEI at 1:6 and varying amounts of targeting moiety were delivered to either normal or LPS-treated HMEC-1 (Fig. A3b, c) and THP-1 cells (Fig. A3d, e). Overall, LPS- or inflammation-dependent delivery of GFP gene was observed only with VMPs assembled with PAP-Id(HA), with >80% of cells being GFP-positive. Particles formed without the I domain showed a much lower efficiency of transfection independent of LPS treatment, which was largely abolished by the addition of serum. Notably, pGFP/PEI transfection caused cell death reaching as high as 90%, whereas VMPs with PAP-Id(HA) preserved the viability of both HMEC-1 and THP-1.

One of the major advantages of using the I domain for targeted delivery is that it cross-reacts with murine ICAM-1[41, 42], allowing the same targeting moiety to be used for preclinical animal studies. Similarly, we chose two types of cells, mouse brain microvascular endothelial cells (bEnd.3) and mouse leukemic monocyte macrophage cells (RAW 264.7), to study inflammation-specific delivery of VMPs bearing pGFP. Overall, the induction of ICAM-1 in murine cells in response to LPS was slower than in human cells (data not shown); accordingly, we delivered VMPs at 48 h post-LPS treatment (Fig. A4a). Similar to the effects of VMPs on human cells, mean fluorescence intensity and the percentage of GFP-positive cells for both bEnd.3 and RAW 264.7 were significantly higher in the group that were treated with LPS and

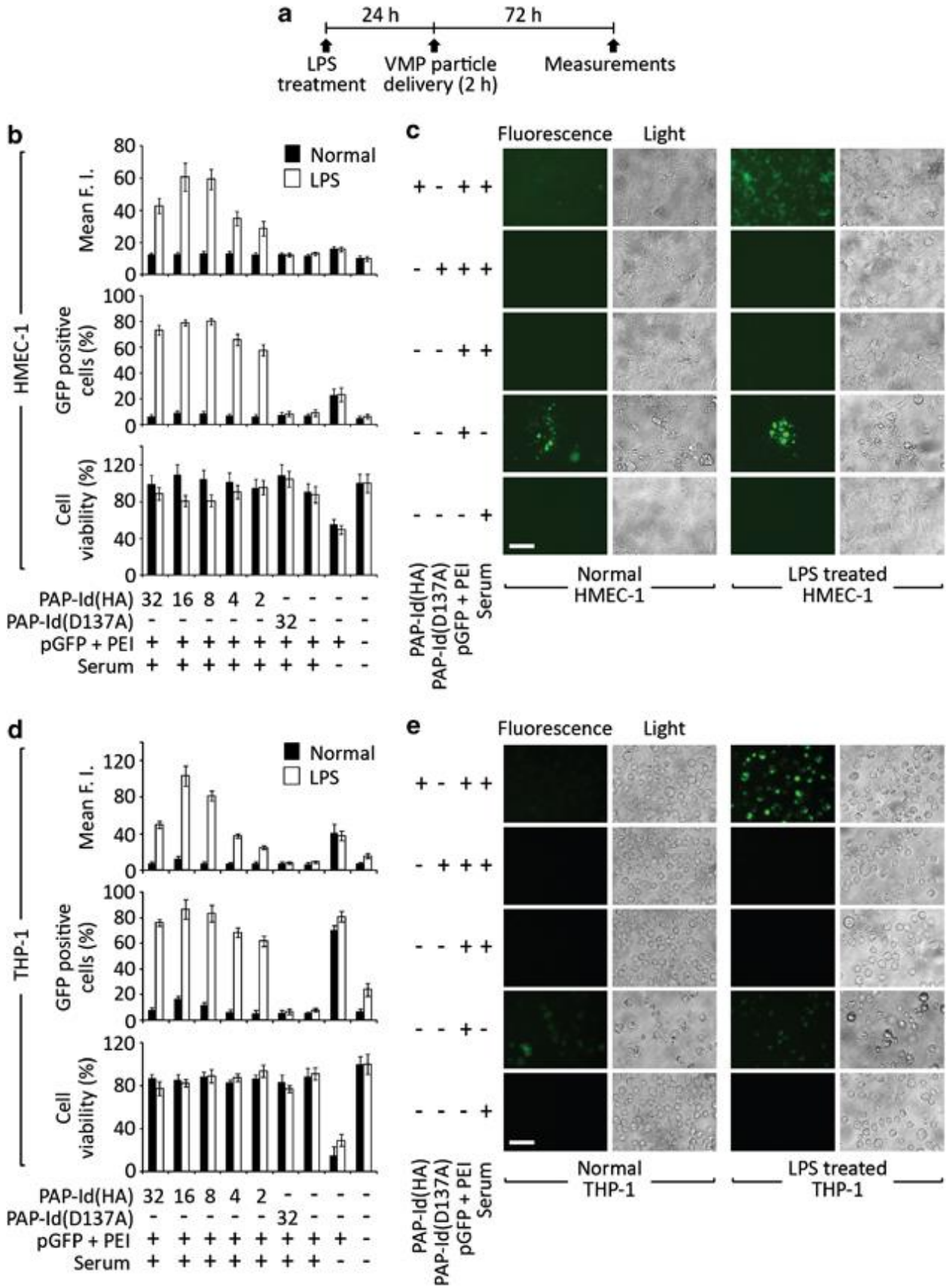
a
24 h
72 h
LPS treatment
VMP particle delivery (2 h)
Measurements
b
HMEC-1
Mean F. I.
GFP positive cells (%)
Cell viability (%)
Normal
LPS
PAP-Id(HA) 32 16 8 4 2 - - - -
PAP-Id(D137A) - - - - - 32 - - -
pGFP + PEI + + + + + + + + -
Serum + + + + + + + - -
c
Fluorescence
Light
PAP-Id(HA)
PAP-Id(D137A)
pGFP + PEI
Serum
Normal HMEC-1
LPS treated HMEC-1
d
THP-1
Mean F. I.
GFP positive cells (%)
Cell viability (%)
Normal
LPS
PAP-Id(HA) 32 16 8 4 2 - - - -
PAP-Id(D137A) - - - - - 32 - - -
pGFP + PEI + + + + + + + + -
Serum + + + + + + + - -
e
Fluorescence
Light
PAP-Id(HA)
PAP-Id(D137A)
pGFP + PEI
Serum
Normal THP-1
LPS treated THP-1

Figure A.3: Inflammation-specific targeted gene delivery to human endothelial cells and monocyte/macrophages.
(a) Timeline shows the sequence of LPS treatment, virus-particle delivery and measurements for human cell lines. Twenty-four hours of LPS treatment was required in human cells to trigger maximal ICAM-1 expression level for optimal delivery. (b–e) VMPs were formed with varying mass ratios of the components, pGFP, PEI and PAP-Id, and were delivered to either normal or LPS-treated HMEC-1 and human acute monocytic leukemia cells (THP-1). A fixed mass ratio of 1:6 between pGFP and PEI was used for all cases. Mass ratios of PAP-Id(HA) was titrated to assess the effect of avidity on the efficiency of ICAM-1-mediated endocytosis and gene delivery in human cell lines. PAP-Id(D137A) was used as a negative control. (b, d) Cells were analyzed for mean fluorescence intensity and percentage of GFP-positive cells by flow cytometry (n = 4). (b, d) Cell viability was measured by MTT assay (n = 4). Data represent mean ± s.d. (c, e) Representative fluorescence and light microscopic images of the optimal mass ratio (pGFP:PEI:PAP-Id adjusted to 1:6:16) are shown. Bar = 50 μm.

received VMPs formed with PAP-Id(HA) (Fig. A4b–e). pGFP/PEI without added serum resulted in up to 90% GFP-positive in bEnd.3, irrespective of LPS treatment (Fig. A4b, c). RAW 264.7 after treatment with LPS became enlarged and autofluorescent, resulted in an increase in fluorescence intensity across all conditions (Fig. A4d, e). Nonetheless, PAP-Id(HA)-mediated delivery resulted in a significant increase in fluorescence and as much as 20% cells were determined GFP-positive (Fig. A4d, e). For LPS-treated RAW 264.7cells, pGFP/PEI particles delivered without serum resulted in ~15% GFP-positive cells, ascribed to nonspecific phagocytic uptake of activated macrophages. PAP-Id(HA)-mediated delivery preserved cell viability, while non-specific pGFP/PEI transfection caused significant cell death in both the cell lines.

Inflammation-specific gene delivery to primary mouse lung cells

We also studied gene delivery to primary mouse lung cells cultured *in vitro*, harvested from a transgenic mouse strain, where exogenous Cre recombinase would excise the *lox*P-flanked transcriptional STOP region and turn on GFP expression. We formed VMPs with a plasmid encoding Cre recombinase fused to nuclear localization signal under the CMV promoter. Similarly, cells were treated with LPS and received VMPs (Fig. A5a), formulated with a fixed ratio of pCRE to PEI (1:6) and with varying amounts of PAP-Id (Fig. A5b). PAP-Id(HA)-mediated delivery was specific to LPS-treated cells, evidenced by increased mean fluorescence intensity (Fig. A5b, c). Normal cells treated with VMPs were as high as 40% GFP-positive, presumably because even a low copy number of Cre recombinase can excise STOP signal and induce GFP expression. PAP-Id(HA)-mediated delivery to LPS-treated cells, however, resulted in 90% GFP-positive cells. Conventional transfection of pCRE/PEI in serum-free media resulted in a

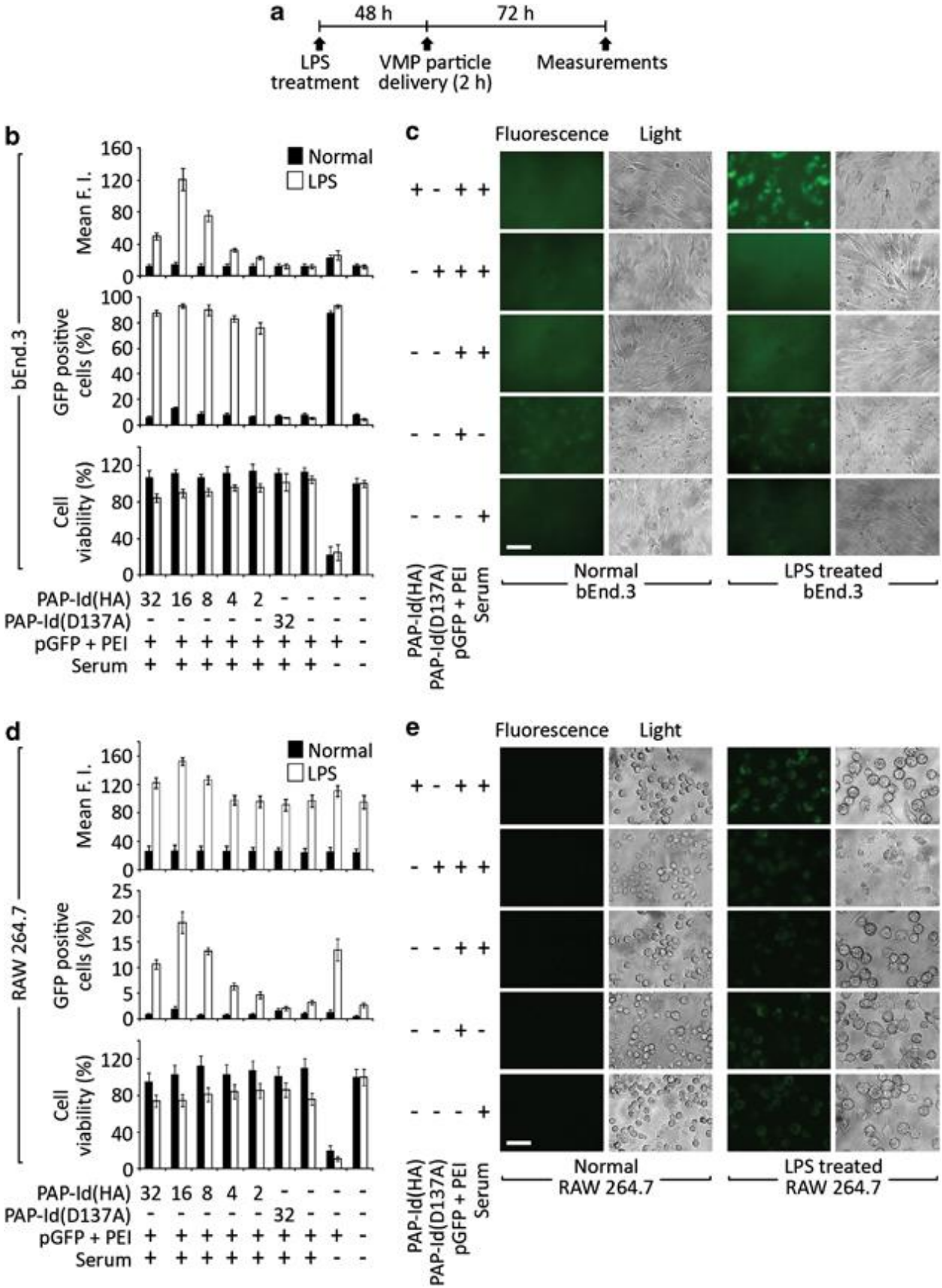
a
48 h
72 h
LPS treatment
VMP particle delivery (2 h)
Measurements
b
bEnd.3
Normal
LPS
Mean F. I.
GFP positive cells (%)
Cell viability (%)
PAP-Id(HA) 32 16 8 4 2 - - - -
PAP-Id(D137A) - - - - - 32 - - -
pGFP + PEI + + + + + + + + -
Serum + + + + + + + - -
c
Fluorescence
Light
PAP-Id(HA)
PAP-Id(D137A)
pGFP + PEI
Serum
Normal bEnd.3
LPS treated bEnd.3
d
RAW 264.7
Normal
LPS
Mean F. I.
GFP positive cells (%)
Cell viability (%)
PAP-Id(HA) 32 16 8 4 2 - - - -
PAP-Id(D137A) - - - - - 32 - - -
pGFP + PEI + + + + + + + + -
Serum + + + + + + + - -
e
Fluorescence
Light
PAP-Id(HA)
PAP-Id(D137A)
pGFP + PEI
Serum
Normal RAW 264.7
LPS treated RAW 264.7

Figure A4: Inflammation-specific targeted gene delivery to mouse endothelial cells and monocyte/macrophages.
(a) Timeline shows the sequence of LPS treatment, virus-particle delivery and measurements for mouse cell lines. LPS was treated for 48 h in mouse cells to reach maximal ICAM-1 expression level for optimal delivery. (b–e) VMPs were formed with varying mass ratios of the components, pGFP, PEI and PAP-Id, and were delivered to either normal or LPS-treated bEnd.3 and RAW 264.7. A fixed mass ratio of 1:6 between pGFP and PEI was used for all cases. Mass ratios of PAP-Id(HA) was titrated to assess the effect of avidity on the efficiency of ICAM-1-mediated endocytosis and gene delivery in mouse cell lines. PAP-Id(D137A) was used as a negative control. (b, d) Cells were analyzed for mean fluorescence intensity and percentage of GFP-positive cells by flow cytometry (n = 4). (b, d) Cell viability was measured by MTT assay (n = 4). Data represent mean ± s.d. (c, e) Representative fluorescence and light microscopic images of the optimal mass ratio (pGFP:PEI:PAP-Id adjusted to 1:6:16) are shown. Scale bar, 50 μm.

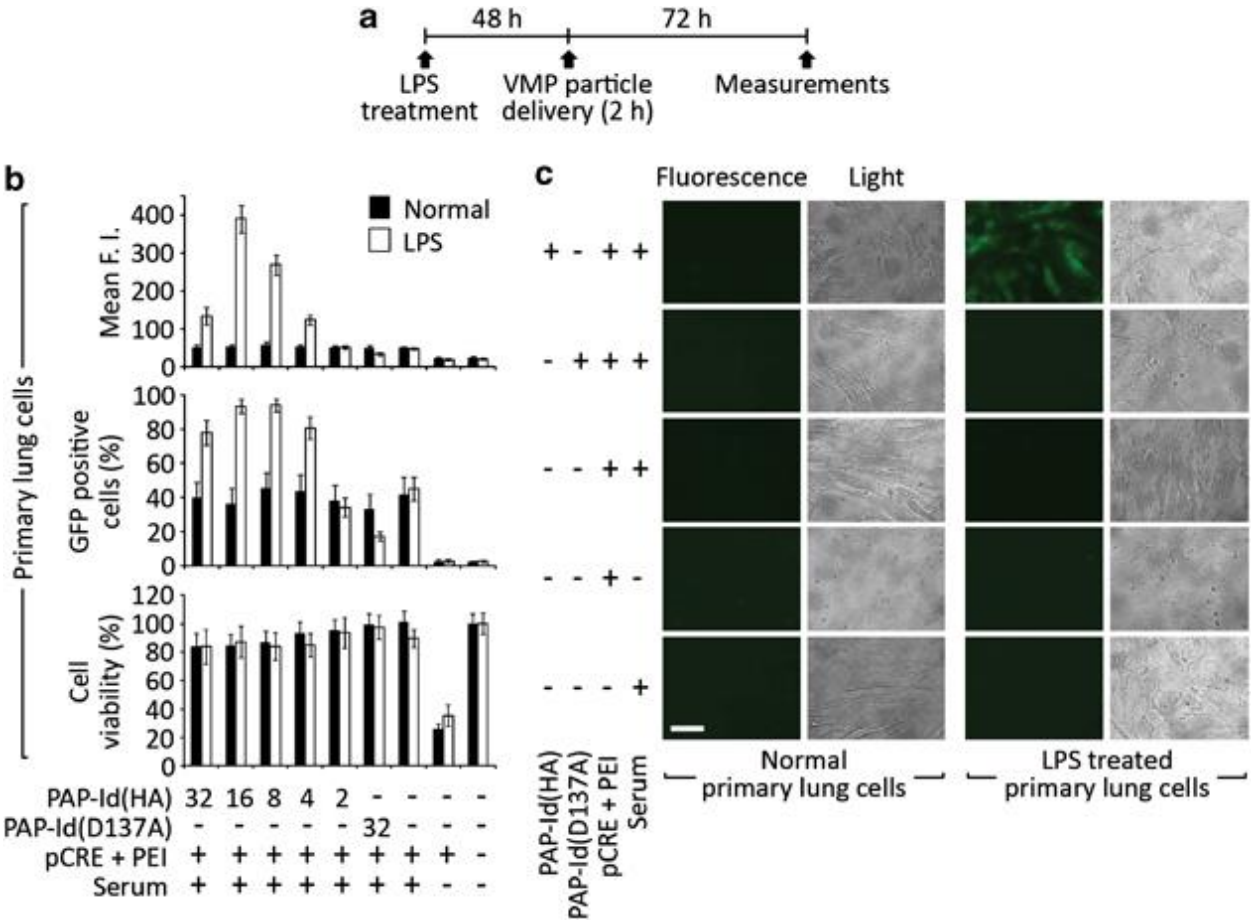

Figure A5: Inflammation-specific targeted delivery to primary mouse lung cells.
(a) Timeline shows the sequence of treatments for VMP delivery to primary mouse lung cells in culture. Lung cells were harvested from a mouse strain engineered for inducible expression of GFP after Cre recombinase-mediated loxP-STOP-loxP excision. (b) VMPs were assembled with pCRE (Cre recombinase) and delivered to either normal or LPS treated primary mouse lung cells. A fixed mass ratio of 1:6 between pCRE and PEI was used for all cases. Mass ratios of PAP-Id(HA) was titrated to assess the effect of avidity on the efficiency of ICAM-1-mediated endocytosis and gene delivery in primary lung cells. PAP-Id(D137A) was used as a negative control. Cells were analyzed for mean fluorescence intensity and percentage of GFP-positive cells by flow cytometry (n = 4). Cell viability was measured by MTT assay (n = 4). Data represent mean ± s.d. (c) Representative fluorescence and light microscopic images of the optimal mass ratio (pCRE:PEI:PAP-Id adjusted to 1:6:16) are shown. Bar = 50 μm.

significant cytotoxicity of primary cells, whereas no cell death was observed with fully assembled VMPs.

Inflammation-specific targeted gene delivery of VMPs in vivo

Gene delivery has the potential to treat many diseases, which may benefit much from systemic and targeted treatments via intravenous routes. Cationic nonviral gene delivery systems without molecular targeting are severely limited due to loss of efficiency in cell entry, inhibited by negatively charged molecules (for example, glycosaminoglycans) in blood serum. We chose to study the delivery of VMPs to the lung, where endothelial cells comprise a large portion of tissue composition. We also confirmed that cell-surface expression of ICAM-1 is highly upregulated in the lungs after systemic LPS treatment (data not shown).

As for specific cell types, upregulation of ICAM-1 was observed in >50% of CD31-positive cells (Fig. A6a), which consist of mainly endothelial cells and small percentages of a subset of immune cells. We also found a comparable level of ICAM-1 induction in F4/80-positive myeloid lineage macrophages, which participate critically in inflammatory diseases, including atherosclerosis and cancer (Fig. A6b). We injected VMPs bearing pGFP via the lateral tail vein route, either to normal or LPS-treated mice (BALB/c) (Fig. A6c). Relative amount of GFP mRNA expression in the lung was analyzed at 48 h post injection of VMPs (Fig. A6d). PAP-Id(HA)-mediated delivery was specific to LPS-treated group, whereas pGFP/PEI particles had a lower gene transfer efficiency irrespective of the induction of inflammation (Fig. A6d). Similarly, gene delivery by VMPs formulated with PAP-Id(D137A) was ineffective (Fig. A6d). VMP delivery for GFP expression in the lung was also assessed at 72 h post-delivery by immunostaining of fixed/permeabilized and collagenase-digested lung cells (Fig. A6e). Gene delivery by VMPs with

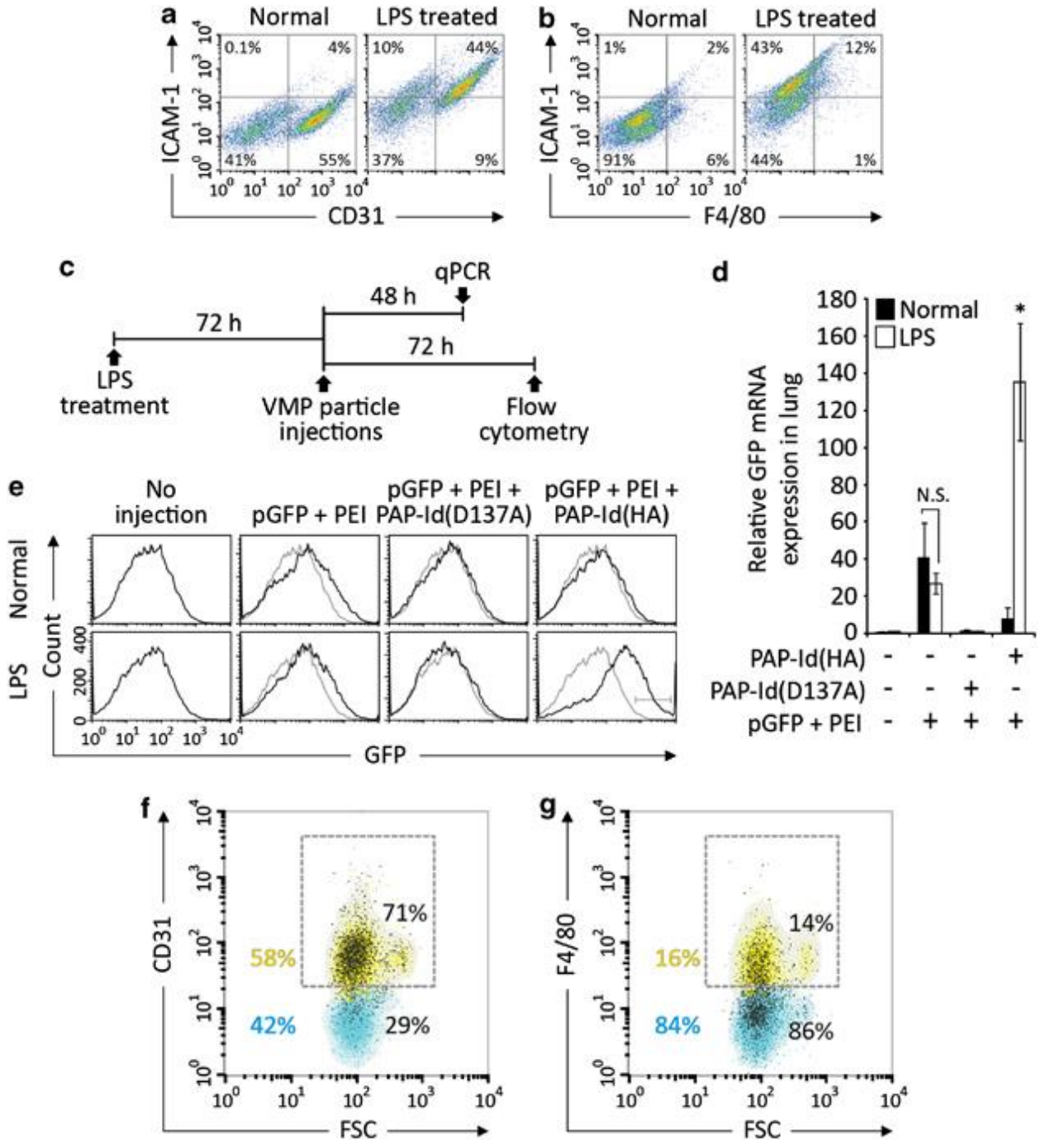
a
Normal
LPS treated
ICAM-1
CD31
0.1%
4%
41%
55%
10%
44%
37%
9%
b
Normal
LPS treated
ICAM-1
F4/80
1%
2%
91%
6%
43%
12%
44%
1%
c
qPCR
48 h
72 h
72 h
LPS treatment
VMP particle injections
Flow cytometry
d
Relative GFP mRNA expression in lung
Normal
LPS
N.S.
*
PAP-Id(HA)
PAP-Id(D137A)
pGFP + PEI
e
No injection
pGFP + PEI
pGFP + PEI + PAP-Id(D137A)
pGFP + PEI + PAP-Id(HA)
Normal
LPS
Count
GFP
f
CD31
FSC
71%
58%
42%
29%
g
F4/80
FSC
14%
16%
84%
86%

Figure A6: Systemic and inflammation-specific targeted gene delivery to the mouse lung in vivo. (a) Cell-surface expression of ICAM-1 in CD31- positive endothelial cells and (b) F4/80-positive monocyte/macrophages in the mouse lung was detected by flow cytometry with I domain fused to GFP (GFP-Id(HA)) (n = 4). Lungs were collected 72 h after systemic LPS injection for comparison of the level of ICAM-1 expression between normal and inflamed states. Percentage of cells in each quadrant is shown. (c–g) VMPs bearing pGFP was systemically applied in vivo to target inflamed mouse lung. Mass ratio of the components of VMPs was fixed to 1:6:16 (pGFP:PEI:PAP-Id). VMPs were injected intravenously via lateral tail vein route into either normal or LPS-treated mice (BALB/c). (c) Timeline shows the sequence of treatments, injections and data collection. (d) Lungs were collected and analyzed for GFP mRNA expression by quantitative PCR. Expression was normalized to a housekeeping gene (CYC1) and presented as relative fold difference as compared with PAP-Id(D137A) case (n = 4). PAP-Id(HA)-mediated delivery to LPS-treated group was statistically significant among all the groups. Data represent mean ± s.d. (*$P < 0.05$, one-way analysis of variance followed by Tukey's post-hoc test). (e) Flow cytometric histograms show GFP expression assessed by immunostaining of fixed/ permeabilized lung cells (n = 4). Lung cells were dual labeled for GFP and for either CD31 or F4/80 and were analyzed for the percentage of GFP-positive cells (black dots) within (f) CD31-positive or (g) F4/80-positive subset (yellow region and dotted box). FSC, forward scatter; NS, not significant.

PAP-Id(HA) was specific to LPS-treated group, resulting in nearly 15% of the entire cell population being GFP-positive, while pGFP/PEI particles produced much less GFP-positive cells irrespective of inflammatory condition (Fig. A6e). We further analyzed for the types of cells that were targeted by PAP-Id(HA)-mediated delivery (Fig. A6f, g). Specifically, 71% of GFP-positive cells were CD31-positive cells (Fig. A6f), whereas only about 14% of GFP-positive cells were F4/80-positive (Fig. A6g). This finding demonstrates that intravenous delivery of VMPs was mainly against the cellular components that are directly accessible to the agents in circulation and express high levels of ICAM-1 in response to LPS treatment.

Discussion

In this study, we have demonstrated that VMPs can be formulated by functionalizing PEI with a PAP for fusion to targeting moieties, allowing systemic and molecular interaction-dependent gene delivery. With the targeting moiety derived from the integrin LFA-1, our VMPs were highly selective to cells with inflammation-induced overexpression of ICAM-1. VMPs mimicked some of the essential properties of non-enveloped viruses by possessing the ability to (a) package large nucleic acid molecules by PEI-mediated condensation, (b) bind specifically to cell-surface receptors, (c) elicit receptor-mediated endocytosis, (d) escape endosomal degradation (attributed to the proton sponge effect of PEI) and (e) express the payload gene with high efficiency.

VMPs were far more efficient in delivering genes to cells with overexpressed ICAM-1 than cells at basal level, which enabled inflammation-specific delivery both *in vitro* and *in vivo*. This is analogous to HRVs that displayed enhanced infectivity when host cells were treated with

inflammatory cytokines and upregulated ICAM-1[52]. The efficiency of gene transfer by VMPs was also largely dependent on the coating density or avidity of PAP-Id, as it would influence the degree of multimeric interaction with ICAM-1 necessary for receptor-mediated endocytosis. Furthermore, in contrast to toxicity-laden conventional transfection by PEI due to plasma membrane destabilization associated with non-specific internalization, molecular interaction-dependent uptake of VMPs produced little cytotoxicity. We speculate that, unlike how nonspecific uptake of densely charged cationic particles can damage cell membranes and cause cell death,[9] viability may have been maintained as receptor-mediated endocytosis is an active cellular process that can be regulated by cells. Greatly reduced toxicity with VMPs is also ascribed to the presence of PAP that counterbalances positive charges of PEI.

By targeting ICAM-1, VMPs delivered genes mostly to CD31-positive cells in the lung, which are predominantly composed of pulmonary endothelial cells. With the current detection method of gene expression, we failed to observe GFP expression in other organs, including the liver, despite accumulation of VMPs therein. Although further work is required to finely control the size of VMPs and its subsequent effects on biodistribution, clearance rate and other pharmacokinetic parameters with the given size of VMPs (150–250 nm in diameter), we expect that targeted cells would mainly be the ones that reside in the blood-accessible stroma as opposed to the parenchyma. However, endothelial cells as well as immune cells such as monocytes/macrophages have been implicated to have critical roles in the pathology of inflammatory diseases, especially in the cases of atherosclerosis[50], psoriasis and arthritis[53]. The ability to deliver corrective genes specifically to these types of cells under

dysregulated inflammation should provide an immense therapeutic opportunity, even without the access to the parenchyma.

Apart from the ability of viruses to efficiently deliver genes into host cells, they also have evolved mechanisms to self-replicate their genome, elude the immune system by synthesizing viral cytokine homologues and over-ride host cellular component or activity. Likewise, the use of more advanced genetic materials (for example, plasmids with promoters for improved expression or cell type-specific expression, mechanisms for self-replication/integration or functions that can be activated under disease-associated cellular activities) may further improve VMPs for enhanced gene transfer efficiency, specificity and safety. Finally, we anticipate that simplicity and versatility of the system developed in this study may facilitate rapid assessments of multifaceted VMPs, formed with a range of different targeting moieties and payloads, and contribute to successful translation of nonviral vectors into the clinic.

REFERENCES

1. Hacein-Bey-Abina, S., et al., *Efficacy of gene therapy for X-linked severe combined immunodeficiency.* N Engl J Med, 2010. **363**(4): p. 355-64.
2. Bainbridge, J.W., et al., *Effect of gene therapy on visual function in Leber's congenital amaurosis.* N Engl J Med, 2008. **358**(21): p. 2231-9.
3. Manno, C.S., et al., *Successful transduction of liver in hemophilia by AAV-Factor IX and limitations imposed by the host immune response.* Nat Med, 2006. **12**(3): p. 342-7.
4. Mendell, J.R., et al., *Dystrophin immunity in Duchenne's muscular dystrophy.* N Engl J Med, 2010. **363**(15): p. 1429-37.
5. Breitbach, C.J., et al., *Intravenous delivery of a multi-mechanistic cancer-targeted oncolytic poxvirus in humans.* Nature, 2011. **477**(7362): p. 99-102.
6. McCormack, M.P. and T.H. Rabbitts, *Activation of the T-cell oncogene LMO2 after gene therapy for X-linked severe combined immunodeficiency.* N Engl J Med, 2004. **350**(9): p. 913-22.
7. Yang, Y., et al., *Cellular immunity to viral antigens limits E1-deleted adenoviruses for gene therapy.* Proc Natl Acad Sci U S A, 1994. **91**(10): p. 4407-11.
8. Yang, Y., et al., *Cellular and humoral immune responses to viral antigens create barriers to lung-directed gene therapy with recombinant adenoviruses.* J Virol, 1995. **69**(4): p. 2004-15.
9. Lv, H., et al., *Toxicity of cationic lipids and cationic polymers in gene delivery.* Journal of Controlled Release, 2006. **114**(1): p. 100-9.
10. Luo, D. and W.M. Saltzman, *Synthetic DNA delivery systems.* Nat Biotechnol, 2000. **18**(1): p. 33-7.
11. Moret, I., et al., *Stability of PEI-DNA and DOTAP-DNA complexes: effect of alkaline pH, heparin and serum.* Journal of Controlled Release, 2001. **76**(1-2): p. 169-81.
12. Staprans, I. and J.M. Felts, *Isolation and characterization of glycosaminoglycans in human plasma.* J Clin Invest, 1985. **76**(5): p. 1984-91.
13. Ruponen, M., S. Yla-Herttuala, and A. Urtti, *Interactions of polymeric and liposomal gene delivery systems with extracellular glycosaminoglycans: physicochemical and transfection studies.* Biochim Biophys Acta, 1999. **1415**(2): p. 331-41.
14. Kumar, P., et al., *T cell-specific siRNA delivery suppresses HIV-1 infection in humanized mice.* Cell, 2008. **134**(4): p. 577-86.
15. Peer, D., et al., *Systemic leukocyte-directed siRNA delivery revealing cyclin D1 as an anti-inflammatory target.* Science, 2008. **319**(5863): p. 627-30.
16. Song, E., et al., *Antibody mediated in vivo delivery of small interfering RNAs via cell-surface receptors.* Nat Biotechnol, 2005. **23**(6): p. 709-17.
17. Davis, M.E., et al., *Evidence of RNAi in humans from systemically administered siRNA via targeted nanoparticles.* Nature, 2010. **464**(7291): p. 1067-70.
18. Waehler, R., S.J. Russell, and D.T. Curiel, *Engineering targeted viral vectors for gene therapy.* Nat Rev Genet, 2007. **8**(8): p. 573-87.
19. Maheshri, N., et al., *Directed evolution of adeno-associated virus yields enhanced gene delivery vectors.* Nat Biotechnol, 2006. **24**(2): p. 198-204.

20. Douglas, J.T., et al., *Targeted gene delivery by tropism-modified adenoviral vectors.* Nat Biotechnol, 1996. **14**(11): p. 1574-8.
21. Lee, R.J. and L. Huang, *Folate-targeted, anionic liposome-entrapped polylysine-condensed DNA for tumor cell-specific gene transfer.* Journal of Biological Chemistry, 1996. **271**(14): p. 8481-7.
22. Erbacher, P., J.S. Remy, and J.P. Behr, *Gene transfer with synthetic virus-like particles via the integrin-mediated endocytosis pathway.* Gene Ther, 1999. **6**(1): p. 138-45.
23. Ogris, M., et al., *PEGylated DNA/transferrin-PEI complexes: reduced interaction with blood components, extended circulation in blood and potential for systemic gene delivery.* Gene Ther, 1999. **6**(4): p. 595-605.
24. Wagner, E., et al., *Transferrin-Polycation Conjugates as Carriers for DNA Uptake into Cells.* Proceedings of the National Academy of Sciences of the United States of America, 1990. **87**(9): p. 3410-3414.
25. Boussif, O., et al., *A Versatile Vector for Gene and Oligonucleotide Transfer into Cells in Culture and in-Vivo - Polyethylenimine.* Proceedings of the National Academy of Sciences of the United States of America, 1995. **92**(16): p. 7297-7301.
26. Sadeqzadeh, E., et al., *Combined MUC1-specific nanobody-tagged PEG-polyethylenimine polyplex targeting and transcriptional targeting of tBid transgene for directed killing of MUC1 over-expressing tumour cells.* Journal of Controlled Release, 2011. **156**(1): p. 85-91.
27. Somiya, M., et al., *Targeting of polyplex to human hepatic cells by bio-nanocapsules, hepatitis B virus surface antigen L protein particles.* Bioorganic & Medicinal Chemistry, 2012. **20**(12): p. 3873-3879.
28. Hildebrandt, I.J., et al., *Optical imaging of transferrin targeted PEI/DNA complexes in living subjects.* Gene Therapy, 2003. **10**(9): p. 758-764.
29. Kunath, K., et al., *Galactose-PEI-DNA complexes for targeted gene delivery: degree of substitution affects complex size and transfection efficiency.* Journal of Controlled Release, 2003. **88**(1): p. 159-172.
30. Godbey, W.T., K.K. Wu, and A.G. Mikos, *Poly(ethylenimine) and its role in gene delivery.* Journal of Controlled Release, 1999. **60**(2-3): p. 149-60.
31. Sonawane, N.D., F.C. Szoka, Jr., and A.S. Verkman, *Chloride accumulation and swelling in endosomes enhances DNA transfer by polyamine-DNA polyplexes.* Journal of Biological Chemistry, 2003. **278**(45): p. 44826-31.
32. Akinc, A., et al., *Exploring polyethylenimine-mediated DNA transfection and the proton sponge hypothesis.* J Gene Med, 2005. **7**(5): p. 657-63.
33. Dustin, M.L., et al., *Induction by IL 1 and interferon-gamma: tissue distribution, biochemistry, and function of a natural adherence molecule (ICAM-1).* J Immunol, 1986. **137**(1): p. 245-54.
34. Marlin, S.D. and T.A. Springer, *Purified Intercellular-Adhesion Molecule-1 (Icam-1) Is a Ligand for Lymphocyte Function-Associated Antigen-1 (Lfa-1).* Cell, 1987. **51**(5): p. 813-819.
35. Albelda, S.M., C.W. Smith, and P.A. Ward, *Adhesion molecules and inflammatory injury.* FASEB J, 1994. **8**(8): p. 504-12.

36. Tomassini, J.E., et al., *Cdna Cloning Reveals That the Major Group Rhinovirus Receptor on Hela-Cells Is Intercellular-Adhesion Molecule-1.* Proceedings of the National Academy of Sciences of the United States of America, 1989. **86**(13): p. 4907-4911.
37. Grunert, H.P., et al., *Internalization of human rhinovirus 14 into HeLa and ICAM-1-transfected BHK cells.* Medical Microbiology and Immunology, 1997. **186**(1): p. 1-9.
38. Muro, S., et al., *A novel endocytic pathway induced by clustering endothelial ICAM-1 or PECAM-1.* Journal of Cell Science, 2003. **116**(8): p. 1599-1609.
39. Jin, M., et al., *Directed evolution to probe protein allostery and integrin I domains of 200,000-fold higher affinity.* Proceedings of the National Academy of Sciences of the United States of America, 2006. **103**(15): p. 5758-5763.
40. Park, S., et al., *Self-assembled nanoplatform for targeted delivery of chemotherapy agents via affinity-regulated molecular interactions.* Biomaterials, 2010. **31**(30): p. 7766-75.
41. Kang, S., et al., *Tunable physiologic interactions of adhesion molecules for inflamed cell-selective drug delivery.* Biomaterials, 2011. **32**(13): p. 3487-98.
42. Chen, X.Y., et al., *Inflamed leukocyte-mimetic nanoparticles for molecular imaging of inflammation.* Biomaterials, 2011. **32**(30): p. 7651-7661.
43. Cabantous, S., T.C. Terwilliger, and G.S. Waldo, *Protein tagging and detection with engineered self-assembling fragments of green fluorescent protein.* Nat Biotechnol, 2005. **23**(1): p. 102-7.
44. Soriano, P., *The PDGF alpha receptor is required for neural crest cell development and for normal patterning of the somites.* Development, 1997. **124**(14): p. 2691-2700.
45. Cudre-Mauroux, C., et al., *Lentivector-mediated transfer of Bmi-1 and telomerase in muscle satellite cells yields a Duchenne myoblast cell line with long-term genotypic and phenotypic stability.* Human Gene Therapy, 2003. **14**(16): p. 1525-1533.
46. Zou, K., et al., *Production of offspring from a germline stem cell line derived from neonatal ovaries.* Nature Cell Biology, 2009. **11**(5): p. 631-U424.
47. Huth, J.R., et al., *NMR and mutagenesis evidence for an I domain allosteric site that regulates lymphocyte function-associated antigen 1 ligand binding.* Proceedings of the National Academy of Sciences of the United States of America, 2000. **97**(10): p. 5231-5236.
48. Choe, S., et al., *The Crystal-Structure of Diphtheria-Toxin.* Nature, 1992. **357**(6375): p. 216-222.
49. Coussens, L.M. and Z. Werb, *Inflammation and cancer.* Nature, 2002. **420**(6917): p. 860-7.
50. Ross, R., *Atherosclerosis is an inflammatory disease.* American Heart Journal, 1999. **138**(5): p. S419-S420.
51. Chow, J.C., et al., *Toll-like receptor-4 mediates lipopolysaccharide-induced signal transduction.* Journal of Biological Chemistry, 1999. **274**(16): p. 10689-10692.
52. Subauste, M.C., et al., *Infection of a human respiratory epithelial cell line with rhinovirus. Induction of cytokine release and modulation of susceptibility to infection by cytokine exposure.* J Clin Invest, 1995. **96**(1): p. 549-57.
53. Folkman, J., *Angiogenesis in cancer, vascular, rheumatoid and other disease.* Nat Med, 1995. **1**(1): p. 27-31.

APPENDIX B

SSTR2 as a genetic reporter for quantitative imaging of distribution, expansion, and activity of adoptively transferred chimeric antigen receptor T cells

Park S contributed to the *in vitro* and *ex vivo* validation of various CAR T cell models, including E to T assays and *ex vivo* flow cytometry, as well as *in vivo* luminescence imaging. This included the experiments related to Figures 1, 5, and 6.

Summary

Adoptive T cell therapy (ATT) has shown promising results for the treatment of certain cancers owing to the increased specificity and persistence in targeting and killing tumor cells. To date, the efficacy and toxicity of T cell activity *in patients* have been monitored by peripheral T cell counts and serum cytokine measurements - methods which provide a useful but incomplete picture of the spatiotemporal dynamics of ATT. Quantitative positron emission tomography/computed tomography (PET/CT) imaging techniques have yet to be applied to clinical monitoring of ATT; however, it remains to be seen if molecular imaging can provide the specificity and sensitivity required to detect initial trafficking to subsequent expansion of sparsely distributed, adoptively transferred T cells. To define the detection limit of infiltrating T cells in solid tumors, we produced mosaic xenografts of Jurkat T cells with varying expression of the reporter marker somatostatin receptor 2 (SSTR2), and performed PET/CT imaging to detect the uptake of SSTR2 radiotracer over the course of tumor growth. Using this model, SSTR2 expressing T cells were detected at a density of as low as 1% within tumors larger than 100

mm^3 with 95% specificity and 70% sensitivity. To apply SSTR2 as an imaging marker to predict ATT activity *in vivo*, we engineered primary human T cells with a single lentiviral vector to express SSTR2 and a chimeric antigen receptor (CAR) specific to intercellular adhesion molecule (ICAM-1) that is overexpressed in anaplastic thyroid cancer. Tumor specific CAR T cell localization and expansion were visualized in a metastatic tumor model in mice, which correlated with T cell killing of tumors. Our study demonstrates the potential for SSTR2-based, real-time quantitative imaging of adoptively transferred T cells, enabling the visualization and monitoring on-site and off-site T cell activity.

Introduction

ATT is being studied as a potent treatment strategy for cancers that are refractory to standard chemotherapy and radiation therapy. Currently, serum cytokine profiles associated with T cell activation (interferon-γ, IL-2, IL-6)[1, 2] are used to measure activity of adoptive T cells in patients. However, while useful, changes in serum cytokine levels likely reflect a broader, systemic immune response within the body, reflecting not only the activation of adoptively transferred T cells, but also their effects on neighboring immune cells as well as dying tumor cells. The ability to map the distribution of T cells in the body will not only significantly improve monitoring T cell activity against tumor and potential toxicity from off-site targeting, but could also contribute to exploring adjuvant therapies to enhance adoptive T cell efficacy against solid cancers.

The current gold-standards for whole-body visualization of cell trafficking are SPECT, PET/CT, or PET/MRI techniques for detection of radiolabeled cells in combination with anatomical information of the body. Current reporter markers used in preclinical and clinical studies are based on both intracellular enzymes e.g., herpes simplex virus type-1 thymidine kinase (HSV1-tk)[3, 4] and surface receptors e.g., sodium iodide symporter (NIS)[5] and prostate-specific membrane antigen (PSMA)[6]. However, previous clinically-relevant studies have not examined T cell detection in a quantitative and statistically rigorous manner to fully demonstrate the feasibility of harnessing genetic reporters for detection of adoptively transferred T cell distribution[7-15]. We have chosen SSTR2 as a reporter marker in efforts to determine the detection limit of T cells infiltrating solid tumors, and also to predict temporal kinetics of T cell recruitment and expansion, directly related to T cell activity against tumor. SSTR2 belongs to a family of G protein coupled receptor, and its expression is restricted to within the brain, gastrointestinal tract, and kidneys.[16] SSTR2 is a potentially ideal reporter marker for monitoring ATT for its limited expression in the body and owing to a clinical use of radiotracers for SSTR2 (e.g., DOTATOC, DOTATATE) for detection of SSTR2-overexpressing neuroendocrine tumors[17]. To determine the limit of detection of T cells within a solid tumor mass, we introduced SSTR2 into Jurkat T cells and titrated these with wild type Jurkat cells to produce subcutaneous Jurkat tumor xenografts, each with a defined percentage of SSTR2 expressing cells ranging from 0 – 100 %, with the aim of replicating the varying degrees of T cell localization at tumor sites and T cell expansion upon activation. In the course of tumor growth, we performed PET/CT imaging using SSTR2 radiotracer (^{68}Ga-DOTATOC) to quantify the

detection limit of T cells within a tumor, and to correlate radiotracer uptake with tumor size and percentages of SSTR2 expressing cells.

On-going activity of T cells against both on- and off-tumor sites can be predicted by quantitative imaging of T cell distribution and expansion. Observation of T cell activity in the body is based on the presumption that adoptively transferred T cells will proliferate upon activation by interaction with target antigen-expressing cells, leading to an increase in T cell density and uptake of PET radiotracers. Therefore, to further demonstrate the utility of SSTR2 for imaging T cell distribution and expansion, we designed a single lentivirus vector to modify T cells to express both SSTR2 and CAR specific to ICAM-1, which is overexpressed in a range of malignant cancers. Whole-body imaging of SSTR2 expressing, ICAM-1 specific CAR T cells by PET/CT was then evaluated in mice with systemic growth of poorly differentiated, radioactive iodine resistant, anaplastic thyroid tumor[18, 19]. Our study demonstrates the application of SSTR2 as a clinically adaptable reporter for detection of adoptively transferred T cell activity against tumors and potential off-target sites.

Experimental Procedures

Mammalian cell culture

Parental HeLa, HEK 293T (ATCC), and 8505c (DSMZ) were transduced with lentivirus encoding Firefly Luciferase-F2A-GFP (Biosettia) followed by fluorescence activated cell sorting (FACS) to purify GFP expressing cells. HeLa-FLuc^{+}GFP^{+} cells and HEK 293-FLuc^{+}GFP^{+} cells were cultured in Advanced Dulbecco's Modified Eagle Medium containing 10% (v/v) fetal bovine

serum (FBS), 2 mM L-alanyl-L-glutamine dipeptide (Gibco), and 100 U/ml Penicillin-Streptomycin (Pen/Strep) (Gibco). 8505c-FLuc^{+}GFP^{+} cells were cultured in RPMI-1640 supplemented with 10% (v/v) FBS, 2 mM L-alanyl-L-glutamine dipeptide and 100 U/ml Pen/Strep. Human peripheral blood was obtained from healthy volunteer donors by venipuncture. Peripheral blood mononuclear cells (PBMC) were isolated over Ficoll-Paque PLUS (GE Healthcare) and cultured in GIBCO Optimizer CTS T-cell Expansion SFM (Thermo) supplemented with 5% human AB serum (Sigma), 2 mM L-alanyl-L-glutamine dipeptide, 100 U/ml Pen/Strep and 30 IU/ml human IL-2 (Cell Sciences). Non-adherent cells were removed after 24hr and magnetically enriched for T cells with Dynabeads CD3/CD28 T cell expander (Thermo) at a 2:1 bead:T cell ratio. Dynabead-bound T cells were subsequently cultured in IL-2 containing media at a density of 1 – 2 x 10^6 cells/ml. All cells were incubated at 37°C in a 5 % CO_2 humidified incubator.

Construction of ICAM-1 CAR and SSTR reporter genes

The CAR gene specific to ICAM-1 was derived from the single-chain fragment variable (scFv) sequence of a murine monoclonal anti-human R6.5 antibody – itself derived from hybridoma (ATCC). The R6.5 specific scFcv was then fused with the transmembrane and cytoplasmic domains of CD28, CD137, and CD3ζ of an independent third generation CAR gene (a kind gift from Dr. Carl June at University of Pennsylvania[26]). The complete R6.5 CAR was then subcloned into a pLenti backbone. A lentivirus vector (derived from CAR vector) encoding human SSTR2 (NM_001050) was constructed by synthesizing SSTR2 coding sequencing (IDT) and inserting it into the vector using Xba1 and Sal1 sites.

Lentivirus production and transduction of T cells

Lentivirus particles were produced by transiently transfecting HEK 293 cells using calcium phosphate. Briefly, 10 μg transfer gene, 7.5 μg CMV-dR8.2 (Addgene) and 5 μg pCMV-VSVG (Addgene) were mixed and incubated with 2 M $CaCl_2$ followed by 2x HBSS. Resulting solutions were added dropwise to 10 cm^2 cell culture dishes seeded with 3.2 x 10^6 HEK 293 in 10 ml DMEM 24 hr previously. Transfection media was replaced after 6 hr. Media containing lentivirus was harvested at 48 and 72 hr post transfection, filtered through 0.45 μm filters, and concentrated by ultracentrifugation at 75,000x g for 2 hr at 4 °C. Lentivirus was then resuspended in serum containing media at an approximate titer of 10^8/ml and frozen at -80 °C. Human T cells were transduced 24 - 72 hr post activation with CD3/CD28 Dynabeads either by spinfection at 1,000x g for 1 hr at 32°C or by overnight incubation of lentivirus in the presence of Synperonic F108 (Sigma)[27]. T cells were also transduced a second time, 24 hr after initial transduction. The virus titer was adjusted to give a transduction level of approximately 50%. During and following transduction, media containing IL-2 was replaced with media containing human IL-7 (10 ng/ml) and IL-15 (5 ng/ml) (Peprotech) which was found to augment T cell persistence in-vitro {ref}. Jurkat T cells were transduced by a single incubation with lentivirus overnight in the presence of Synperonic F108.

Functional confirmation of SSTR expression and measurement of SSTR2 site density

SSTR2-transduced Jurkat T cells were incubated with or without octreotide, 1 μM (Sigma) for 30 mins at 37 °C. Subsequent internalization of SSTR2 was measured by flow

cytometry analysis of SSTR2 expression. The site density of SSTR2 expression on Jurkats was determined by incubating non-transduced and SSTR2-transduced Jurkat T cells with DOTATOC (250 nM-8 nM) at either 37°C or 4°C for 30 min in PBS/0.1% BSA. After incubation, cells were washed three times and DOTATOC uptake was measured by gamma counter (Packard, Coba II Auto - Gamma). Values obtained were used for Scatchard analysis to estimate affinity and site density.

Subcutaneous Jurkat T cell xenograft

All animal experiments were performed in strict accordance with the recommendations in the Guide for the Care and Use of Laboratory Animals of the National Institutes of Health. The protocol of this study was approved by the Institutional Laboratory Animal Use and Care Committee of Weill Cornell Medicine (Permit Number: 2012-0063). SSTR2 expressing Jurkats were spiked with increasing numbers of non-transduced Jurkats to derive distinct cultures containing defined percentages of SSTR2 expression ranging from 100-0%. For each subcutaneous xenograft, 5 x 10^6 total cells were resuspeneded in 100 µl Matrigel Basement Membrane Matrix (Corning) and injected bilaterally into NOD-SCID IL2Rγ^{null} (NSG) mice (Jackson Laboratory). Measurements of tumor size were made using an external digital caliper. Tumor volume was calculated by use of the modified ellipsoid formula 1/2(Length × Width^2). Length was measured as longer dimension. Each dimensional measurement was rounded to nearest 0.5 cm.

PET/CT imaging

^{68}Ga-DOTATOC synthesis--Registered CT images was using a micro-PET/CT scanner (Inveon, Siemens). Projection data was acquired in a cone-beam geometry approximately 1 s steps at 1 degree angular increments. At least 10 million coincidence events were acquired for PET per study using a 250 to 750 keV energy window and a 6 ns timing window. Reference was included using a tube containing 100 µl of 10 %ID/cm^3 for quantification of DOTATOC uptake in vivo. The conversion of %ID/cm^3, computed relative to the counts in a reference tube, to a standard uptake value (SUV) can be made by dividing %ID/cm^3 by a value '4', assuming injection efficiency of 100% and 25 g of body weight. Visualization and analyses of PET/CT images were performed using Amide.

E:T assay

2 x 10^5 HeLa-FLuc$^+$GFP$^+$, 8505c-FLuc$^+$GFP$^+$ or HEK 293-FLuc$^+$GFP$^+$ cells were co-cultured with either non-transduced or CAR expressing T cells (SSTR2-R6.5 or R6.5) at varying E:T ratios as indicated. Co-cultures were carried out in 'T cell media' containing 150 µg/ml D-Luciferin (Gold Biotechnology) with no cytokine supplementation. Luminesence was measured with a plate reader (TECAN infinite M1000 PRO) with readings in each E:T condition normalized to the non-transduced T cell:target co-culture controls.

8505c mouse model, measurement of ex vivo organs and whole-body tumor growth

5 - 7.5 x 10^5 8505C cells were injected into NSG mice via tail vein. 2 – 3 x 10^6 T cells were injected via tail vein 4 -14 days after tumor cell injection. Luminescence imaging of tumor xenografts in live mice was performed using a whole body optical imager (In-Vivo Extreme,

Bruker). Mice were anesthetized first with 3% isoflurane in 2 L/min O_2 and subsequent to this, maintained at 2% isoflurane in 2 L/min O_2. Growth or reduction in tumor burden was estimated by integration of luminescence over the entire mouse body. Ex-vivo fluorescence imaging of mouse liver, lungs, spleen and resected tumors were performed using a whole body optical imager (In-Vivo Extreme, Bruker).

Flow cytometry

Tumor xenografts were resected from mice following completion of PET/CT imaging. Resected tumors were diced and flushed through an 80 μm cell strainer to yield single cell suspensions. Red blood cells were lysed by incubating with 1x RBC lysis buffer (eBioscience), followed by washing and re-suspension in 1x HBSS containing 2% normal goat serum. Prior to staining, cells were blocked with mouse IgG at 2 μg/ml for 10 min. This was followed by live staining with 1 μg/ml Propidium Iodide (Invitrogen) in combination with 2 μg/ml murine anti-human CD3-Alexa Fluor 647 (Biolegend) or 2 μg/ml PE-conjugated murine anti-human SSTR2 (Clone # 402038, R&D). Flow cytometry gates were determined first based on live cell gating (Propidium Iodide negative) and subsequently by parallel staining of SSTR2-transduced and wild-type Jurkat cells from culture. ICAM-1 expression on tumor cell lines was determined using a murine anti-human R6.5 monoclonal antibody (10 μg/ml) derived from hybridoma (ATCC). R6.5-CAR expression on T cells was detected using FITC-conjugated goat anti-mouse F(ab')2 secondary antibody (Thermo).

Statistical analysis

One-way ANOVA and unpaired Student's t-test were performed using Prism (GraphPad) on data indicated.

Results

Expression of SSTR2 in Jurkat T cells

We constructed a second-generation lentivirus vector for expression of human SSTR2 by inserting the SSTR2 gene downstream of the elongation factor-1α promoter. With increasing lentivirus titer, 100% of Jurkat T cells were transduced to express SSTR2 as measured by antibody binding (Fig. B1A). Consistent with agonist-induced internalization of SSTR2[20], incubation of T cells with the synthetic SSTR2 agonist (octreotide) reduced surface expression of SSTR2 as indicated by reduced antibody binding (Fig. B1B). Labeling of SSTR2-transduced Jurkat T cells with ^{68}Ga-DOTATOC (hereafter referred to as DOTATOC) at 250 nM – 8 nM followed a first-order Langmuir isotherm equation, giving a dissociation constant (K_D) of 38 nM (Fig. B1C). In comparison, DOTATOC uptake by non-transduced T cells was approximately 10-fold lower. Similar to the K_D estimated by Langmuir isotherm, Scatchard analysis estimated the K_D of DOTATOC to be 32 nM and the site density of SSTR2 to be approximately 3.2 x 10^6 molecules per cell (Fig. B1D). Actual site density is likely to be lower due to recycling of SSTR2 after internalization of DOTATOC and some level of non-specific binding. Incubation of cells at 4°C to inhibit SSTR2 recycling resulted in an estimated site density of 1.8 x 10^6 molecules per cell; however, the affinity of DOTATOC for SSTR2 was also determined to be substantially lower (K_D = 170 nM) at this temperature (Fig. B1D).

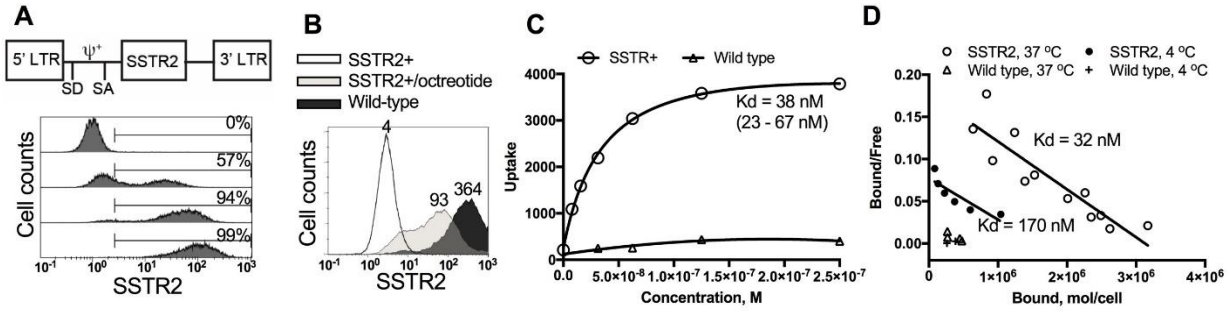

Figure B1: Expression of SSTR2 by lentivirus vector in T cells.
(A) A schematic of a lentivirus vector encoding human SSTR2 is shown. Histograms show the level of SSTR2-specific antibody binding to wild-type Jurkat T cells and Jurkat T cells transduced with increasing virus titers (1, 5, 15 µl). Percentages of SSTR2 positive cells are indicated. (B) Level of SSTR2-specific antibody binding to SSTR2-transduced Jurkat T cells with and without pre-incubation with 1 µM octreotide (37°C, 30 min). (C) DOTATOC uptake by SSTR2-transduced and wild-type Jurkat T cells versus DOTATOC concentration is shown. A first-order Langmuir isotherm equation was used to fit the data to find an equilibrium dissociation constant (Kd). Confidence interval of Kd is shown in parenthesis. (D) DOTATOC uptake of SSTR2-transduced and wild-type Jurkat T cells is shown in Scatchard plot. Estimates of Kd are shown.

Growth of mosaic Jurkat T cell xenografts

To examine the utility of SSTR2 for detection of sparsely distributed T cells in tumors, we produced subcutaneous Jurkat T cell xenografts in NSG mice with a mixture of SSTR2 transduced (referred to as $SSTR2^+$) and non-transduced (wild-type) in order to titrate levels of SSTR2 expressing cells ranging from 0 % to approximately 100 %. Xenografted Jurkat T cell tumors began to show palpable growth 30 days after xenograft, and exhibited continuous growth for the next 30 days, reaching approximately 1 cm^3 (Fig. B2A). The level of SSTR2 expression did not affect Jurkat T cell tumor growth (Fig. B2B). $SSTR2^+$ T cells in culture were 90 - 95% SSTR2 positive by antibody staining (Fig. B2C). However, later resection of 100 % SSTR2+ tumor followed by staining for SSTR2 by flow cytometry revealed that the level of SSTR2 expression was reduced to 70 - 80 %, with the15 - 20 % reduction accounted for by the presence of mouse stroma cells within tumors (Fig. B2C). The reduction of SSTR2 expression was not caused by the loss of SSTR2 expression during tumor growth as a similar level of reduction was seen by CD3 staining: 70% positive in cells harvested from tumors, reduced from 80 - 85 % CD3 positive in culture.

PET imaging of DOTATOC uptake in Jurkat T cell xenografts

We wanted to ascertain our ability to detect SSTR2 expressing T cells within tumors when both their number density (assuming a volume of single cell to be ~1 pl within tissue) and absolute numbers ranged from low to high in both respects. Thus to cover this range, we

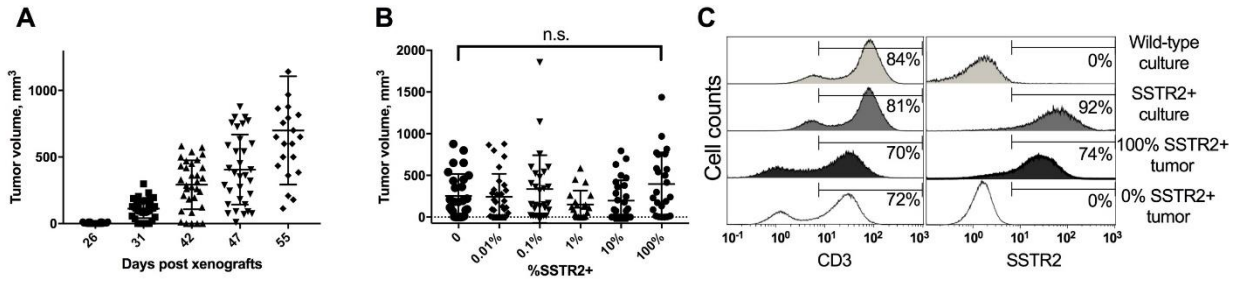

Figure B2. Growth of mosaic Jurkat SSTR2+ and SSTR2- subcutaneous tumors.
(A-B) Tumor size measurement is shown along the days of post xenografts and percentages of SSTR2+ cells. No significance (n.s.) by one-way ANOVA was found among SSTR2+ groups. (C) CD3- and SSTR2-specific antibody binding to Jurkat SSTR2+ and wild-type T cells in culture and to T cells harvested from tumors is shown in histograms. Percentages of CD3 and SSTR2 positive cells are indicated.

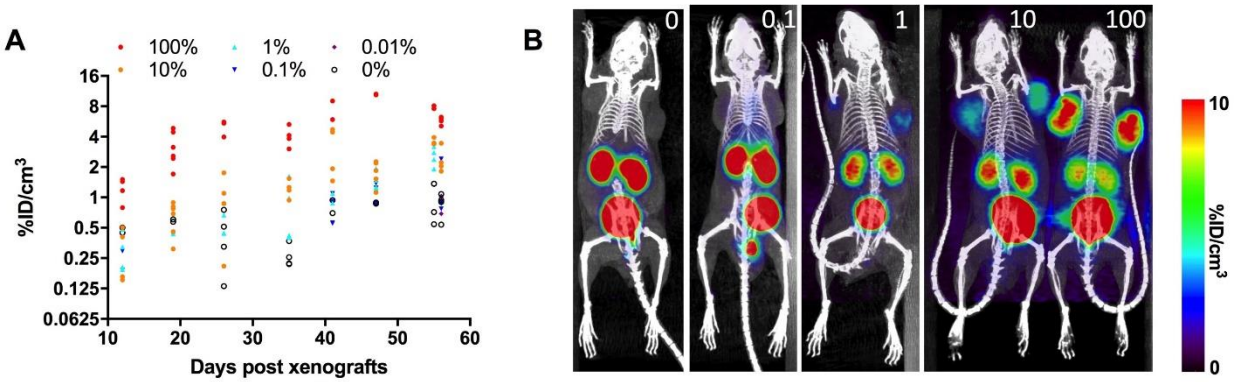

Figure B3: Quantitative PET/CT for measuring DOTATOC uptake by Jurkat tumors.
(A) DOTATOC uptake is shown in %ID/cm^3 for Jurkat tumors (100%-0% SSTR2+) in the course of tumor growth. (B) Representative PET/CT images of mice xenografted with Jurkat SSTR2+ T cells at 0% and 100%. Images are maximum intensity projection (MIP) of entire mouse body (10-20 mm thick plane). PET intensity is pseudo-colored in the range of 0-10% ID/cm^3.

initiated PET/CT imaging at 12 days post xenograft, before we could detect palpable tumor growth and continued imaging until tumors reached approximately 1 cm^3 in volume (Fig. B3A). The level of DOTATOC uptake by tumors was quantified as percent injection dose per volume (%ID/cm^3) based on the region of interest (ROI) enclosing tumors. The ROIs were defined by tumor-size measurements and anatomical information from CT images. Overall, over the course of tumor growth, DOTATOC uptake was higher in tumors with increasing percentages of SSTR2 expressing cells (Fig. B3A). PET/CT images showed DOTATOC uptake by tumors and uniformly higher uptake by the kidneys and bladder - consistent with its known biodistribution and renal clearance (Fig. B3B). DOTATOC uptake values, as measured by %ID/cm^3, agreed with visual assessment of PET/CT images over the course of tumor growth and correlated with increasing SSTR2 expressing Jurkat T cells within the tumor burden (Fig. B3). We also noted a minor increase in DOTATOC uptake during growth of 0 % $SSTR2^+$ tumors, which we speculate to be caused by the increasing leaky vasculature and stagnant blood pooling within tumors (Fig. B3A).

Defining detection limit, specificity, and sensitivity

We next analyzed DOTATOC uptake values to determine the detection sensitivity and specificity of SSTR2 expressing T cell density within tumors. At tumor sizes below 100 mm^3, DOTATOC uptake was significant only in tumors with $SSTR2^+$ T cell densities of 10 % or 100 % (Fig. B4A, B). However, a detection limit at 10% SSTR2+ tumors <~100 mm^3 (approximating detection of T cell density ~10%) was deemed unreliable as the area under the receiver operating characteristic (ROC) curve (AUC) was 0.75, which is below a clinically acceptable cutoff (>0.85) (Fig. B4C). In contrast, DOTATOC uptake for $SSTR2^+$ tumors larger than 100 mm^3

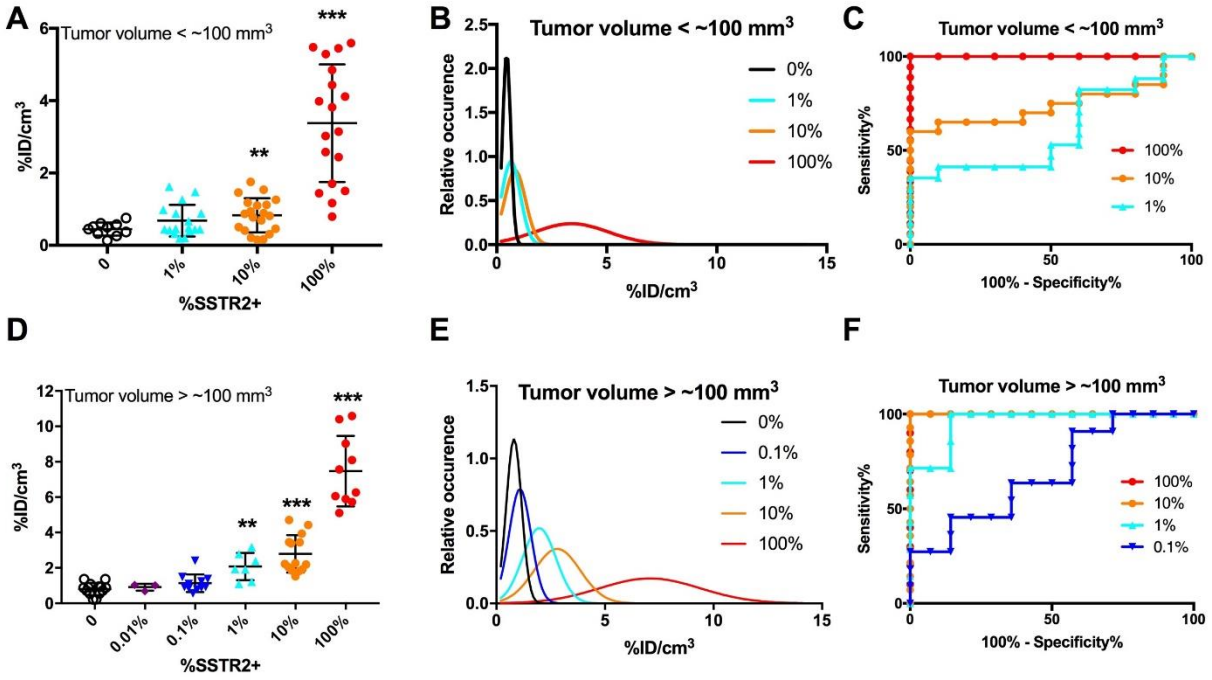

Figure B4: Statistical analysis of DOTATOC uptake by tumors.
DOTATOC uptake (%ID/cm^3) for Jurkat tumors (A&D), simulated Gaussian distribution as a function of the measured mean and standard deviation of uptake for each %SSTR2+ (B&E), and ROC curves of sensitivity and 100%-specificity% (C&F) are shown for tumors smaller than 100 mm^3 (A-C) and larger than 100 mm^3 (D-F). *** vs. 0%, $p<0.001$, ** vs. 0%, $p<0.01$ by Student's t-test.

was significantly higher at 100, 10, and 1% SSTR2$^+$ (7.1 ± 2.3, 2.8 ± 1.1, and 2 ± 0.77 %ID/cm^3, respectively) when compared to 0% SSTR2$^+$ uptake (0.8 ± 0.35 %ID/cm^3), and was detectable, although not significant even at 0.1% SSTR2$^+$ (1.1 ± 0.51 %ID/cm^3, p = 0.12) (Fig. B4D, E) A threshold of DOTATOC uptake at 1.45 %ID/cm^3 gives 95% specificity (5% false positives) and 71% sensitivity (29% false negatives) for 1% SSTR2$^+$ (approximately 0.7 - 0.8 % density of SSTR2 expressing T cells accounting for the presence of stroma cells) within our Jurkat tumor model (Fig. B4F). With the same threshold, one achieves >95% sensitivity for tumors where the SSTR2 expressing T cell density is at or above 10%.

In vitro efficacy of ICAM-1 specific CAR T cells against thyroid tumors

We then examined application of SSTR2 imaging to CAR T cells to acquire visual mapping of T cells that have been engineered to target tumors overexpressing ICAM-1. Anaplastic thyroid cancer is a particularly aggressive cancer with high mortality and has been found to overexpress ICAM-1 at levels correlating with tumor malignancy and metastatic potential[21]. The anaplastic thyroid cancer cell line 8505c was found to be 40% - 100 % positive for ICAM-1, the level of which varied due to culture conditions, exposure to cytokines, and growth *in vivo* (Fig. B5A). The cervical cancer cell line, HeLa, exhibiting naturally high levels of ICAM-1 and the ICAM-1 negative cell line, HEK 293, served as positive and negative controls respectively to test selectivity of CAR T cell mediated killing. The CAR is 3rd generation and is comprised of an ICAM-1-specific scFv (derived from mAb R6.5[22]), the transmembrane and cytoplasmic domains of CD28 followed by CD137, and CD3ζ. A lentiviral vector encoding both SSTR2 and R6.5 CAR was

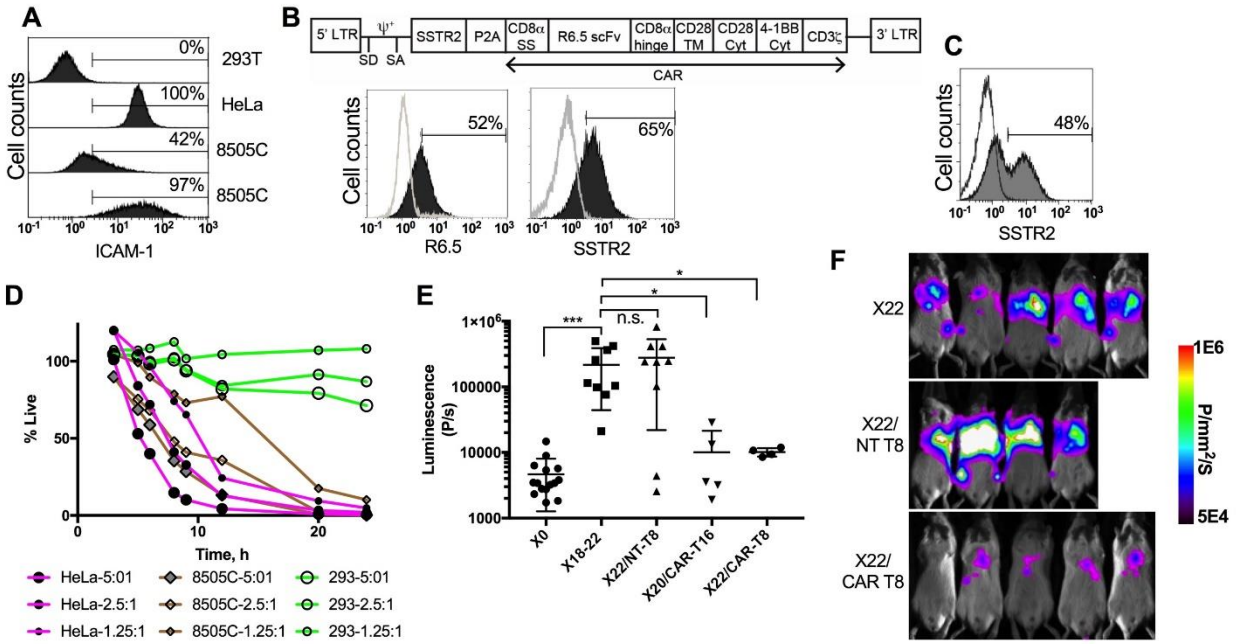

Figure B5: CAR T cell efficacy against thyroid tumor cells in vitro and in vivo.
(A) Histograms show the level of anti-ICAM-1 antibody binding to ICAM-1 negative 293T, ICAM-1 positive HeLa, and 8505C with the level of ICAM-1 expression influenced by culture conditions (passage number, confluency) and growth in vivo. (B) A schematic of a lentivirus vector of SSTR2-R6.5 CAR is shown. Anti-SSTR2 and anti-CAR antibody binding to transduced (filled) and non-transduced (open) primary T cells are shown in histograms. (C) Anti-SSTR2 antibody binding to SSTR2-transduced (filled) and non-transduced (open) primary T cells is shown in histograms. (D) Effector to target assay to measure lysis of target cells by CAR T cells. The ratios of T cells to target were 5:1, 2.5:1, and 1.25:1. Percentages of live cells were measured by the intensity of luminescence normalized to the levels of target cells incubated with non-transduced T cells as 100%. (E) Total luminescence counts (photons per second, P/s) of whole body imaging were plotted for each mouse to estimate a tumor burden of a group of mice right after injection of tumor cells (X0), a group of 18-22 days of xenograft (X18-22), a group of 22 days after xenograft and 8 days after injection of non-transduced T cells (X22/NT-T8), a group of 20 days after xenograft and 16 days after injection of CAR T cells (X20/CAR-T16), and a group of 22 days after xenograft and 8 days after injection of CAR T cells (X22/CAR-T8). (F) Whole body luminescence imaging of a group of 4-5 mice after 22 days of xenograft with or without injection of NT-T cells or CAR-T cells. *** $p<0.001$, * $p<0.05$ by Student's t-test.

constructed by linking SSTR2 to CAR with a 'ribosome skipping' porcine teschovirus-1 2A (P2A)[23] sequence (Fig. B5B). Primary T cells were transduced to express SSTR2 and R6.5-CAR at approximately 50% (65% and 52% for SSTR2 and R6.5-CAR, respectively as shown in Fig. B5B). SSTR2 and R6.5-CAR expression levels by the SSTR2-R6.5 CAR vector were comparable to what could be attained by two separate SSTR2 and R6.5-CAR vectors at similar virus titers (Fig. B5C). Incubation of CAR T cells (either SSTR2- R6.5 CAR or R6.5-CAR T cells) with targets of varying ICAM-1 expression showed that CAR T cell killing of target was dependent upon ICAM-1 expression. After 24 hours, 100% of both 8505c and HeLa cells were lysed at effector to target (E:T) ratios of 5:1 and 2.5:1, and ~90% lysis of target cells obtained at an E:T of 1.25:1 (Fig. B5D). Although there was minor yet gradual killing of ICAM-1-negative 293 cells with higher E:T ratios, specificity of CAR T cells against ICAM-1 was apparent.

In vivo efficacy of ICAM-1 specific CAR T cells against thyroid tumors

In order to test our ability to image CAR T cells and their anti-tumor efficacy in-vivo, NSG mice were xenografted by systemic i.v. injection of 0.75 x 10^6 8505c-FLuc$^+$GFP$^+$ cells followed by treatment with SSTR2-R6.5 CAR T cells. Tumor growth or lysis was evaluated by whole body luminescence imaging of firefly luciferase activity. Tumors that received either no T cells by day 18 - 22 (denoted as X18 - 22) or non-transduced parental T cells (X22/NT-T8) expanded by approximately 50-fold (Fig. B5E). In contrast, mice treated with CAR T cells either day 4 or 14 post-tumor xenograft (X20/CAR-T16 or X22/CAR-T8) showed a dramatic 25-fold reduction in tumor burden compared to non-treated mice ($p<0.05$ vs. X18 - 22) or mice that received non-transduced T cells ($p<0.05$ vs X22/NT-T8). Bioluminescence imaging of the tumors revealed

localization mainly in the lungs and liver with distant metastatic foci evident throughout the body (Fig. B5F), consistent with a prior observation of 8505c tumor growth characteristics in mice.

PET imaging of CAR T cells in vivo

Tumor bearing mice injected with T cells were randomly chosen for PET/CT to detect DOTATOC uptake and to image T cell distribution and expansion. Transverse CT images showed the heart and tumor-free alveolar air space in lungs in mice without tumors (Fig. B6). When these mice were injected with SSTR2 transduced T cells, only the background intensity of DOTATOC (0.7 %ID/cm^3) could be observed, which is indicative of the absence of T cells in the lungs (Fig. B6A). 8505C tumor xenografted mice with or without T cell infusion had alveolar air space replaced by the growth of tumor cells, which produced tissue density in CT images (Fig. B6B-G). Non-CAR, SSTR2-transduced T cells were unreactive to 8505c tumors growing in lungs as demonstrated by low DOTATOC uptake (0.9%ID/cm^3) (Fig. B6B) - likely corresponding to less than 1% T cell density. Alloreactive killing of tumors by SSTR2 transduced T cells was often observed, as illustrated by occasional instances of mice displaying reduced tumor burdens (Fig. B5E). This was associated with increased uptake of DOTATOC within lungs (2.1%ID/cm^3, corresponding to ~1% in T cell density approximated from Fig. B4D) (Fig. B6C). In comparison, SSTR2-R6.5 CAR T cells exhibited markedly higher uptake of DOTATOC (5.4 %ID/cm^3) localized to the area of tumor growth (Fig. B6D). *Ex vivo* organ imaging revealed the lungs and the liver

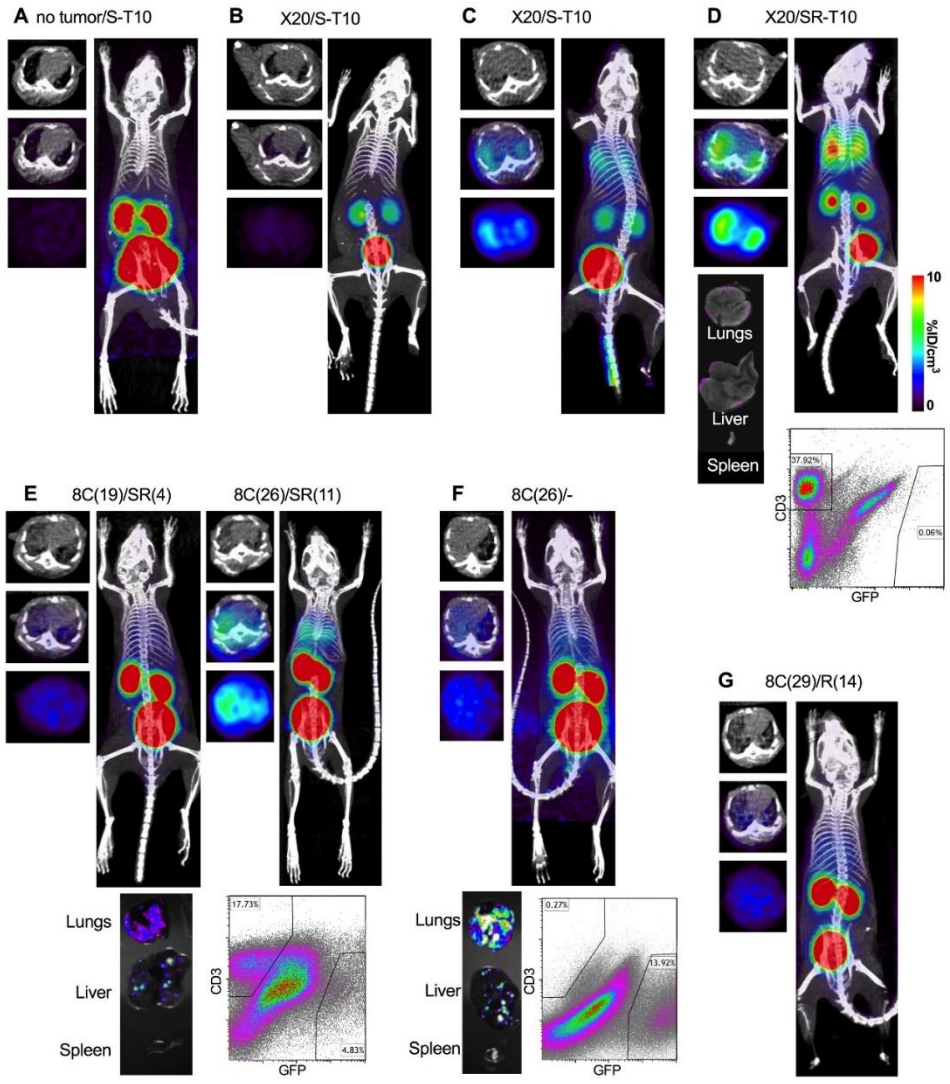

Figure B6: Quantitative PET for detection of CAR T cell distribution and expansion. PET/CT images (transverse view of 1 mm thick plane MIP and coronal view of 15 mm thick plane MIP) of a mouse with no tumor and 10 days after injection of SSTR2-transduced T cells (A), mice of 20 days after xenograft and 10 days after injection of SSTR2-transduced T cells (B-C), and a mouse of 20 days after xenograft and 10 days after injection of SSTR2-R6.5 CAR T cells (D). (E) A longitudinal PET/CT images of a mouse, 19 days after xenograft and 4 days after infusion of SSTR2-R6.5 CAR T cells (left panel) and 26 days after xenograft and 11 days after infusion of SSTR2-R6.5 CAR T cells (right panel). PET/CT images of a mouse of 26 days after xenograft and no T cells (F) and a mouse of 29 days after xenograft and 14 days after infusion of R6.5-CAR T cells (G). Ex vivo fluorescence images of lungs, liver, and spleen are shown (D-G). Flow cytometry measurement of percentages of CAR T cells (identified by anti-CD3 antibody staining) and 8505C tumor cells (GFP) harvested from lungs are shown as dot plots (D-G). Transverse views are shown for CT only, CT/PET superimposed, and PET only.

were tumor free (absence of GFP intensity). Total cells were also harvested from lung tissues and were analyzed for the presence of tumor (GFP) and T cells by flow cytometry. CD3+ T cells accounted for ~38% of live cells in the lungs whereas tumor cells were almost undetectable (~0.1%).

To demonstrate the ability to monitor T cell expansion more directly, we imaged same mice on different days after SSTR2-R6.5 CAR T cell injection. A significant increase in DOTATOC uptake in lungs was found (1.3 %ID/cm^3 to 3.4 %ID/cm^3 during the span of seven days, Fig. B6E). Compared to higher burden of tumor growth in the lungs and liver of mice without CAR T cell treatment (shown as ex vivo imaging of organs and GFP in Fig. B6F), much reduced tumor growth was found in lungs and liver (Fig. B6E). By flow cytometry, percentages of T cells and 8505c tumor cells were estimated to be ~18% and ~5%, respectively. Overall, we observed quantitative agreement between in vivo DOTATOC uptake in the lungs and flow cytometry-based estimates of T cell percentage (3.4 %ID/cm3 vs. 18% T cell density and 5.4 %ID/cm^3 vs. 38% T cell density). Elevated DOTATOC levels in both lungs and heart was frequently observed in mice with high burden of tumors and particularly in mice exhibiting difficulties with breathing, likely due to slower clearance of DOTATOC from circulation (~1.5 %ID/cm^3 in Fig. B6F, G). Uptake of DOTATOC was specific to SSTR2 expression, demonstrated by a lack of lung-specific uptake in mice treated with R6.5-CAR T cells despite CAR T cell density reaching 20 - 40% of total live cells in lungs (Fig. B6G).

Discussion

The ability to detect adoptively transferred T cells in the human body is a potentially powerful tool for monitoring T cell activity against target tumor sites as well as potential toxicity from off-site reactivity. It may also aid our understanding of the underlying causes behind the patchy success of T cell therapy in clinical cases. Our study utilizes mosaic tumor xenografts of Jurkat T cells transduced with the genetic reporter SSTR2 to correlate PET intensity to T cell density and to visualize T cell distribution *in vivo.* With the lentivirus developed in this study, the site density of SSTR2 in transduced Jurkat T cells was in the range of several million per cell, a density significantly higher than previously published[24]. To demonstrate the feasibility of SSTR2 reporter-based imaging to predict T cell activity against tumor, we chose ICAM-1 positive anaplastic thyroid cancer cells as a target model and engineered T cells to express both ICAM-1 specific CAR and SSTR2 by a single lentiviral vector. Although the correlation between T cell imaging and a change in tumor burden needs to be examined in a larger set of mice for statistical analysis, the current study presents a convincing validation for the use of SSTR2 to monitor T cell activity against tumors *in vivo*.

Quantitative PET imaging is increasingly used for disease diagnosis and to gauge therapy response in a more accurate and objective manner. From an ATT standpoint, the T cells to be imaged will distribute throughout tissues rather than form solid mass. Therefore, the utility of any T cell imaging technique will depend upon a limit-of-detection threshold low enough to enable monitoring of meaningful T cell activity. In the context of T cell killing of solid tumors, T cell density needs to be at least 1% within tumor lesions for substantial elimination of tumor mass[25]. To gauge detection limit, specificity, and sensitivity of T cell imaging in our system, we produced mosaic xenografts consisting of lentivirally transduced SSTR2 and wild type Jurkat

T cells. By titrating SSTR-transduced cells against wild type, we produced xenografts with SSTR2 levels varying from 0% to approximately 100%. We observed that with a known threshold of radiotracer uptake, one can detect T cell density at 1% with 95% specificity and 71% sensitivity. Extrapolating a change of radiotracer uptake at between 1% and 10% T cell density, a gradual increase in T cell density would increase sensitivity to >90% levels.

We chose SSTR2 as a generic reporter for a number of reasons. One was to take advantage of the FDA-approved radiotracer DOTATOC, which is currently in use in clinics to probe for overexpressed SSTR2 in neuroendocrine tumors. SSTR2 also displays relatively low basal expression in major organs except the kidneys as well as in tissues thus making it ideal for detection of adoptively transferred T cells targeting a multitude of solid tumors. Another surfaced expressed reporter gene, PSMA has been shown to be superior to more widely tested receptors such as HSV1-tk and NIS. Compared to our SSTR2 system, we also found that reporter-specific radio-ligand uptake in Jurkat T cells transduced with PSMA gave 5 - 10 fold higher uptake compared to that of non-transduced cells (data not shown). Therefore, with the myriad of available genetic reporters, choosing the most suitable agent for imaging adoptively transferred T cells will depend foremost on the tumor being targeted. For example, PSMA would not be a suitable imaging marker for CAR T cells designed to treat PSMA positive prostate cancer. Likewise, SSTR2 will be inappropriate if T cells are engineered to target SSTR2 positive neuroendocrine cancers. Therefore, at least two different genetic reporters are required to avoid a situation where a potential T cell genetic reporter is already overexpressed in the target tumor or in proximal tissues leading to specific yet non-T cell uptake of radiotracers. Interestingly, the simultaneous use of two distinct genetic reporters could

potentially create new opportunities for live T cell imaging. For example, CD4 and CD8 T positive cells could be transduced separately with SSTR2 and PSMA and sequential, time-delayed injection of cognate radiotracers followed by PET imaging could reveal underexplored dynamics of, and interactions between, adoptively transferred CD4/CD8 T cells in pre-clinical models.

Upon administration to patients, the bulk of adoptively transferred T cells undergo rapid elimination followed by expansion upon target recognition within the tumor. Indeed, it has been noted that greater expansion of T cells against target correlates with better disease remission rates[25]. Using luminescence as a measure of tumor burden, we have observed that an initial tumor burden of approximately 1 x 10^6 cells can increase more than 50-fold to an estimated 50 x 10^6 cells over 14 days. This is consistent with our flow cytometry estimate of the percentage of GFP expressing tumor cells, which was in the range of 10 - 20% (20 to 60 x 10^6 cells) of live cells harvested from lungs (which contain 200 - 300 million cells assuming 1 pl volume per cell and 200 - 300 µl of lung tissue volume). When tumor bearing mice were injected with 2 - 3 million CAR T cells 1 - 2 weeks post-xenograft, the T cell to tumor ratio will be lower than 0.1. Although it is not yet fully appreciated how many target cells can be killed by single T cells before experiencing activation-induced cell death, an increase in T cell number or expansion would be necessary to produce effective tumor elimination. Therefore, a change in T cell density over the course of tumor killing may span from 1% (2 – 3 x 10^6 cells; assuming 100% of injected T cells reside in lungs right after injection) to more than 10% when T cell expansion is at its peak. Our PET imaging was able to detect such a span of change, longitudinally and across different mice, by either allogeneic reaction or CAR mediated killing.

Although numerous efforts have been made to pre-label cells with radiotracer *in vitro* followed by *in vivo* imaging post-injection, such direct labeling methods do not allow for monitoring T cell expansion over the course of the immune response - a critical drawback when trying to predict T cell activity at on- and off-target sites as well as subsequent therapy outcomes. One drawback of T cell imaging by a genetic reporter marker for adoptive transfer of T cells is that primary T cells need to be modified with two different genes. The introduction of an extra reporter gene to CAR or T cell receptor-modified primary T cells is technically demanding and can substantially reduce the percentage of T cells co-expressing both genes. However, with the use of a self-cleaving '2A' sequence, we demonstrated that both genes can be successfully expressed on the same T cell without compromising the level of expression otherwise achievable using two independent vectors.

The conversion of DOTATOC uptake by SSTR2-R6.5 CAR T cells into T cell density using Jurkat T cell xenografts as reference needs to be examined more thoroughly with a larger set of *in vivo* data. Besides the number of T cells within tumors, the site density of SSTR2 on T cells, and the degree of perfusion within tumors and radiotracer diffusion will all influence DOTATOC uptake within tumors *in vivo*. Although we aim to transduce T cells at approximately 50% to avoid overexpressed CAR-mediated T cell exhaustion (unpublished observation), as anticipated we observed an increase in the percentage of CAR expressing T cells, presumably due to positive selection following recognition of target-positive tumors in vivo (data not shown). Under an in vitro setting, SSTR2 expressing T cells can be labeled with DOTATOC to saturation to have the level of SSTR2 expression to linearly affect DOTATOC uptake. Such a proportional relationship is unlikely to hold in vivo if radiotracers do not fully diffuse into and permeate

tumors to saturate every single cells expressing SSTR2. This should explain to a great extent why DOTATOC uptake was not linearly proportional to $SSTR2^+$ percentages in Jurkat xenografts. Despite the variability in SSTR2 expression and heterogeneity in tumor growth, however, our study provides evidence for the feasibility of monitoring multiple phases of T cell distribution and activity at on- and off-target sites including initial recruitment, expansion, and gradual killing of tumors.

Our study is the first example of a clinically adaptable, quantitative imaging technique capable of specifically detecting adoptively transferred CAR T cells in combination with their target-specific or alloreactive expansion at the tumor site. We have also demonstrated a simple method of estimating CAR T cell density infiltrating solid tumors by comparing radiotracer uptake by SSTR2-CAR T cells to that of titrated SSTR2 expressing Jurkat T cell tumor xenografts. We posit that SSTR2/DOTATOC-based T cell imaging should be able to detect T cells with clinically acceptable sensitivity and specificity at a T cell density of 1% and higher. We anticipate that the imaging technique developed in this study can contribute to improving T cell immunotherapy in cancer by facilitating efforts to explore adjuvant therapies, increasing our understanding of parameters that mediate successful adoptive therapy and also to aid in the investigation of the underlying causes of systemic toxicities that impede adoptive T cell-based therapies.

Acknowledgements

NIH grants R01CA178007, R21AI07451.

REFERENCES

1. Porter, D.L., et al., *Chimeric antigen receptor-modified T cells in chronic lymphoid leukemia.* N Engl J Med, 2011. **365**(8): p. 725-33.
2. Brentjens, R., et al., *Treatment of chronic lymphocytic leukemia with genetically targeted autologous T cells: case report of an unforeseen adverse event in a phase I clinical trial.* Mol Ther, 2010. **18**(4): p. 666-8.
3. Yaghoubi, S., et al., *Human pharmacokinetic and dosimetry studies of [(18)F]FHBG: a reporter probe for imaging herpes simplex virus type-1 thymidine kinase reporter gene expression.* J Nucl Med, 2001. **42**(8): p. 1225-34.
4. Penuelas, I., et al., *Positron emission tomography imaging of adenoviral-mediated transgene expression in liver cancer patients.* Gastroenterology, 2005. **128**(7): p. 1787-95.
5. Barton, K.N., et al., *Phase I study of noninvasive imaging of adenovirus-mediated gene expression in the human prostate.* Mol Ther, 2008. **16**(10): p. 1761-9.
6. Castanares, M.A., et al., *Evaluation of prostate-specific membrane antigen as an imaging reporter.* J Nucl Med, 2014. **55**(5): p. 805-11.
7. Moroz, M.A., et al., *Comparative Analysis of T Cell Imaging with Human Nuclear Reporter Genes.* J Nucl Med, 2015. **56**(7): p. 1055-60.
8. Griessinger, C.M., et al., *In vivo tracking of Th1 cells by PET reveals quantitative and temporal distribution and specific homing in lymphatic tissue.* J Nucl Med, 2014. **55**(2): p. 301-7.
9. Ahrens, E.T. and J.W. Bulte, *Tracking immune cells in vivo using magnetic resonance imaging.* Nat Rev Immunol, 2013. **13**(10): p. 755-63.
10. Yaghoubi, S.S., et al., *Noninvasive detection of therapeutic cytolytic T cells with 18F-FHBG PET in a patient with glioma.* Nat Clin Pract Oncol, 2009. **6**(1): p. 53-8.
11. Dobrenkov, K., et al., *Monitoring the efficacy of adoptively transferred prostate cancer-targeted human T lymphocytes with PET and bioluminescence imaging.* J Nucl Med, 2008. **49**(7): p. 1162-70.
12. Adonai, N., et al., *Ex vivo cell labeling with 64Cu-pyruvaldehyde-bis(N4-methylthiosemicarbazone) for imaging cell trafficking in mice with positron-emission tomography.* Proc Natl Acad Sci U S A, 2002. **99**(5): p. 3030-5.
13. Charoenphun, P., et al., *[(89)Zr]oxinate4 for long-term in vivo cell tracking by positron emission tomography.* Eur J Nucl Med Mol Imaging, 2015. **42**(2): p. 278-87.
14. McCracken, M.N., et al., *Noninvasive detection of tumor-infiltrating T cells by PET reporter imaging.* J Clin Invest, 2015. **125**(5): p. 1815-26.
15. Liu, Z. and Z. Li, *Molecular imaging in tracking tumor-specific cytotoxic T lymphocytes (CTLs).* Theranostics, 2014. **4**(10): p. 990-1001.
16. Yamada, Y., et al., *Cloning and functional characterization of a family of human and mouse somatostatin receptors expressed in brain, gastrointestinal tract, and kidney.* Proc Natl Acad Sci U S A, 1992. **89**(1): p. 251-5.

17. Garkavij, M., et al., *177Lu-[DOTA0,Tyr3] octreotate therapy in patients with disseminated neuroendocrine tumors: Analysis of dosimetry with impact on future therapeutic strategy.* Cancer, 2010. **116**(4 Suppl): p. 1084-92.
18. Rivera, M., et al., *Histopathologic characterization of radioactive iodine-refractory fluorodeoxyglucose-positron emission tomography-positive thyroid carcinoma.* Cancer, 2008. **113**(1): p. 48-56.
19. Higgins, M.J., A. Forastiere, and S. Marur, *New directions in the systemic treatment of metastatic thyroid cancer.* Oncology (Williston Park), 2009. **23**(9): p. 768-75.
20. Cescato, R., et al., *Internalization of sst2, sst3, and sst5 receptors: effects of somatostatin agonists and antagonists.* J Nucl Med, 2006. **47**(3): p. 502-11.
21. Buitrago, D., et al., *Intercellular adhesion molecule-1 (ICAM-1) is upregulated in aggressive papillary thyroid carcinoma.* Ann Surg Oncol, 2012. **19**(3): p. 973-80.
22. Cosimi, A.B., et al., *In vivo effects of monoclonal antibody to ICAM-1 (CD54) in nonhuman primates with renal allografts.* J Immunol, 1990. **144**(12): p. 4604-12.
23. Kim, J.H., et al., *High cleavage efficiency of a 2A peptide derived from porcine teschovirus-1 in human cell lines, zebrafish and mice.* PLoS One, 2011. **6**(4): p. e18556.
24. Zhang, H., et al., *Imaging expression of the human somatostatin receptor subtype-2 reporter gene with 68Ga-DOTATOC.* J Nucl Med, 2011. **52**(1): p. 123-31.
25. Boissonnas, A., et al., *In vivo imaging of cytotoxic T cell infiltration and elimination of a solid tumor.* J Exp Med, 2007. **204**(2): p. 345-56.
26. Carpenito, C., et al., *Control of large, established tumor xenografts with genetically retargeted human T cells containing CD28 and CD137 domains.* Proc Natl Acad Sci U S A, 2009. **106**(9): p. 3360-5.
27. Hofig, I., et al., *Poloxamer synperonic F108 improves cellular transduction with lentiviral vectors.* J Gene Med, 2012. **14**(8): p. 549-60.